REVIEW

Germanium Self-Assembled Quantum Dots in Silicon for Nano- and Optoelectronics

A. I. Yakimov*, A. V. Dvurechenskii, and A. I. Nikiforov

Institute of Semiconductor Physics, Siberian Branch of the Russian Academy of Sciences,
630090 Novosibirsk, Russia

The scope of this article is to review the formation mechanisms, variety of electronic and optical phenomena, as well as possible device-oriented applications, in Ge/Si self-assembled quantum dots that have been synthesized by molecular-beam heteroepitaxy. A difference of this review from the other existing works on physics of Ge/Si nanostructures is that we will focus on the fundamental aspects and device applications of the dots whose size is extremely small ($\sim$10 nm) and the electronic states resemble certainly those of an atom even at room temperature.

Keywords: Self-Assembling, Quantum Dots, Germanium, Silicon, Strain, Electronic Structure.

CONTENTS

1. INTRODUCTION

The two last decades have witnessed the emergence of a new branch of semiconductor physics that studies the behavior of electrons confined in precisely tailored man-made potential. This field has developed from the obvious progress in technology that now allows for the routine fabrication of nanometer-scale solid state structures that contain small number of conduction electrons ($<$100) in geometries of size comparable to their de Broglie wavelength. Usually they are called "quantum dots" (QDs), referring to their quantum confinement in all three spatial dimensions. The three-dimensional confinement leads to formation of a discrete carrier energy spectrum, resembling that of an atom. Next to this purely quantum effect, an important element of electronic transport through QDs is Coulomb blockade. An extra electron can only be added to the dot if enough energy is provided to overcome the Coulomb repulsion between the electrons. Studying the

QD systems has proven to be a fertile experimental and theoretical endeavour, in which the discreteness of charge carried by a single electron and the interplay of quantum effects become manifest in striking ways.[1]

A common way to fabricate a single QD is to restrict the two-dimensional electron gas in a semiconductor heterostructure laterally by electrostatic gates, or vertically by etching techniques. This creates a bowl-like potential in which the conduction electrons are trapped. In a single QD weakly coupled by tunneling barriers to two leads, the interplay of single-electron charging effects and resonant tunneling through quantized states leads to conductance

Andrew I. Yakimov received his M.S. degree in Physics from the Novosibirsk State University, Russia, in 1986. He received his Ph.D. degree in Solid State Physics and degree of Doctor of Physics and Mathematics from the Institute of Semiconductor Physics, Russia, in 1991 and 2001, respectively. In September 1986, he joined the Laboratory of Nonequilibrium Semiconductor Systems of the Institute of Semiconductor Physics, Siberian Branch of the Russian Academy of Science, where he is a Leading Researcher. In 1994, 1996, and 1998 he worked as a Visiting Scientist at Cambridge University, UK. Dr. Yakimov's research interests are in the area of electronic processes in low-dimensional systems. Current research topics in his group include Ge–Si quantum dots, single-electron phenomena, strain-induced modification of band structure, electron and hole transport in arrays of self-assembled quantum dots, spatially indirect excitons and excitonic complexes, and Ge–Si related nanodevices. He has authored more than 100 refereed journal publications including 8 review papers in the area of Ge–Si quantum dots. His research work was recognized by Administration of Novosibirsk Region Award for "Commercially Valuable Scientific Research" (2003) and the President of Russian Federation Award for Young Doctors of Science (2004).

Anatoly V. Dvurechenskii is Professor, Doctor of Physics and Mathematics in the field of semiconductors, insulators, quantum nanostructures, and nanotechnology. He has graduated from Novosibirsk State University, Physics Department in 1968. He is working in Institute of Semiconductor Physics, Siberian Branch of Russian Academy of Science (Novosibirsk) since 1968 year starting from junior researcher, then senior (1981) and leading (1986) researcher, head of the laboratory of Nonequilibrium Semiconductor's Systems (1987), and deputy director of Institute of Semiconductor Physics (2002). He received his Ph.D. degree in Physics and Mathematics from the Institute of Semiconductor Physics in 1974 and his Doctor of Physics and Mathematics degree from the same Institute in 1988. The main research interests are in the area of atomic and electronic structure of point defects induced by fast electrons, neutrons and ion beam irradiation; ion-beam assisted phase transition, crystal nucleation and growth; laser annealing, melting, solidification; electronic and optical phenomena in disordered system and low dimensional structures. Current research topics in his laboratory is quantum dot heterostructures: nanocrystal nucleation and growth with pulsed ion beam action during molecular beam epitaxy, electron transport and optical phenomena in quantum dot heterostructures, pulsed laser annealing, and nanodevices. As a guest scientist he worked in New York State University at Albany (1979), in Research Center Rossendorf, Dresden, Germany (since 1980 practically every year), Fudan University, Shanghai, China (2001, 2002, and 2006). He has over 250 journal publications, co-author of three books and three invited book chapters. He received the highest award of the Soviet Union in science, State Prize in 1988 for the results on physical phenomena at pulsed laser annealing of thin semiconductor's layers, and International prize of academies of science of Soviet Union and German Democratic Republic. He is Professor of Novosibirsk State University to lecture on: "Radiation Physics of Semiconductors" and "Physics of Semiconductor Nanotechnology." He is member of scientific boards on the problems of "Physics of Semiconductors" and "Radiation Physics of Solid State" in Russian academy of science.

Alexander I. Nikiforov received his M.S. degree in Electronic Techniques (1979) from Novosibirsk Electrotechnical Institute, Physical and Technical Department. He received his Ph.D. in Solid State Physics (1994) from Institute of Semiconductor Physics, Russian Academy of Sciences, Siberian Branch. In 1979, he joined in MBE Department, Institute of Semiconductor Physics, Russian Academy of Sciences, Siberian Branch as Engineer, Junior Research Scientist, Research Scientist, Senior Research Scientist, and Leading Research Scientist. He leads the SiGe MBE growth group. Current research topics in his group include growth process studies of Ge quantum dots on Si and SiO_2 surfaces, delta-doped silicon layers, and low-temperature growth.

oscillations as the electrochemical potential of the dot is tuned. This phenomenon underlies the working of nanoscale single-electron transistors which have a number of practical uses, ranging from metrology to computing. Recently, research focused on double-dot systems[2] whose behavior is found to be mainly affected by electrostatic coupling between the two dots inside the artificial molecular. The next step is to create and study macroscopic arrays of close packed QDs, which are required for the development of semiconductor lasers,[3] photodetectors,[4] single-photon devices,[5] as well as quantum computation.[6]

An elegant way to fabricate large-scale arrays of zero-dimensional semiconductor structures is based on strain-induced self-assembly of islands during heteroepitaxial growth of lattice mismatched materials. Ge on Si(001) (4.2% lattice mismatch) is one of the best studied systems exhibiting a self-organization of nanostructures in semiconductor heteroepitaxy. Electronic and opto-electronic nanodevices implemented on Ge self-assembled quantum dots (SAQDs) in Si matrix have attracted much attention due to their compatibility with modern Si-based complementary metal-oxide-semiconductor circuitry. This would offer a substantial reduction in complexity and cost of future high performance electronics. Considerable work has been done on the growth of Ge dots and important results have been discussed in recent reviews.[7–12] In this paper we will discuss the physics and several device aspects of Ge/Si nanostructures with SAQDs whose size is extremely small ($\sim$10 nm) with the motivation of relevance of such systems for realizing quantum devices operating at room temperature.

2. STRAIN-DRIVEN QUANTUM DOT SELF-ASSEMBLY

Elastic deformations in epitaxial films is the key factor that not only causes the morphological planar-to-island film transition (Stranski-Krastanov mechanism) but also effects the further stages of island evolution, including the shape, size, composition, and spatial distribution of the islands. In this section, the discussion deals with experimental data on the process of formation of self-organized Ge islands on pure and oxidized Si(100) surface.

The germanium on silicon heterosystem has been used for a long time to study the two-dimensional to three-dimensional transition. Phenomena of nanoisland self-organization are of interest to several areas of solid-state physics. For physics of surface and condensed media, the actual importance are studies of the mechanisms of nanostructure growth and atomic processes occurring on the surface during the growth. However, these objects also are of interest to semiconductor physics because of their potential application as quantum-sized nanostructures. When synthesized at relatively low temperatures, these islands are free of misfit dislocations even though they reach the size larger than the critical thickness.

Dislocation-free germanium islands of 10 to 100 nm in size are detected on the Si(100) surface after formation of a continuous Ge film.[13]

The islands can be downsized when germanium is deposited at a lower temperature. The smallest germanium islands growing on the pure silicon surface are about 10 nm in lateral size and much smaller in growth direction. The size can be also reduced when Ge later is deposited on the oxidized atomically pure surface prepared *in situ* in the MBE installation. It has been known for long time that the oxide layer can be generated on the silicon surface under vacuum conditions. Possibility of choosing regimes of etching and growth of the oxide film depending on oxygen pressure and temperature has been demonstrated for the first time elsewhere.[14] Growth of germanium islands on the pre-oxidized silicon surface allows the islands to be decreased considerably in size at a higher density. The islands grown on the oxidized Si(111) surface are shown to be 10 nm in lateral size at the density higher than 10^{12} cm^{-2} (Refs. [15, 16]). The authors of Ref. [15] supposed that this is the case of local disoxidation of silicon by germanium accompanied by desorption of germanium monoxide. Germanium nanoislands conjugated coherently with silicon are nucleated in these sites.

2.1. Basic Concepts

Three stages of nucleation and evolution of three-dimensional (3D) islands can be classified. Basic regularities of the island nucleation in an epitaxial heterosystem are determined by the balance between the film and substrate surface energies, as well as between the film-substrate interface energy and the intrinsic energy of the island bulk. The free energy of a newly formed nucleus on the substrate surface can be a sum of three terms:[17]

$$\Delta G = -V\Delta\mu + \gamma s + E_i\left(V, \frac{h}{l}\right) \qquad (1)$$

Here the first term is the work function of formation of a new nucleus of volume V with $\Delta\mu$ as the thermodynamic driving force of crystallization (supersaturation); the second term is the work function for producing an extra surface s with γ as the nucleus surface energy. The third term is the additional energy due to elastic deformation of the nucleus. The first two terms represent the classical version of the nucleation theory (see, e.g., Ref. [18]), while the last term cannot be assigned to any process but to the growth of strained films. At a high lattice mismatch, for example, at one inherent in the Ge–Si system, the additional energy is a function of not only the nucleus volume but also the shape, h/l (the height to cross-size ratio of the nucleus), it being essential for the two-dimensional (2D) to 3D transition. From computing by Müller and Kern, the contribution of this term looks like a rapidly drop-down function of h/l. The more apparent three-dimensionality of the strained nucleus, the lower is the contribution of the

strain energy to the free energy of the nucleus. The surface energy of the system of Ge film (Ge island)–Si substrate is also dependent on the Ge layer thickness (and on the shape of the Ge island).[17, 19]

As the first approximation, the strain energy lowering at the island tops due to the elastic relaxation is the key factor of the transition from two-dimensional to three-dimensional growth modes of pseudomorphous films, with the mismatch strains being of crucial importance. For the case of homoepitaxy at a sufficiently pure surface of almost all semiconductors, 3D islands are not formed but the films grow either through step propagation (step-layer growth mode) or through nucleation and coalescence of 2D islands. It will be demonstrated below that the strains contribute considerably to the evolution and size distribution of 3D islands.

In Refs. [20, 21], the crucial role of the elastic strain relaxation in the morphological instability of the film surface has been shown. The underlying idea of this model is that the roughened surface of the strained layer possesses a lower total energy due to the elastic strain relaxation at the tops of ridges. An increase in the surface energy is the factor that counteracts the evolution of the film relief but causes only a partial decrease in the energetic gain due to the relaxation. The higher the film-to-substrate lattice mismatch, the lower the thickness at which the pseudomorphous film becomes morphologically unstable. The formation of islands is the extreme case of the morphological instability of strained films. It is normally observed in the systems with a high film-to-substrate lattice mismatch (4% for the Ge–Si system). If the surface energy of the newly formed phase is diminished in any way, the morphological instability of the strained film may be achieved at a low-lattice mismatch.

In line with the classical considerations,[22] the process of formation of a new phase involves basic stage of nucleation, independent growth of the nuclei and, finally, evolution of the nuclei in cooperation with one another, the so-called Ostwald ripening (OR). The latter is the latest stage of the growth of nuclei of the new phase in time. If the study is aimed at synthesis of an island film (that is just the case under consideration), then OR is the key stage controlling the nature of the island size distribution. For this reason, great attention is paid to the problem of applicability of the OR model to analysis of the processes of quantum-sized cluster self-assembling in Ge–Si.

Experimental observations of the evolution of 2D silicon islands on Si(001) surface are in good agreement with the OR model (see, e.g., Ref. [23]). At the starting point, the substrate surface is covered by a supersaturated adsorbate. The first stage is the nucleation of 2D islands. The next stage is the island growth when the supersaturation is lowered around the islands but the latter do not as yet interact. Therefore, nucleation continues at the

sites away from already formed islands. After the areas of diffusive "nutrition" of the islands have been overlapped and the supersaturation level falls down in gaps between the islands, the probability of new nucleation decreases, and the third stage begins. This is the stage of correlated growth of islands, or Ostwald ripening. Large islands grow and small islands disappear. This stage can take a long time if the system is closed and the amount of adatoms is less then one monolayer. The size distribution of islands is a reproducible function that depends essentially on the substrate orientation.

Lifshitz and Slyozov[24] stated, in particular, that elastic deformations in grains as the second-order factor may be taken into consideration but do not influence essentially the nature of the final distribution. Indeed, for the three-dimensional case under consideration by Lifshitz and Slyozov, strains in 3D grains of the new material may be treated as an extra portion of free energy of the cluster, which effects the rate of the cluster nucleation and growth. The latest studies have demonstrated that elastic deformations in epitaxial films and in emerging 3D islands are the key and multivalued factor. There are many cases when this factor makes dramatic changes to the classical set of phase-formation mechanisms. For example, for the case of Ge-on-Si, the occurrence of these deformations leads to transition from the layer-by-layer growth to nucleation of 3D clusters at the surface of the underlying Ge layer (i.e., to the achievement of the Stranski-Krastanov mechanism). Remarkable inhomogeneity of the elastic relaxation of the islands along their heights causes shape-dependent elastic relaxation (i.e., energetic profit). As a result, several discrete cluster shapes "hut," "dome," "super-dome") arise, which are the most energetically favorable. Elastic deformations at the cluster base and in the adjacent substrate region increase as the cluster increases in size.[25] The elastic deformations and their relaxation in islands can, under certain conditions, predominate until a quasiequilibrium state is established. In this case, the shape and size distribution of the ensemble of islands are time-independent.

2.2. Growth of Ge Self-Assembled Quantum Dots on Si(100) Surface

Several stages of island evolution were experimentally observed in Ge–Si heterosystems during the increase of the film effective thickness. These stages are different for the (001) and (111) substrate surfaces. In terms of generation of quantum-size objects, the (001) surface is unique: this is the only surface where compact dislocation-free 3D islands of 10–100 nm were discovered. These islands appear upon formation of a continuous Ge film (wetting layer). The start of 3D cluster nucleation is accompanied by appearance of strikes in the reflection high energy electron diffraction (RHEED) patterns, which are assigned to electron scattering at {105} planes. These islands were

called hut clusters[26] because of their shape. As the average film thickness increases, RHEED patterns start showing {113} and {102} planes along with {105}. The formation of dome clusters is characteristic of this stage. On passing from hut clusters (10–20 nm in lateral size) to dome clusters (50–100 nm), the relaxation level of mechanical strains increases. After Floro et al.,[27] the material is elastically relaxed by 20% in hut clusters but by more than 50% in dome islands because of their higher aspect ratio. In the latter case, the islands keep on coherency with the substrate. From numerous experimental observations, the last stage of morphological and structural evolution of Ge islands on Si(001) and Si(111) is the formation and rapid growth of plastically deformed 3D islands with misfit dislocations at the island-substrate interface (see, e.g., Ref. [28]).

2.3. Self-Assembling

It was mentioned above that the surface morphology is of considerable importance in ordering of 3D islands formed on this surface. This factor can be used to control ordering of both shape and spatial distribution of islands. Surface parameters can be controlled by the following ways:
— The use of substrates misoriented from the (001) surface and the respective methods for step ordering. The steps are used as patterns for island nucleation.
— The use of surfactants to modify surface characteristics (surface energy, adatom diffusion length) of both substrate and epitaxial layer.
— Generation of microstrains on the substrate surface to initiate island nucleation in the desirable sites (layer stacking).
— Lithographic patterning: creation of windows on the substrate to confine the range of assembling of adatoms into an island and to isolate the islands. Photolithographic formation of facet planes for localization of nucleation of Ge islands.

Considerable attention was given to the size distribution of Ge islands since this parameter of QD systems is of extreme practical importance. The more narrow distributions for dome clusters are accounted for by the fact that the accumulation of elastic deformations in the substrate and in the cluster bottom at an increase in the cluster size results in a deceleration of the cluster growth rate (in contrast to the island evolution according to the OR mechanism). The growth rate of Ge hut clusters decreased with an increase in the cluster size. This effect is studied in more detail in Ref. [25]. The result is the remarkable narrowing of the island-size distribution. The most uniform size distribution of Ge islands (∼3%) was reported in Ref. [29]. The authors assert that such a narrow distribution was obtained due to a very careful choice of island growth conditions.

Almost simultaneous nucleation of islands throughout the substrate surface can be achieved if a considerable supersaturation of germanium adatoms is provided at the earliest instance of the growth process, for example, through a momentary increase of the molecular flux or a short-time reduction of the substrate temperature. So-called the synchronizing effect of periodical short-term variations in the surface supersaturation on the 2D nucleation earlier was realized at homoepitaxy of Ge and Si.[30] Later, an optimized method for synthesis of quantum structures such as vertical superlattices, quantum wires or QDs at cyclic supersaturation for growing each atomic layer constituting the film was proposed and substantiated.[31]

The weakest kind of ordering is areal ordering due to a weak interaction between the islands at the earliest stage of their growth. Therefore, pregeneration of ordered sites for nanocluster nucleation is the most attractive way to obtain their spatially ordered state. The spatial ordering increases with increasing coverage (ratio of the total island area to the substrate surface area) because of minimization of repulsive forces of elastic interaction between adjacent islands. Therefore, the highest spatial ordering is observed for island arrays that occupy most of the substrate surface.

The successive growth of layers with Ge islands to be covered by the material matching the substrate (Si) was shown to enhance island ordering in both their size and surface area.[19] Cluster-induced disturbance of elastic deformation fields penetrates for various distances into the covering layer, depending on the volume of an individual island and on island agglomeration. Sites for preferable nucleation of new islands at the next "floor" are formed at the surface of the covering layer. Control of the thickness of the covering layer makes it possible to minimize the effect of "weak" islands. Both theoretical and experimental studies in the field were accomplished; several identical examples were given for Ge–Si systems.[19, 32] These multilayer heterostructures with QDs are of practical importance for innovative research fields (e.g., electron bonding of clusters through vertical, synthesis of 3D lattices comprising islands-clusters often referred to as "artificial atoms").[33, 34]

2.4. Size and Density of Self-Assembled Quantum Dots

Experience shows that traditional methods for generation of germanium quantum dots do not allow the QD size to be considerably decreased and the density increased. Among the promising ways are
— Growth of germanium islands on SiO_2 synthesized immediately before deposition of Ge in a MBE installation.
— Low-temperature growth.
— Growth in prepatterned oxide windows.
— Formation of islands during growth of the wetting layer.

GeSi hut and dome clusters sizes are seen to increase with the concentration of Si in the GeSi solid solution.[35] As the proportion of Si increases, strains are decreased in the cluster, and the necessary energetic gain due to the elastic relaxation of islands is attained at their larger sizes. Solid GeSi solutions, because of their relatively large sizes, are very suitable for model experiments aimed at elucidating basic regularities of the island formation.[27] However, the practical interest is focused on the systems with not larger than 10-nm nanoislands (pure Ge on Si) because of the possibility in optoelectronic applications. The islands density is again of much importance. The system response to an external action is in direct relationship with the number of islands and with the island density. Both parameters (size and density) depend on such growth conditions as substrate temperature and growth rate. A decrease in the growth temperature, as well as an increase in Ge flux, results in a shortening of the diffusion length of Ge adatoms through the substrate. Correspondingly, the range of adatoms assembling for one island is contracted; the island decreases in size but the density of island increases. Abstreiter et al.[36] could vary the density of islands in the regular manner up to the density of 10^{10} cm^{-2} by decreasing the growth temperature to 550 °C and increasing the Ge flux. The further decrease of the growth temperature to 300 °C allowed the density of Ge islands to be increased to $\sim 3 \times 10^{11}$ cm^{-2} (Ref. [37]) (Fig. 1). Peng et al.[38] reached the highest density of Ge islands on Si(100) surface (5×10^{11} cm^{-2}) using antimony as a surfactant to decrease the surface diffusion length of Ge adatoms.

It is possible to reduce the QD dimension by growing germanium on the oxidized atomically pure surface prepared *in situ* in the MBE chamber. Depending on the thickness of the deposited germanium layer on silica surface, the islands are different in size and density. At the film not thicker than five monolayers (ML), the islands are less than 10 nm in base diameter and have the density higher than 2×10^{12} cm^{-2} (Ref. [39]) (Fig. 2(a)). These samples were also used for HREM studies in plan-view and cross-sectional conditions. Figure 3 shows pertinent TEM images.[40] An increase in the effective thickness of deposited germanium results in formation, along with small sized islands, of islands with the size larger by an order of magnitude at a considerably lower density. Their lateral size reaches 200 nm and the density of about 1.5×10^9 cm^{-2} (Fig. 2(b)). The large germanium islands are relaxed and their lattice constant equals to that of bulk germanium. This conclusion also is supported by the presence of Moire fringes in the electron micrographs. It should be noticed that the islands are not pronouncedly faceted but almost spherical in shape. A similar island shape was observed during *in situ* STM analysis of Ge islands on Si(111) surface.[15] It looks like the island shape depends on the presence of an oxide layer but not on the layer thickness or substrate orientation.
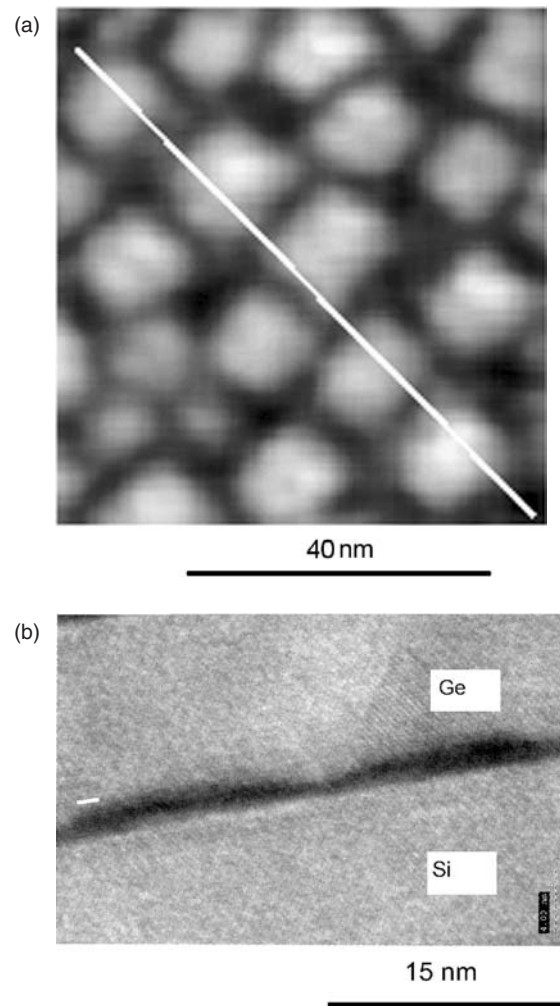
Fig. 1. Plan-view STM (a) and cross-section TEM (b) images of Ge islands on Si(001) surface (deposition temperature $T_s = 300$ °C, equivalent thicknesses of Ge layer $d_{\text{eff}} = 10$ ML).

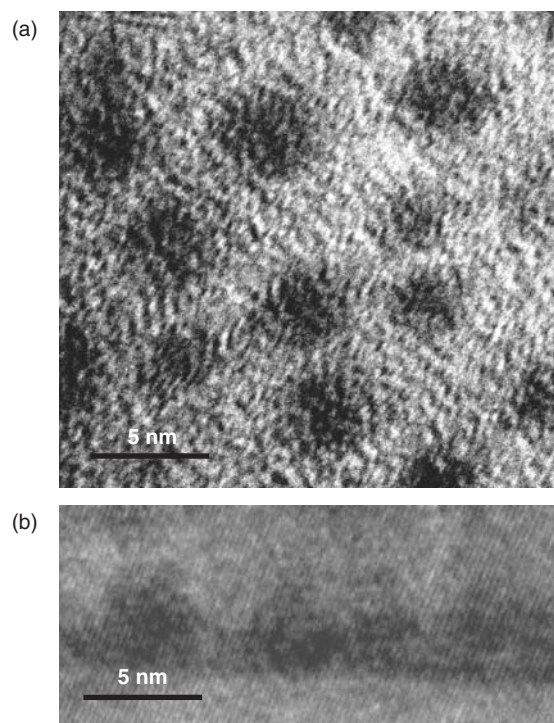## 2.5. *In Situ* Reflection High Energy Electron Diffraction Control of Quantum Dot Growth

The strong dependence of the island parameters on the technological conditions makes it necessary to provide continuous monitoring of the growing surface of the substrate. The appropriate traditional method is RHEED technique. A typical example of comprehensive surface study during heteroepitaxy is presented in Ref. [41]. Of particular interest are the data on strains in the growing layer, which are the driving force of the observed morphological rearrangement. The strains can be estimated from variations of the lattice constant of the Ge film during the transition from 2D to 3D growth modes, as well as from changes of the island shape. The lattice constant of the growing layer can be determined from variations of the distance between correspondent spots of the RHEED pattern. The intensity oscillations were registered in the diffraction pattern in the azimuth [110] along the line intersecting several reflections, including bulk spots. The experimental data
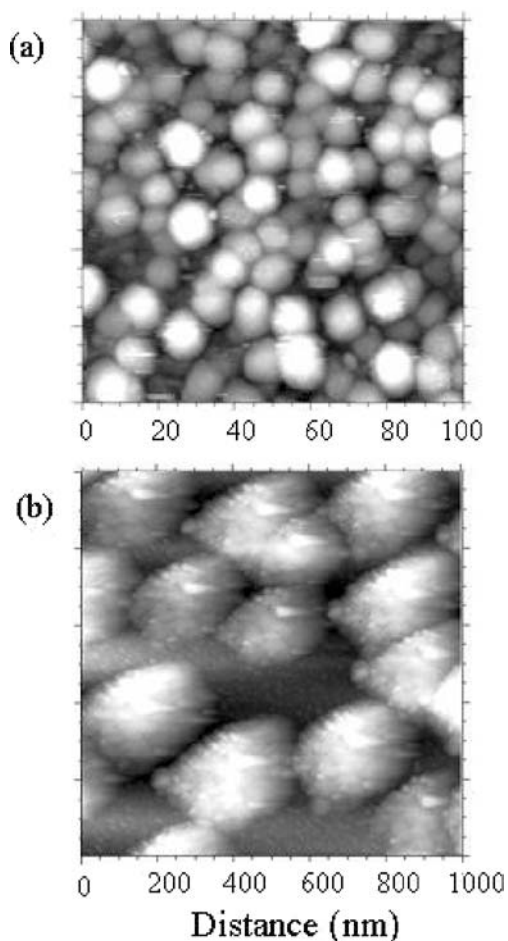
Fig. 2. STM image of Ge islands on oxidized Si(001) surface ($T_s = 500$ °C, $d_{eff} = 3$ ML (a) and 6 ML (b)).

Fig. 3. Plan-view (a) and cross-section (b) TEM images of Ge islands on oxidized Si(001) surface ($T_s = 500$ °C, 3 ML of Ge).

were used for constructing the structure phase diagram[41] to show the existence ranges of strained and elastically deformed continuous and island films depending on Ge thickness and deposition temperature (Fig. 4).

The process of Ge film growth on silicon oxide surface was controlled using a RHEED patterns also. The initial stage of germanium film growth on the oxidized Si surface was analyzed by registering variations in the intensities of specular reflection and three-dimensional diffraction reflection (3D-reflection).[42] These values were very sensitive to variations in the surface roughness, while appearance of 3D-reflection indicated the presence of 3D objects on the surface under study. The occurrence of intensity oscillations of the specular reflection during growth on the pure surface, extinction of the reflection and appearance of 3D-reflection at the germanium film thickness more than 4 monolayers argue for 2D growth of the wetting layer followed by formation of three-dimensional islands. As to the Ge film growth on the oxidized surface, the reflection intensities are only varied after deposition of one monolayer, and the specular reflection intensity does not oscillate (Fig. 5). These observations indicate the absence of the stage of wetting layer formation. While the first monolayer

is deposited on the SiO$_2$ surface, an adsorbed Ge layer is formed that is transformed into 3D islands during the growth of the second and next monolayers. Therefore, germanium film growth on the oxidized silicon surface is characterized by the Volmer-Weber mechanism but not by the Stranski-Krastanov mechanism, which is characteristic of the growth on pure Si surface.

2.6. Effect of Growth Rate on Germanium Hut Clusters

As it has been mentioned, several approaches have been exploited to tune the morphology and structural properties
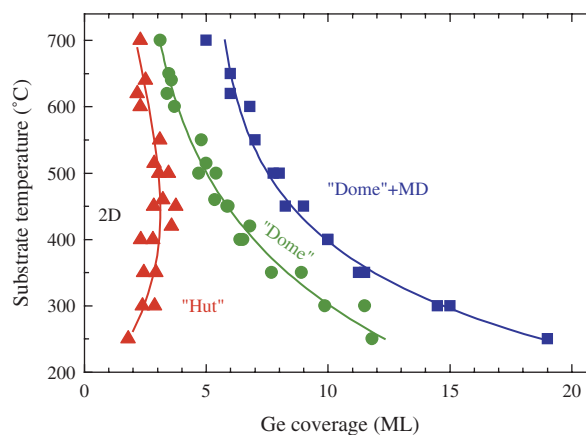
Fig. 4. The structure phase diagram which shows the existence ranges of strained and elastically deformed continuous and island films depending on the Ge thickness and deposition temperature T_s.
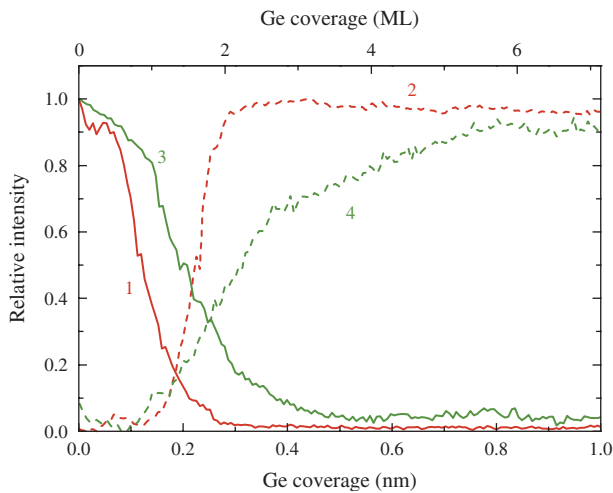
Fig. 5. Relative intensity variations of specular (solid line) and 3D reflections (dashed line) during growth of Ge film on oxidized Si(100) surface at different substrate temperatures (1,2: $T_s = 550$ °C, 3,4: $T_s = 450$ °C.

of Ge QDs, such as manipulating the Ge growth[43] and overgrowth[44] temperatures, the Ge coverage,[45] vertical ordering in QD multilayers,[46–48] surfactant-mediated growth,[49, 50] deposition on vicinal[51] and oxidized[52] surfaces, ion-beam stimulated growth.[53] Another parameter which can control the formation of QDs through the kinetic factors is the dot deposition rate R. Little work has been done on the influence of grown rate on the formation of Ge/Si(001) nanoclusters. Recently, Cho et al.[54] demonstrated the effect of deposition rate on the spatial distribution of dome-shaped Ge islands fabricated at high (600 °C) temperature. McDaniel et al.[55] reported on the increase in

Ge composition as the deposition rate increases also for dome clusters grown at 650 °C. The situation in all cases was complicated by shape transitions between pyramids and domes. In this section we focus on small (<15 nm) Ge nanoislands which were grown at lower temperature (500 °C) and have the form of well-defined hut clusters.

In our experiments, we varied the Ge deposition rate from $R = 0.02$ ML/s to $R = 2$ ML/s while maintaining the substrate temperature, $T_s = 500$ °C, and the Ge coverage, 6 ML, being the same for all samples. The growth temperatures were 500 and 700 °C for the cap and buffer Si layers, respectively. Immediately after the deposition of Ge, the temperature was lowered to $T_s = 350$–400 °C and the Ge islands are covered by a 2-nm Si layer at that temperature. This is necessary to preserve the shape and size of Ge islands with subsequent Si capping at higher T_s.[56]

The scanning tunneling microscopy (STM) of samples without the Si cap layer was employed to assess the morphology of Ge layers. Figure 6 shows a series of images taken at different Ge deposition rates, and the lateral size histograms derived for each image. Although, some of the islands did not have a square base, we used their geometrical mean, $l = \sqrt{a \times b}$ (a and b are the island base lengths), as a convenient measure of their size. The island size distribution were evaluated by measuring the lateral dimensions on 200×200 nm^2 or 200×400 nm^2 scans dependent on the sample until more than 100 islands were taken into consideration. From these data, the width of the size distribution, σ, was calculated as standard deviation,

$$\sigma^2 = \frac{1}{n-1} \sum_{i=1}^{n} (l_i - \langle l \rangle)^2$$
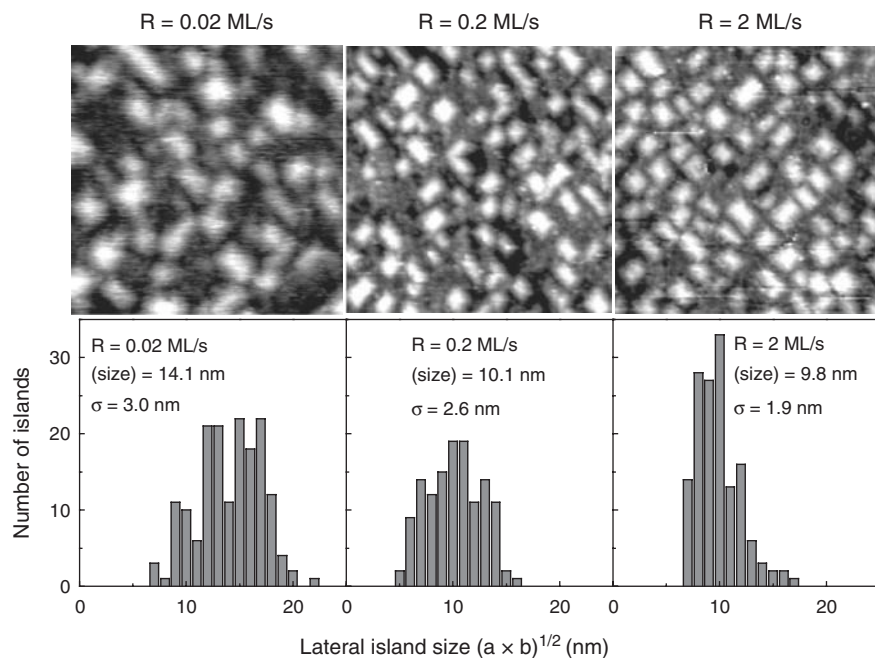
Fig. 6. A series of 150×150 nm^2 STM images and size distribution histograms of Ge islands deposited at a substrate temperature of 500 °C with varying Ge deposition rates. The amount of Ge deposited is 6 ML.

Table I. The surface density of Ge nanoclusters n_{QD}, the Ge island mean size in the growth plane $\langle l \rangle$, and the normalized standard deviation of size distribution $\sigma/\langle l \rangle$ in layers of Ge islands fabricated at different deposition rates R and evaluated from STM images. The amount of Ge deposited d_{eff} and the channeling minimum yield χ_{min} of Ge (χ_{min}^{Ge}) were obtained in Rutherford backscattering/channeling experiments. c is the Ge content and ϵ_{xx} is the average lateral strain in Ge islands determined from Raman measurements.

R (ML/s)	n_{QD} (cm^{-2})	$\langle l \rangle$ (nm)	$\sigma/\langle l \rangle$	d_{eff} (ML)	χ_{min}^{Ge} (%)	c	ϵ_{xx}
0.02	$(1.5 \pm 0.2) \times 10^{11}$	14.1	0.21	5.4 ± 0.5	6.5	0.75 ± 0.03	$-(0.029 \pm 0.002)$
0.2	$(3.2 \pm 0.3) \times 10^{11}$	10.1	0.27	6.1 ± 0.5	4.0	0.83 ± 0.02	$-(0.030 \pm 0.002)$
2	$(3.6 \pm 0.3) \times 10^{11}$	9.8	0.19	7.1 ± 0.5	<3	0.88 ± 0.02	$-(0.035 \pm 0.002)$

where n is the number of islands evaluated, and $\langle l \rangle$ is the mean size. The parameters of Ge QDs distribution obtained from the analysis of STM images are listed in Table I. The average island size decreases with increasing growth rate while the normalized width of size distribution $\sigma/\langle l \rangle$ shows nonmonotonic behavior. Simultaneously, the island density increases with R due to increasing surface concentration of migrating Ge atoms and, thus, the number of island nuclei.

From the STM images, we observe that Ge nanoclusters grown at low deposition rate have a shape of hut clusters bounded by {105} facets with rectangular or square bases in two orthogonal orientations, corresponding to $\langle 100 \rangle$ directions in the substrates. At highest R the formation of elongated islands is suppressed and square-based pyramids dominate, giving rise to a more narrow size distribution. In this case the faster Ge deposition promotes nucleation of additional square-based islands, in preference to diffusion of absorbed Ge atoms to existing islands with subsequent elongating them.

The samples were also characterized by Raman spectroscopy to estimate Ge–Si intermixing effect in Ge QDs and elastic strain in them. We used quasi-backscattering geometry, the incident radiation was polarized along $\langle 100 \rangle$ crystallographic direction, and the scattered light was detected in $\langle 010 \rangle$ polarization. The chosen configuration is allowed for the scattering by longitudinal optical phonons in Ge and Si and forbidden for the two-phonon scattering by transverse acoustical phonons in the Si substrate. Raman spectra of samples with Ge layers grown at different R are shown in Figure 7. A peak observed at ~ 300 cm^{-1} is originated from the optical vibration of Ge–Ge bonds in Ge islands. Another feature at ~ 420 cm^{-1} corresponds to the local Ge–Si vibrations. Based on Raman measurements the Ge–Si intermixing effect can be found from the ratio of the integrated intensities of the Ge–Ge and Ge–Si peaks[57]

$$\frac{I_{Ge-Ge}}{I_{Ge-Si}} = \alpha \frac{(d_{eff} - c)}{2[1 + (c^{-1} - 1)(d_{eff} - c)]} \quad (2)$$

where c is the Ge content in Si$_{1-c}$Ge$_c$ nanoclusters, d_{eff} is the Ge coverage in monolayers, and α is a constant which depends on the experimental conditions. For our experimental setup $\alpha = 2$. The values of c obtained from the Raman spectra and Eq. (2) are listed in Table I. Analysis shows that the average Ge content in the dots

increases with increasing deposition rate. Similar behavior has been previously reported for dome-shaped Ge islands fabricated at 620–650 °C.[55, 58] Since the amount of Ge deposited as well as the growth and overgrowth temperatures are the same for all three samples this finding provides an evidence for that intermixing in self-organized GeSi QDs proceeds by a surface diffusion process[44, 58, 60] rather than a bulk interdiffusion mediated by nonuniform stress fields.[61–63]

The average lateral strain ϵ_{xx} ($= \epsilon_{yy}$) in Ge nanoclusters can be estimated from the Ge–Ge phonon frequency ω_{Ge-Ge} using the following empirical relation[64]

$$\omega_{Ge-Ge} = 300.3 - 32(1 - c) + 12(1 - c)^2 - (450 - 30c)\epsilon_{xx} \quad (3)$$

Here we disregard the size-confinement effect of optical phonons which has to be important for QD's of smaller sizes.[65] This leads to some underestimation of ϵ_{xx}. The data are presented in Table I. The negative strain values indicate a compressive lateral strain within Ge islands. In the sample with largest R the Ge dots are the most strained
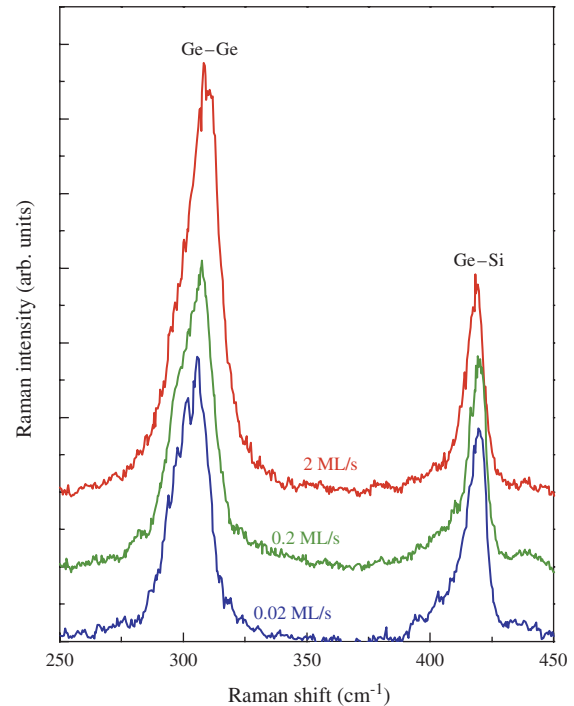
Fig. 7. Raman spectra of the samples with the layers of Ge QDs grown at various Ge deposition rates R.

with ϵ_{xx} being close to the maximum biaxial compressive strain for pure Ge islands in Si(001) (≈ 0.04), whereas when the Ge was deposited at a smaller rate the strain is relaxed due to the Ge–Si intermixing. Moreover, one could expect that the strain would increase with increasing deposition rate on the basis of island–island elastic interactions, i.e., at higher deposition rates, the island density increases so that the islands interact more strongly and relax less effectively via the inhomogeneous strains allowed for isolated islands.

Rutherford backscattering spectroscopy (RBS) was used to estimate the amount of Ge deposited and to characterize qualitatively degree of strain relaxation in Ge layer. RBS experiments were performed at the Research Center Rossendorf using $^4\text{He}^+$ beams with a beam energy of 1.2 MeV. Usually, the channeling minimum yield, χ_{min}, which is a ratio of the backscattering yield when the impinging beam is aligned to a crystallographic axis to that for a random beam incidence, is considered as a measure of the crystalline quality of the films. For a perfect crystal of Si(001), χ_{min} is about 3%. Figure 8 shows the RBS/channeling spectra of samples fabricated at different Ge growth rates R. The thickness of the Si capping layer

is 300 nm when $R = 0.2$ ML/s and 2 ML/s, and 50 nm for the sample with $R = 0.02$ ML/s. In all samples, the Ge coverage is determined to be about 6 ML (see Table I) in a good agreement with the measurements of Ge flux *in situ* by a quartz thickness monitor. The minimum yield from Si matrix taken immediately under the surface peak is about 2.6% independent of the growth conditions and corresponds to a high quality Si structure. An important feature is the reduction of χ_{min} of the buried Ge layer with increasing Ge deposition rate. At $R = 2$ ML/s, χ_{min}^{Ge} approaches that of the best Si crystals, implying that in this case Ge atoms occupy positions of Si atoms and, hence, the Ge layer is nearly fully strained, as also observed in Raman measurements.

3. THEORETICAL CONSIDERATION OF STRAINS AND ELECTRONIC STRUCTURE

3.1. Spatial Distribution of Elastic Strain in a Single Ge Quantum Dot

The physical properties of the SAQD heterostructures depend on a variety of parameters of the QDs (size, shape, lattice mismatch), therefore, the modeling of such objects became a powerful method for understanding the real experimental results and for predicting new ones. Nonuniform elastic strains in heterostructures can cause significant changes in the electrical and optical properties as a result of the energy-spectrum modification by about 0.1 eV (Refs. [66, 67]). Furthermore, nonuniform strains favor the spatial ordering of nanoclusters during the formation of multilayer structures.[68] Therefore, determining the fields of elastic strains is a necessary step in both calculating the band structure of self-arranged QDs and modeling the epitaxy on strained surfaces.

The typical values of strain components are order of relative lattice mismatch of two materials. For Si/Ge heterostructure the relative lattice mismatch is equal to $A_{Ge} - A_{Si}/A_{Si} = 4.2 \times 10^{-2}$, where A_{Ge} and A_{Si} are lattice constants.

Nonuniform elastic strains in heterostructures can cause significant changes in the electron energy spectrum due to the following reason:

(1) unit cell volume modification leads to a shift of energy extremes of Brillouin zone;

(2) unit cell shape modification leads to degeneracy release due to lowering symmetry; and

(3) built-in electric due to deformation (piezoelectric effect).

There is no piezoelectric effect in Ge and Si, so the last term may be omitted.

The strain distribution was found in terms of atomic positions, using valence-force-field (VFF) model with a Keating interatomic potential,[69, 70] previously adopted for self-assembled QDs with different shapes.[71–75] In comparison with the finite-difference[76] and finite-element
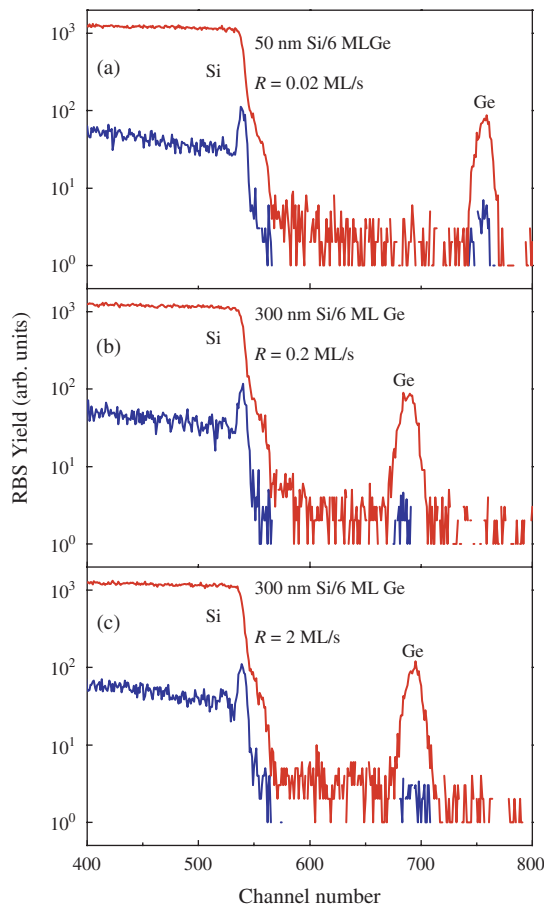
Fig. 8. Random (red lines) and aligned (blue lines) backscattering spectra of Si/Ge/Si(001) heterostructures with Ge nanoclusters deposited at (a) $R = 0.02$ ML/s, (b) $R = 0.2$ ML/s, and (c) $R = 2$ ML/s.

methods,[68, 77–79] which are also often used for the strain calculations of QDs, the advantage of the VFF model is that the strain energies and the positions of all the atoms in a supercell can be obtained. The elastic energy W is given by

$$W = \frac{3}{16} \sum_i \sum_j \frac{\alpha_{ij}}{d_{ij}^2} \left[(\mathbf{r}_i - \mathbf{r}_j)^2 - d_{ij}^2 \right]^2$$

$$+ \frac{3}{8} \sum_i \sum_{j>k} \frac{\beta_{ijk}}{d_{ij}d_{ik}} \left[(\mathbf{r}_i - \mathbf{r}_j)(\mathbf{r}_i - \mathbf{r}_k) + \frac{d_{ij}d_{ik}}{3} \right]^2 \quad (4)$$

where the indices i, j, and k enumerate the atoms, the index i runs over all atoms, j in the first sum runs over the nearest neighbors of the ith atom, and the pair of indices (j, k) in the second sum runs over all pairs of nearest neighbors of the ith atom; $\mathbf{r}$ is the atomic position, d_{ij} is the unstrained bond length, and α_{ij} and β_{ijk} are the force constants in the Keating model.

The problem of finding a set of atomic positions that minimizes W was solved using an original method relying on Green's tensor of the elastic problem.[74] The sizes of the QDs studied are so small that the continuum approximation is inapplicable to the description of the elastic properties of the system. To reduce the calculation error introduced by the finite crystal volume, we sought the deformational field as a convolution of some auxiliary function with the Green's function (Green's tensor) of the elastic atomistic problem.[74] Conventional strain calculation techniques suppose periodic boundary conditions, and a large calculation domain (or "supercell") is needed to reduce the unphysical elastic dot–dot interaction.[73] In contrast to this, the Green function technique is not sensitive to the size of calculation domain, and this allows us to shrink the calculation domain so that only the atoms of the island and its immediate surroundings are involved in the strain calculation. This method yields the distribution of strain at the atomic level for a system containing inclusions of one material in the matrix of another. The crystal anisotropy and the different elastic properties of the medium with inclusions of another phase are taken into account.

Typical pyramidal Ge/Si islands with four {105}-oriented facets and a (001) base, lying on a wetting layer of 0.7 nm thickness, have been under study. The island size (the length of the base side) has been varied from 6 to 15 nm. Ge islands and wetting layer are embedded into the Si matrix (Fig. 9). Figure 10 shows the distribution of the elastic energy per atom in two sections for quantum dots with the base edge length equal to 28 lattice constants (about 15 nm). It is evident that inside the Ge nanocluster the largest stress arises on the periphery of the pyramid base, and the greatest relaxation occurs in the apex of the pyramid. In Si matrix, which surrounds the Ge island, the region near the apex of the pyramid is most stressed.

To show the structure of the deformation field of a quantum dot and its environment, the deformation tensor profile
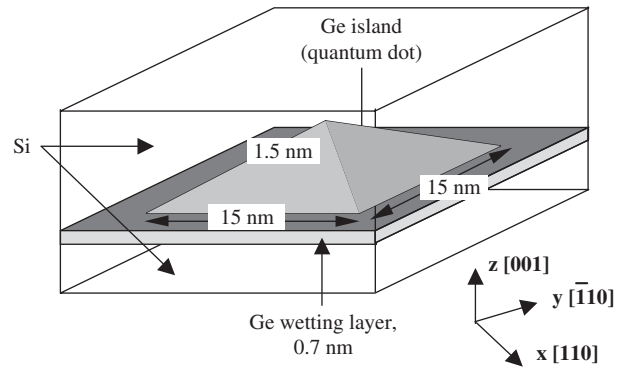

Fig. 9. Geometry of a typical Ge/Si(100) quantum dot used for modeling.

along the pyramid for a 15 nm base size is shown in Figure 11. Inside the pyramid the components of deformation tensor ε_{xx} and $\varepsilon_{yy} < 0$, but $\varepsilon_{zz} > 0$. This means that inside a Ge nanocluster compression occurred in the lateral direction (xy plane). The strain is tensile in the growth z direction.
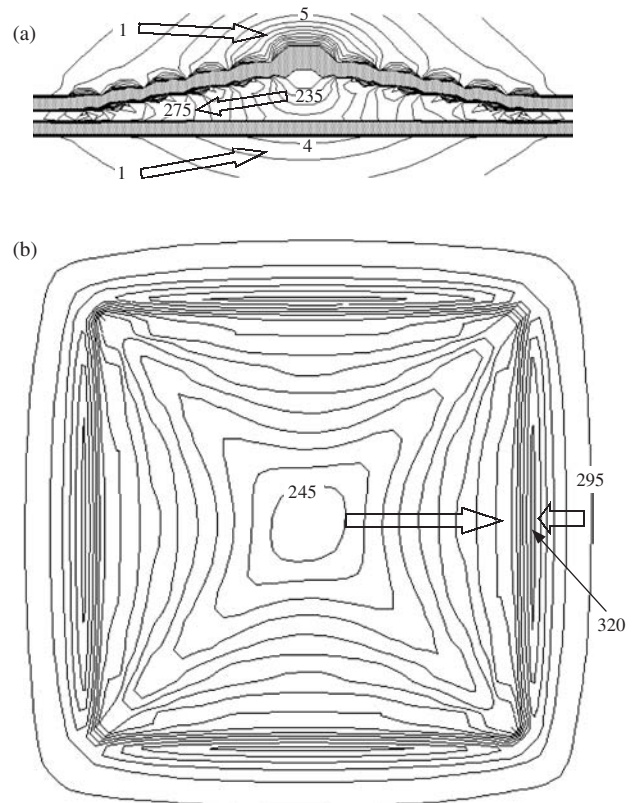
Fig. 10. Space distribution of elastic energy in a Ge/Si quantum dot with the base side of a 28 lattice constants (15 nm): (a) in the (100) plane passing through the pyramid axis; (b) in the (001) plane passing through the center of wetting layer. The numbers indicate the energies in units of 10^{-4} eV per atom; the arrows show the direction of the increasing energy. The spacing of the isolines is 5×10^{-4} eV inside pyramid and 10^{-4} eV outside the pyramid. Isolines are not shown for the Si–Ge interface.
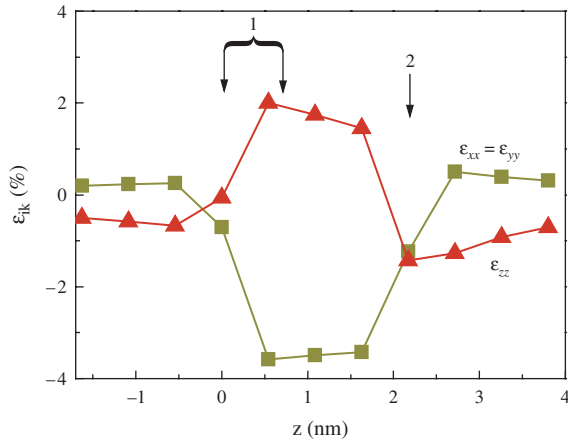
Fig. 11. Depth profiles of the components of the deformation tensor along the symmetry axis of a quantum dot. The step along z is equal to the lattice constant. The label "1" denotes the region occupied by a Ge wetting layer, and the label "2" the position of the pyramid apex.

The analysis of the size dependence of the strain shows the following results:

(a) values of strain components are independent of the dot size over the range of size 10–15 nm in the central region of the dot; this means that the macroscopic value of the strain tensor is already reached in this range;

(b) components of the strain tensor increase in absolute value logarithmically with QD size near the edge of the pyramid base.

This is in agreement with the macroscopic behaviour.

Recently, results obtained in calculating the strain in the Ge/Si QD system with the use of two empirical potentials—Keating and Stillinger-Weber—have been compared.[75] Both methods yield similar results for the lateral tensor components, with a quantitative difference found for the normal tensor components. As a result, the authors[75] recommended that the Stillinger-Weber potential should be used for Ge nanoclusters with a pyramid base smaller than 10 nm.

3.2. Hole Energy Spectrum

In contrast to quantum-well and quantum-wire heterostructures (two-dimensional and one-dimensional systems), the properties of electrons and holes in QD heterostructures cannot be described as a gas of quasiparticles. This case is a fruitful concept of localized states. The electron or hole localization radius in a nanocluster is comparable with the cluster size and frequently it exceeds the Bohr radius of single-impurity atoms with shallow levels in homogeneous bulk semiconductors. However, the energy level in a QD may be deep, and this is one more feature of QDs as deep-level impurity centers. The study of QD heterostructures now constitutes a separate branch of condensed-matter physics.

There are many papers devoted to electronic structure calculation in self-assembled QDs, using the effective

mass approximation,[72, 76, 80–82] pseudopotentials,[73] and the tight-binding (TB) approach.[83] These studies concentrate mainly on the InAs/GaAs heterosystem. Regarding Ge QDs, calculations of energy spectrum have been performed for free-standing spherical Ge nanoclusters[84] and for real pyramidal-type nanoclusters embedded into Si matrix.[85]

The energy spectrum was obtained by means of the sp^3 TB approach, including interactions between nearest neighbours only.[86, 87] Following the work of Chadi,[88] spin–orbit interactions were added to the Hamiltonian. Strain effects are incorporated into the Hamiltonian in two ways:
(1) as changes of interatomic matrix elements and
(2) as the strain-induced mixing of orbitals centered on the same atom.

The changes of interatomic matrix elements due to strain are treated by the generalization of Harrison's d^{-2} law:[89]

$$ijk(d_0)\left(\frac{d_0}{d}\right)^{n_{ijk}}$$

for bond length d and by the Slater and Koster formula[87] for bond angles. There ijk are the two-centre integrals, d_0 is the unstrained bond length and n_{ijk} are the orbital-dependent exponents reflecting the localization of the atomic wavefunctions near the nuclei. For description of the strain influence on mixing of p orbitals we include in the TB Hamiltonian the matrix elements between p orbitals belonging to the same atom:

$$\langle p_x|\widehat{H}|p_y\rangle = -\beta\varepsilon_{xy}; \quad \langle p_x|\widehat{H}|p_z\rangle = -\beta\varepsilon_{xx}$$

$$\langle p_y|\widehat{H}|p_z\rangle = -\beta\varepsilon_{yz}$$

where ε is the strain tensor and β is the model parameter. The mixing of orbitals introduced by above equations allows us to fit the value of shear deformation potential d. Another deformation potential, b, can be varied in a similar way by taking into account the influence of diagonal strain components on energies of orbitals.[89]

Values of parameters were chosen to fit values of heavy-hole and light-hole effective masses and VB deformation potentials.[85] All parameters for Si–Ge bonds are taken as arithmetic means between Si and Ge parameters. Finding eigenvalues of the Hamiltonian is performed by a free-relaxation method analogous to that of Pedersen and Chang.[90] These authors solved the equation:

$$\frac{\partial}{\partial\tau}\big|\psi(\tau)\rangle = -\widehat{H}\big|\psi(\tau)\rangle$$

where τ is imaginary time parameter: $\tau = it$. When $\tau \to \infty$, the solution $|\psi(\tau)\rangle$ will relax towards the lowest-energy state. When fixed the reference energy value E_{ref} in the bandgap the equation is solved by:[85]

$$\frac{\partial}{\partial\tau}|\psi(\tau)\rangle = -(\widehat{H} - E_{ref})^2|\psi(\tau)\rangle$$

In the limit $\tau \to \infty$, this equation gives an eigenstate of $\widehat{H}$ corresponding to an energy level nearest to E_{ref}.
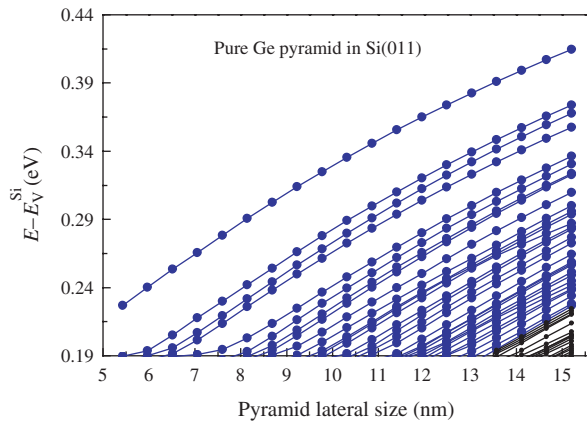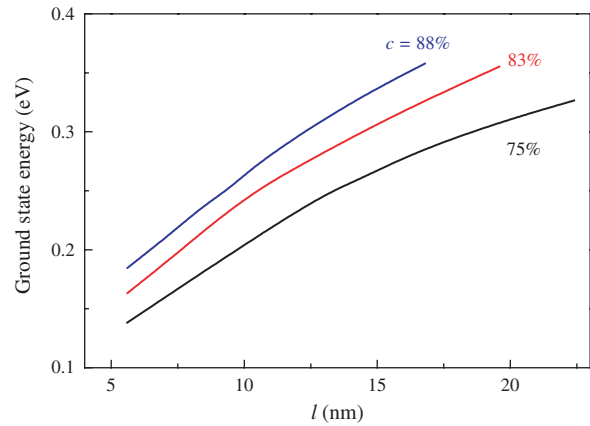
Fig. 12. Energy spectrum of holes in the pyramidal Ge/Si QD as a function of pyramid base size with aspect ratio being constant. The energy is counted with respect to the VB edge in bulk Si. The ground state is upper curve.

Fig. 13. Single-particle energy level of a hole in the ground state in the pyramidal Ge_cSi_{1-c}/Si QD as a function of pyramid base length (l) and Ge content (c) with aspect ratio being constant. The energy is counted with respect to the valence band edge in bulk Si.

Then the value of energy E can be found as $E = \langle\psi(\tau)|\hat{H}|\psi(\tau)\rangle/\langle\psi(\tau)|\psi(\tau)\rangle|_{\tau\to\infty}$.

The geometry and symmetry of problem in itself provides some conclusions about energy spectrum. The geometry of the island results in a strong difference between the values of size quantization energy in the plane of the pyramidal base and in the growth direction. The difference between ground state and some number of excited states therefore has to be determined only by quantization in the base plane. The degeneracy of energy levels is defined by twofold representations of the symmetry group C_{2v}; therefore all the levels are twofold degenerate. The symmetry of the problem is similar to a disc symmetry that allows us to make the assumption that the ground state will be *s*-like and the next two states will be *p*-like.

Calculated energies of the ground state and the next nine excited states of the hole spectrum are presented in Figure 12 as a function of Ge pyramid base size. Energy gap between levels was found to remain practically unchangeable for all sizes in the region 8–15 nm. Figure 13 demonstrates the dependence of the ground-state hole energy level on the Ge content in QDs. The found wave functions are characterized by absence of nodal surfaces perpendicular to the growth direction. From the wave function space configuration one may conclude that the ground state has an *s*-like wave function, and the first two excited states have *p*-like wave functions oriented along [110] and [1̄10]. The next excited states have more complicated configuration. The splitting between two *p*-like states is about 7 meV, and it is caused by two factors: the spin–orbit interaction and the nonequivalence of directions [110] and [1̄10] in the case of an atomically sharp Ge/Si(100) interface. To find the contributions of Ge–Si interface mixing to the splitting of the *p*-levels, the problem was solved with a diffused interface on the base of the pyramid in which the last monolayer of Si under the Ge island contains 33% of Ge, and the first Ge monolayer

in the base of the island contains 33% of Si. In the case of a diffused Ge/Si interface, *p*-like states have no preferred orientation, and splitting between them decreases until ~3 meV. This remaining splitting arises from the spin–orbit interaction.

The absence in wavefunction density of nodal surfaces perpendicular to the growth direction is clear evidence that the difference between all the found states is determined only by quantization in the plane of pyramid base. Therefore optical transitions between these states must be stimulated by irradiation polarized in the base plane, which agrees with experimental results.[37, 91] The weak size dependence of separations between levels allow to conclude that optical transition lines in the QD array will be well resolved even if there is a dispersion of QD sizes within the investigated range of size.

3.3. Wave Functions and *g*-Factor of Holes

The functionality of modern semiconductor devices relies on the control of electronic charge. However, not only do carriers will carry charge, but they also carry spin. Spin transport has one major advantage compared with charge transport: quantum coherence can be maintained on much larger time scales. Several device applications, such as spin transistors, spin memory, and also the spin quantum computer have been proposed to use spin-dependent effects in semiconductors. Semiconductor quantum dots, in which carriers occupy discrete energy states, show various spin-related phenomena, including spin degeneracy, exchange interaction, spin blockade, and Kondo physics (for review, see Refs. [92–96]). Various promising schemes exploiting the spin of carriers in QD have been proposed recently.[6, 97, 98]

For successive manipulation of spin in QD it is necessary to know such fundamental spin properties as the effective *g*-factor, which defines the Zeeman splitting, and the spin relaxation time. On the one hand, these magnitudes

characterize the material properties of the physical object; on the other hand they characterize the individual electron state. The effective g-factor is directly connected with structure of the wave function of the localized carrier in QD. Here this connection will be demonstrated by considering the hole-localized state in the self-assembled Si/Ge quantum dot. From fundamental point of view, this system attracts much interest because, in both, effects of strong quantum confinement and strains define the energy spectrum, and they are responsible for the modification of the g-factor.

In bulk semiconductors, the motion of electrons and holes in the presence of the spin–orbit interaction gives rise to the g-factor, which is significantly modified compared to the free-particle g-factor ($g \approx 2$). As one advances from bulk semiconductors to low-dimensional structures, quantum confinement effects come into play that leads to further strong modification of the g-factor. For electrons, this results in the enhancement[99] and high anisotropy of the Zeeman splitting.[100] A comprehensive theory based on the **kp** method was developed to predict a behavior of the electron g-factor in low-dimensional systems, including quantum wells,[101] wires and dots.[102] Some theoretical results were published for the hole g-factor in quantum wells.[103–105] Calculation of the hole g-factor in quantum dots was made in Refs. [85, 106].

Let us start with qualitative analysis of the principal distinctions between the 2D case of quantum wells and zero-dimensional (0D) case of quantum dots, which are responsible for the g-factor renormalization. A very wide quantum well can be considered as a bulk semiconductor. When the interaction with a magnetic field is small in comparison to the quantization energies (or strain-induced splittings in the case of strained semiconductors), the explicit form of the 8×8 **kp** Hamiltonian allows one to obtain immediately the g-factor components for the hole subbands: for a heavy hole, $g_\parallel = 6k$, $g_\perp = 0$ and for a light hole, $g_\parallel = 2k$, $g_\perp = 4k$, where $g_\parallel$, $g_\perp$ are the components of the effective g-factor tensor for magnetic field parallel and perpendicular to the growth axis z of quantum well, respectively; k is the Luttinger parameter (here the small valence-band parameter q is neglected). For narrower quantum wells, the uncertainty in component of quasi-impulse k_z increases, which leads to the modification of the light-hole g-factor owing to mixing with the split-off VB states and with the conduction band states.[107] The Lande factor of the heavy hole remains unchanged because the heavy-hole states do not mix with the nearest subband states. In the case of ultranarrow quantum wells, the hole g-factor is defined by the parameters of the barrier layer.

In the case of quantum dots, a new modification of the hole g-factor occurs owing to the spatial confinement not only in the growth direction z but also in lateral directions x, y. This leads to the uncertainty in k_x, k_y and, as result, to the strong mixing between the light- and heavy-hole

states.[107] The light- and heavy-hole mixing is left out of account in the theoretical consideration of the 2D system because the states at the bottom of the subband (k_x, $k_y = 0$) are considered usually. In the self-assembled quantum dots formed on the base of strained heterostructures, the significant change of the hole g-factor is caused by the inhomogeneity of strains in QD. If one compares the quantum well and the quantum dot, both with growth direction,[100] then one finds in the dot nonzero strains ε_{xy}, ε_{xz}, ε_{yz}, which lead to the mixing between the light- and heavy-hole states. In quantum wells these strains are absent. So, in the case of quantum dots, the spatial confinement in all three dimensions and the strain inhomogeneity induce the mixing between electronic bands and, as result, lead to a new modification of the hole g-factor.

Here we describe a method developed in Ref. [106] for calculation of the hole g-factor in quantum dots, using the TB approach. This method allows us to calculate the g-factor in quantum dots with different shapes and different confinement potential. It is applicable down to the size of wave function comparable with interatomic distance. This method can be applied also to the electron states in quantum dots.

The application of magnetic field **H** produces the Zeeman interaction energy of the particle, which has effective magnetic moment **M**, which can be written as: $\hat{H} = -\hat{\mathbf{M}} \cdot \mathbf{H}$. The magnetic moment is connected with the angular momentum **J** in following way: $\mathbf{M} = g_0 \mu_B \mathbf{J}$, where μ_B is the Bohr magneton, g_0 is the Lande factor, which is equal to 2 for the particle with only spin magnetism and equal to 1 for the particle with only orbital magnetism. Let us introduce the magnetic moment of a hole $\mathbf{M}_{QD}$, which is measured in unit of the Bohr magneton.

$$\mathbf{M}_{QD} = \mathbf{L} + 2\mathbf{S}$$

where **L** is the orbital angular momentum, and **S** is the spin of the particle. If one needs to calculate g-factor of confined electron in QD, one can use the same expression for magnetic moment where in the sign differs. The Zeeman Hamiltonian for localized carrier in the quantum dot is written as:

$$\hat{H}_{QD}(\mathbf{H}) = -\mu_B \mathbf{H}\hat{\mathbf{M}}_{QD} = -\mu_B(\hat{\mathbf{L}} + 2\hat{\mathbf{S}})\mathbf{H}$$

Even in quantum dots grown along high-symmetry direction [001] the symmetry is not higher than C_{2v} because of the nonequivalence of directions [110] and [$\bar{1}$10]. Hence the energy levels are twofold degenerate in the absence of a magnetic field, and their sublevels constitute the Kramers doublets. For the pair of Kramers-conjugate states the Zeeman contribution to the effective Hamiltonian is written as:

$$\frac{1}{2}\mu_B \hat{\sigma}_i g_{ij} H_j$$

where $\hat{\sigma}_i (i = x, y, z)$ are the Pauli matrices, and for low-symmetry systems the real tensor g_{ij} is characterized by nine linearly independent components.[108] For a hole (or an electron) in the quantum dot with symmetry

not lower C_{2v} one can choose the system of coordinates (x, y, z), where g_{ij} is characterized by three principal values g_{xx}, g_{yy}, g_{zz}.

When the Zeeman interaction is small in comparison to the confinement energy, the g-factor depends only on the magnetic field direction and can be evaluated by means of the first-order perturbation theory:

$$|g| = 2\sqrt{\langle\psi|\mathbf{n}\widehat{\mathbf{M}}_{QD}|\psi\rangle^2 + |\langle\psi|\mathbf{n}\widehat{\mathbf{M}}_{QD}|\psi^*\rangle|^2} \qquad (5)$$

where ψ, ψ^* are the Kramers-conjugate states, $\mathbf{n}$ is the unit vector in the magnetic field direction. Thus, to calculate matrix elements of the operator $\widehat{\mathbf{M}}_{QD}$, one has to determine the wave functions ψ, ψ^* for the hole (or electron) state in the quantum dot. It is assumed, that the magnetic field does not change significantly the wave function of hole in QD, and for calculation of matrix elements, the eigenstates of the non-perturbed Hamiltonian have been used. The eigenvalue problem for the hole states in QD was solved in Ref. [85] with sp^3 tight-binding (TB) approach, including interactions between nearest neighbours only.[86, 87] The set of atomic orbital $\{s, p_x, p_y, p_z\}$ for each atom was taken, and state vector length was equal to (number of atoms) × (number of orbitals per atom). Following Chadi[88] the spin–orbit interaction was added to the Hamiltonian. Strain effects were incorporated into Hamiltonian in two ways: as changes of interatomic matrix elements[87, 89] and as the strain-induced mixing of orbitals centered on the one atom.[85] The wave function was found with free-relaxation technique. The component of calculated state vector $\psi_{\alpha N}$ represents the amplitude of the probability to find hole (or electron) on the α-orbital of the atom number N, where the index α runs over the set $\{s, p_x, p_y, p_z\}$.

Because the state vectors were found as linear combinations of atomic orbitals, one should determine the expression for $\widehat{\mathbf{M}}_{QD}$ in the representation of atomic orbitals. The angular momentum of electron on the α-orbital of the atom number N can be written as

$$\widehat{L}_i = \frac{1}{\hbar} e_{ijk} \hat{p}_j \hat{r}_k$$

where e_{ijk} is the unit antisymmetric tensor; indices i, j, k run over the set $\{x, y, z\}$. The momentum operator $\hat{\mathbf{p}} = m\hat{\mathbf{r}}$ can be expressed via the coordinate operator $\hat{\mathbf{r}}$ as

$$\hat{\mathbf{p}} = \frac{im}{\hbar}(\widehat{H}_0\hat{\mathbf{r}} - \hat{\mathbf{r}}\widehat{H}_0)$$

where m is the mass of the free electron, $\widehat{H}_0$ is the Hamiltonian without spin–orbit interaction. This equation can be deduced from the time differentiation rules for operators.[109] Then the angular momentum operator can be written as

$$\widehat{L}_i = \frac{im}{\hbar^2} e_{ijk} \hat{r}_j \widehat{H}_0 \hat{r}_k$$

Hence the magnetic momentum of hole on the α-orbital can be written as

$$(\widehat{M}_{QD})_i = \widehat{L}_i + 2\widehat{S}_i$$

But one cannot use this equation directly for calculating the matrix elements $\langle\psi|\widehat{\mathbf{M}}_{QD}|\psi\rangle$, $\langle\psi|\widehat{\mathbf{M}}_{QD}|\psi^*\rangle$ because the state vectors ψ, ψ^* are calculated in the TB approach and the coordinate operator $\hat{\mathbf{r}}$ has no physical sense in this approach. It is replaced by coordinate operator $\widehat{\mathbf{R}}$ of the atom with considered orbital

$$\widehat{L}_i = \frac{im}{\hbar^2} e_{ijk} \widehat{R}_j \widehat{H}_0 \widehat{R}_k \qquad (6)$$

Replacing $\hat{\mathbf{r}} \to \widehat{\mathbf{R}}$ leads to losing some part of the angular momentum. The remaining part (Eq. (6)) is connected with the envelope function. It is the orbital momentum caused by localization of the carrier in the quantum dot. To obtain the total magnetic momentum $\mathbf{M}_{QD}$ one should take into account the internal orbital momentum corresponding to the atomic orbital. Also one should remember about renormalization of $g_0 = 2$ caused by the interaction of electronic bands.

The hole state in the quantum dot is built mainly from states of the valence band (VB), namely heavy hole band (HH), and the light hole band (LH). But the nearest electronic bands also make contribution to the state in quantum dot. The split-off valence band (SO) and the conduction band (CB) are important for the correct magnetic momentum calculation for hole (or electron) state in QD. The TB approach, which used for solving the eigenvalue problem, not only takes into account the interaction of the electronic bands near band gap but also includes the interaction of the HH states with the higher conduction bands. The contribution of the remote bands in the hole state in QD are negligible. The wave function of hole (or electron) can be presented in the form:

$$|\psi\rangle = A_{CB}(\mathbf{R})|CB\rangle + A_{HH}(\mathbf{R})|HH\rangle$$
$$+ A_{LH}(\mathbf{R})|LH\rangle + A_{SO}(\mathbf{R})|SO\rangle$$

where $|CB\rangle, \dots, |SO\rangle$ are the Bloch functions, and coefficients $A_{CB}, \dots, A_{SO}$ can be considered as envelopes and reflect the contributions of the corresponding bands in the state in QD. Every component of the wave function has intrinsic effective spin and interacts with the magnetic field according to Eqs. (7)–(11) in the following paragraphs.

For the degenerate valence band states (Γ_8 band), the Zeeman interaction can be written in the form

$$\widehat{H}(\mathbf{H}) = 2\mu_B(k(\widehat{\mathbf{J}}\mathbf{H}) + q(\widehat{J}_x^3 H_x + \widehat{J}_y^3 H_y + \widehat{J}_z^3 H_z)) \qquad (7)$$

where $\mathbf{J}$ is the hole effective angular momentum ($J = \frac{3}{2}$), and k and q are Luttinger parameters. This equation automatically takes into account the internal orbital momentum corresponded to the atomic orbital.

The strains and confinement effects in the quantum dot lead to the lifting of the valence band degeneracy.

It is convenient for states in the HH band to use an effective HH spin or pseudospin $S_{hh} = \frac{1}{2}$ to describe their sublevels: as in Ref. [104], we identify $J_z = -\frac{3}{2}$ with $(S_{hh})_z = -\frac{1}{2}$, and $J_z = \frac{3}{2}$ with $(S_{hh})_z = +\frac{1}{2}$.

In terms of the pseudospin $\mathbf{S}_{hh}$, the Zeeman Hamiltonian is written as

$$\widehat{H}(\mathbf{H}) = \mu_B g_{hh}(\widehat{\mathbf{S}}_{hh}\mathbf{H}) \qquad (8)$$

The same one can make for states in the LH band: $J_z = -\frac{1}{2}$ is identified with $(S_{lh})_z = -\frac{1}{2}$, and $J_z = +\frac{1}{2}$ is identified with $(S_{lh})_z = +\frac{1}{2}$. The Zeeman interaction in the LH band is

$$\widehat{H}(\mathbf{H}) = \mu_B g_{lh}(\widehat{\mathbf{S}}_{lh}\mathbf{H}) \qquad (9)$$

From comparison (7) and (8) one can conclude that for the heavy hole state, which have $J = \frac{3}{2}$, $J_z = \pm\frac{3}{2}$, the Lande g-factor is $g_{hh} \sim 6k$ (the term with small parameter q can be neglected).

For the CB and SO states, the Zeeman interaction can be written in terms of the effective spin: $\mathbf{S}_c$, $\mathbf{S}_{so}$. For states in the conduction band,

$$\widehat{H}(\mathbf{H}) = \mu_B g_c(\widehat{\mathbf{S}}_c\mathbf{H}) \qquad (10)$$

for states in the split-off band,

$$\widehat{H}(\mathbf{H}) = \mu_B g_{so}(\widehat{\mathbf{S}}_{so}\mathbf{H}) \qquad (11)$$

where g_c is the g-factor of an electron in the conduction band, g_{so} is the g-factor of a hole in the split-off band, and operators $\widehat{\mathbf{S}}_c$, $\widehat{\mathbf{S}}_{so}$ can be expressed via the Pauli matrices $\hat{\sigma}_x$, $\hat{\sigma}_y$, $\hat{\sigma}_z$, $\widehat{S}_i = \frac{1}{2}\hat{\sigma}_i$.

The total energy of the interaction with magnetic field, including the interaction of the orbital momentum $\mathbf{L}$ is written as the sum:

$$\widehat{H}(\mathbf{H}) = 2\mu_B(k(\widehat{\mathbf{J}}\mathbf{H}) + q(\widehat{J}_x^3 H_x + \widehat{J}_y^3 H_y + \widehat{J}_z^3 H_z))$$
$$+ \mu_B g_{so}(\widehat{\mathbf{S}}_{so}\mathbf{H}) + \mu_B g_c(\widehat{\mathbf{S}}_c\mathbf{H}) + \mu_B \widehat{\mathbf{L}}\mathbf{H} \qquad (12)$$

where $\widehat{\mathbf{L}}$ is given by (6). From this equation one can extract the magnetic moment $\mathbf{M}_{QD}$:

$$(\widehat{M}_{QD})_i = 2k\widehat{J}_i + 2q\widehat{J}_i^3 + g_{so}(\widehat{S}_{so})_i + g_c(\widehat{S}_c)_i + \widehat{L}_i \qquad (13)$$

Substituting Eq. (6) into Eq. (13) we finally arrive at the following main equation:

$$(\widehat{M}_{QD})_i = 2k\widehat{J}_i + 2q\widehat{J}_i^3 + g_{so}(\widehat{S}_{so})_i + g_c(\widehat{S}_c)_i$$
$$+ \frac{im}{\hbar^2}e_{ijk}\widehat{R}_j\widehat{H}_0\widehat{R}_k \qquad (14)$$

Now the g-factor of a hole (or an electron) can be calculated in the quantum dot utilizing Eqs. (5) and (14).

The localized states in the Ge quantum dot are formed mainly from valence band states and represent the superpositions of states $|\frac{3}{2}, \pm\frac{3}{2}\rangle$, $|\frac{3}{2}, \pm\frac{1}{2}\rangle$, $|\frac{1}{2}, \pm\frac{1}{2}\rangle$ (the states $|J, J_z\rangle$ are the eigenstates of effective angular momentum J and its projection J_z). The states $|\frac{3}{2}, \pm\frac{3}{2}\rangle$ can be considered as heavy hole states, $|\frac{3}{2}, \pm\frac{1}{2}\rangle$ can be considered as light hole states, $|\frac{1}{2}, \pm\frac{1}{2}\rangle$ can be considered as split-off hole states. The strain distribution in quantum dot in general consists of the compression in the plane of the

pyramid base and the extension in the growth direction z. In the bulk, uniaxially extended semiconductor strains lift the degeneracy of the valence band, making the heavy hole band the highest valence band.[110] For this reason the contribution of the heavy hole states in the ground state in QD must be predominant. The same conclusion follows from estimation of the quantization energies for heavy and light hole. Heavy hole has the much bigger effective mass and the lower quantization energy (compared to those for light hole).

Let us consider the external magnetic field applied parallel to the growth direction, $\mathbf{H} \parallel z$. The interaction energy is determined by the projection of the magnetic momentum on the external field direction (i.e., on the z-direction). Therefore for calculation of the hole g-factor, one needs to evaluate the matrix elements of operators $\widehat{J}_z$, $\widehat{J}_z^3$, $(\widehat{S}_{so})_z$, $(\widehat{S}_c)_z$, $\widehat{L}_z$. One can estimate the hole g-factor based only on the results of the wave function expansion in the basis $|J, J_z\rangle$, that is, the expansion $|\psi\rangle = \Sigma_n A_n(\mathbf{R})|n\rangle$, where n runs over the set $\{|\frac{3}{2}, \pm\frac{3}{2}\rangle, |\frac{3}{2}, \pm\frac{1}{2}\rangle, |\frac{1}{2}, \pm\frac{1}{2}\rangle\}$ (the heavy hole states, the light hole states and the split-off hole states). The contribution of CB states is omitted because of its small value ($\sim 0.5\%$) according to our calculations. The results of the wave function expansion for the ground hole state in the quantum dot with size $l = 15$ nm and $h = 1.5$ nm are presented in Table II.

The contribution of the states with $J_z = \pm\frac{3}{2}$ (the heavy hole states) is about $\sim 84\%$ of the ground state. The rest belongs to the states with $J_z = \pm\frac{1}{2}$ (the light and split-off hole states). From the Table II one can see that the state $|\uparrow\rangle$ is formed in general by the states with $J_z = +\frac{3}{2}$ and $J_z = -\frac{1}{2}$ and the state $|\downarrow\rangle$ consists of the states with $J_z = -\frac{3}{2}$ and $J_z = +\frac{1}{2}$. The angular momentum projection of heavy hole part is antiparallel to that of the light and split-off hole part. This can be explained by symmetry considerations. The combination of the states with $J_z = +\frac{3}{2}$ and $J_z = -\frac{1}{2}$ remains the same under symmetry transformation of group C_{2v} (π-rotation). The part with $J_z = \pm\frac{1}{2}$ reflects the contributions of the states $|\frac{3}{2}, \pm\frac{1}{2}\rangle$, $|\frac{1}{2}, \pm\frac{1}{2}\rangle$, either of the two is about $\sim 8\%$ of the ground hole state. That is the LH and SO states make the equal contributions to the ground hole state.

If the ground hole state in the quantum dot was formed by the heavy hole states only, the spin-up state $|\uparrow\rangle$ would correspond to $J_z = +\frac{3}{2}$, and the spin down state $|\downarrow\rangle$ would correspond to $J_z = -\frac{3}{2}$. The Zeeman splitting in the

Table II. Results of wave function expansion in the basis $|J, J_z\rangle$ for two Zeeman sublevels $|\uparrow\rangle$, $|\downarrow\rangle$ of the ground hole state in Ge quantum dot. The sizes of Ge nanocluster: the height $h = 1.5$ nm, the length of the base side $l = 15$ nm. The contribution of CB states ($\sim 0.5\%$) is omitted.

$\|J, J_z\rangle$	$\|\frac{3}{2}, \frac{3}{2}\rangle\%$	$\|\frac{3}{2}, \frac{1}{2}\rangle\%$	$\|\frac{3}{2}, -\frac{1}{2}\rangle\%$	$\|\frac{3}{2}, -\frac{3}{2}\rangle\%$	$\|\frac{1}{2}, \frac{1}{2}\rangle\%$	$\|\frac{1}{2}, -\frac{1}{2}\rangle\%$
$\|\uparrow\rangle$	83.67	2.26	4.7	0.08	1.17	8.11
$\|\downarrow\rangle$	0.08	4.7	2.26	83.67	8.12	0.67

magnetic field $\mathbf{H} \parallel z$ would be defined as

$$E(H_z) = 2\mu_B \langle (M_{QD})_z \rangle H_z$$
$$= 2\mu_B H_z \left(2k \cdot \frac{3}{2} + 2q \cdot \frac{27}{8} + \langle L_z \rangle \right) \quad (15)$$

where $\langle (M_{QD})_z \rangle$, $\langle L_z \rangle$ are average z-components of the magnetic and orbital momentum in the state $|\uparrow\rangle$. For estimation, the term with small parameter q is neglected in the Eq. (15), $|q| = 0.06$ (Ref. [111]). If one takes into account the admixture of the light and split-off hole states with $J_z = \pm\frac{1}{2}$, the Eq. (15) turns into following:

$$E(H_z) = 2\mu_B H_z 2k(a^2 - d^2) \cdot \frac{3}{2}$$
$$+ 2\mu_B H_z (2k(b^2 - c^2) + g_{so}(e^2 - f^2)) \cdot \frac{1}{2}$$
$$+ 2\mu_B H_z \langle L_z \rangle$$

where coefficients a^2, b^2, c^2, d^2 are probabilities of finding in the state $|\uparrow\rangle$ hole with $J = \frac{3}{2}$ and $J_z = \frac{3}{2}$, $J_z = \frac{1}{2}$, $J_z = -\frac{1}{2}$, $J_z = -\frac{3}{2}$ correspondingly. The coefficients e^2, f^2 are probabilities of finding hole with $J = \frac{1}{2}$ and $J_z = \frac{1}{2}$, $J_z = -\frac{1}{2}$ correspondingly. They all are connected with coefficients $A_i(\mathbf{R})$, $i \in \{HH\uparrow, HH\downarrow, LH\uparrow, LH\downarrow, SO\uparrow, SO\downarrow\}$ in following way:

$$a^2 = \int A_{HH\uparrow}^2(\mathbf{R})\, d\mathbf{R}, \quad b^2 = \int A_{LH\uparrow}^2(\mathbf{R})\, d\mathbf{R}$$

$$c^2 = \int A_{LH\downarrow}^2(\mathbf{R})\, d\mathbf{R}, \quad d^2 = \int A_{HH\downarrow}^2(\mathbf{R})\, d\mathbf{R}$$

$$e^2 = \int A_{SO\uparrow}^2(\mathbf{R})\, d\mathbf{R}, \quad e^2 = \int A_{SO\downarrow}^2(\mathbf{R})\, d\mathbf{R}$$

For quantum dots with size $l = 15$ nm and $h = 1.5$ nm, these probabilities are: $a^2 \approx 0.84$, $b^2 \approx 0.02$, $c^2 \approx 0.05$, $d^2 \approx 0$, $e^2 \approx 0.01$, $f^2 \approx 0.08$.

If one excludes the term with $\langle L_z \rangle$, the estimation of the hole g-factor can be done by means following equation:

$$g_{zz} \approx 6k(a^2 - d^2) + 2k(b^2 - c^2) + g_{so}(e^2 - f^2) \quad (16)$$

The valence-band parameters for bulk Ge and Si are well known. The Luttinger parameter k is known from high-precision experiments[111] $k = -3.41 \pm 0.03$, but the magnitude of g_{so} is known with poor accuracy, $g_{so} = -10 \pm 3$ (Ref. [112]). However, the g-factor is crucially depended on the magnitude of k and weakly depended on the g_{so}, and this fact does not lead to the significant error in calculations. More significant correction of g-factor can be expected from the difference of parameter k in the strained Ge from its value in unstrained Ge. Experimental values for the Luttinger parameters of strained Ge do not exist in the literature. Therefore, we have used a nonlinear interpolation scheme[113] along the concepts of Lawaetz,[114] which exactly reproduces the experimental values of the Luttinger parameters of both Si and Ge. Parameter k is mainly

depended from $\mathbf{k} \cdot \mathbf{p}$ couplings of the topmost valence band with the s and p antibonding conduction-band states with energy gap E_0 and E_0', respectively. This allows k to be expressed in the following form:

$$k = \frac{1}{6}\frac{E_p}{E_0} - \frac{1}{6}\frac{E_p'}{E_0'} + \bar{k} \quad (17)$$

where

$$E_p = \frac{2}{m} |\langle X|P_x|\Gamma_2'\rangle|^2$$

$$E_p' = \frac{2}{m} |\langle X|P_y|\Gamma_{15}'\rangle|^2$$

are the principal interband momentum matrix elements, $|X\rangle$ is the yz-type wave function of the Γ_{25}' valence-band states in the case where spin–orbit coupling is neglected, and $\bar{k}$ is expressed by two constants (G and H_2 in Ref. [114]). The estimation of fundamental gap E_0 in strained Ge following Van de Walle[110] gives $E_0 \simeq 1.2$ eV. This value is close to E_0 obtained for pseudomorphic Ge film by theoretical study of strained $Si_{1-c}Ge_c$ alloys, coherently grown on a Si(001).[115]

The gap E_0' in strained Ge can be found follow Lawaetz by scaling E_0' for initial Ge according to

$$E_0'(s) = E_0'(i)\left[\frac{a(s)}{a(i)}\right]^{-1.92}$$

where $a(s)$, $a(i)$ are the lattice constants for strained and unstrained Ge. The momentum matrix elements are inversely proportional to the lattice constant. Hence $E_p(s)$ and $E_p'(s)$ are obtained by scaling their values for unstrained Ge with

$$\delta(s) = \{1 + 1.23[D(s) - 1]\}\left[\frac{a(i)}{a(s)}\right]^2$$

where $D(s)$ the factor introduced by Van Vechten[116] to account for d electron effects. For unstrained Ge, $D(i) = 1.25$. To determinate the $D(s)$ for strained Ge, we use the method proposed by Van Vechten and obtain the value $D(s) = 1.13$. Thus, using $E_0'(Ge) = 3.16$ eV, $E_p(Ge) = 26.3$ eV, $E_p'(Si) = 14.4$ eV,[114] we have calculated from Eq. (17) the Luttinger parameter $k = -2.75$.

Substituting $k = -2.75$, $g_{so} = -10$ in Eq. (16), one can find $|g_{zz}| \approx 13$ for Ge nanocluster with $h = 1.5$ nm and $l = 15$ nm. The numerical calculation of the hole g-factor by means Eq. (5) with eigenstates obtained in TB approach gives the value $|g_{zz}| = 12.28$. Analogously, we have calculated the principal values of the g-tensor for magnetic field lying in the plane of the pyramid base $|g_{xx}| = 0.69 (\mathbf{H} \parallel [110])$, $|g_{yy}| = 1.59 (\mathbf{H} \parallel [\bar{1}10])$. The comparison of the obtained value g_{zz} with the g-factor of heavy hole in the bulk germanium $|g_{hh}| \approx 6k = 20.46$ shows that the effects of quantum confinement and strains lead to the decrease of the hole g-factor. This demonstrates the suppression of the spin–orbit interaction due to the admixture of the light and split-off holes states.
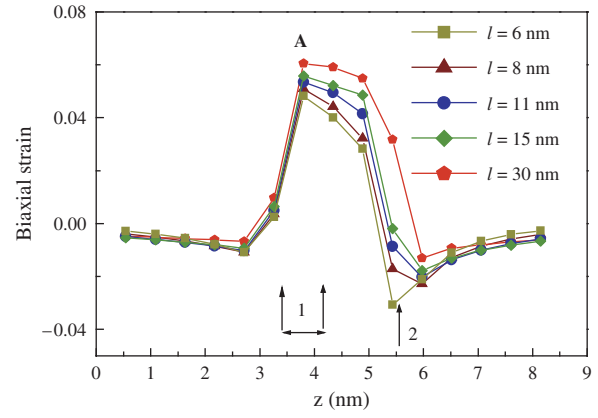
REVIEW
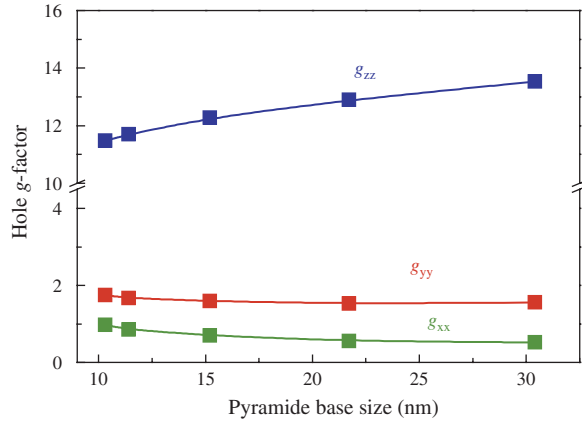
Fig. 14. The g-factor of ground state in Ge quantum dot as a function of the QD lateral size. The Ge nanocluster height is $h = 1.5$ nm.

Fig. 15. Profiles of biaxial strain $\varepsilon_{zz} - \frac{1}{2}(\varepsilon_{xx} + \varepsilon_{yy})$ along the symmetry axis z of a quantum dot at different lateral sizes l of Ge nanocluster. The region "1" corresponds to wetting layer and the point "2" corresponds to the tip of the pyramid. The maximum value of biaxial strain is reached in wetting layer (point "A").

To estimate the orbital momentum contribution we have calculated the hole g-factor dropped all terms in Eq. (14) except the last. In this case, the calculation gives the value of the g-factor one order smaller than for case of total moment $\mathbf{M}_{QD}$: $|g_{zz}| = 0.59$. So, the hole g-factor is mainly determined by the effective angular momentum $\mathbf{J}$, but not by the orbital momentum $\mathbf{L}$.

The hole g-factor of the ground state in QD demonstrates a well pronounced anisotropy: g_{zz} is one order larger than g_{xx} and g_{yy}. Calculation of the hole g-factor for Ge nanocluster with larger lateral size l, keeping the nanocluster height h constant, shows the stronger anisotropy of the g-factor (Fig. 14). For calculating this size dependence, the parameter $k = 2.75$ for strained Ge was used. The change of k with size of Ge nanocluster was not taken into account. Simple estimation of k in dependence on strain shows that this parameter slightly rises with nanocluster size l. So, if this fact was considered, it would be led to the stronger anisotropy enhancement with lateral size l.

The reason of the g-factor anisotropy lies in the similarity between the ground hole state and the heavy hole state $|\frac{3}{2}, \pm\frac{3}{2}\rangle$, which has the transverse components of the g-factor close to zero.[104] The ground hole state becomes closer to the heavy hole state with the increase of the nanocluster lateral size that leads to the anisotropy enhancement. The numerical calculation confirms this assumption: the contribution of the heavy hole state in the ground state in QD goes up with increasing of the nanocluster size l (Fig. 14). For example, when the size l changes from 15 nm to 30 nm at the height $h = 1.5$ nm, the contribution of the heavy hole state increases from 83.7% to 86%. The g-factor anisotropy becomes stronger: $|g_{zz}|$ goes up to 13.53, and transverse components decrease to $|g_{xx}| = 0.52$, $|g_{yy}| = 1.56$.

The contribution of the states with $J_z = \pm\frac{3}{2}$ (the $|\frac{3}{2}\rangle$-states) with nanocluster size l, was considered with previous results of the spatial strain distribution in Ge nanocluster and their environment.[74] When the lateral nanocluster size l increases with $h = $ constant, the biaxial

strain $\varepsilon_{zz} - \frac{1}{2}(\varepsilon_{xx} + \varepsilon_{yy})$ in the Ge nanocluster increases with the ratio l/h (Fig. 15). This leads to higher strain splitting between the light and heavy hole states.[110] The admixture of the states with $J_z = \pm\frac{1}{2}$ (the $|\frac{1}{2}\rangle$-states) is decreased. It is surprising that the dependencies of these characteristics on the nanocluster size l are identical (Fig. 16). This means that the $|\frac{3}{2}\rangle$-state contribution is a nearly linear function of biaxial strain. It is difficult to explain this result in frame of simple qualitative model. But it demonstrates that the strain is the main reason determining the change of the contribution ratio between the $|\frac{3}{2}\rangle$-state and the $|\frac{1}{2}\rangle$-state in considered case ($h = $ const, l is changed).

The calculation of the hole g-factor with increasing of both sizes l and h, keeping the proportions of the pyramid constant ($h/l = \frac{1}{10}$), gives more higher anisotropy of the g-factor. For example, for $l = 30$ nm, $h = 3$ nm the principal values of the g-tensor are the following: $|g_{zz}| = 17.43$, $|g_{xx}| = 0.12$, $|g_{yy}| = 1.06$. In this case, the contribution of the heavy hole state goes up to 90%, which leads to this high anisotropy. The strong increase of g_{zz} is caused
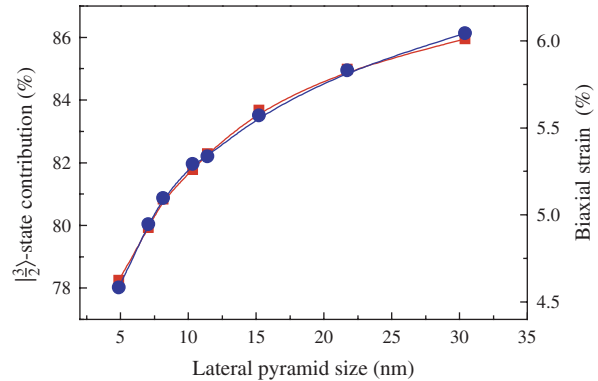
Fig. 16. Maximum value of biaxial strain at point "A" in Figure 15 (red symbols) and the $|\frac{3}{2}\rangle$-state contribution (blue symbols) as a function of lateral pyramid size. The height of pyramid is fixed as $h = 1.5$ nm.

136

by reducing the part of wave function penetrating in Si. In this case, the wave function is located almost only in the Ge region, and Si does not an affect on the g-factor value. In the case of nanocluster with $h = 1.5$ nm, the influence of Si environment is stronger. When proportions of the pyramid ($h/l = \frac{1}{10}$) are preserved, strains can not be considered as the main reason determining the $|\frac{3}{2}\rangle$-state contribution. The spatial distribution of strains and their magnitude in the quantum dot are not significantly changed increasing nanocluster sizes. The strain splitting between the light and heavy hole states remains the same. The confinement energy determined the change of $|\frac{3}{2}\rangle$-state contribution in this case is.

The obtained size dependence of the g-factor proves the correctness of our approach. Indeed, when the lateral size l increases, the Ge nanocluster transforms into the pseudomorphic-strained Ge film. The inhomogeneity of the strain distribution disappears; the strains ε_{xy}, ε_{xz}, ε_{yz} are absent. The uncertainty in k_x, k_y becomes equal to zero for the state on the bottom of the subband. All this changes suppress the mixing of the heavy hole state with the nearest band states. And as result, the g-factor of the ground hole state must trend toward the heavy hole g-factor in strained Ge film, $g_{hh} \approx 6k = 16.5$. But for thin Ge layer (thickness is a few nanometers), the g-factor of hole state is affected by Si surrounding Ge because the tails of wave function penetrate into Si. Namely, for Ge layer with thickness $h = 2.2$ nm the z-component of g-tensor is equal to $|g_{zz}| = 13.11$. It is obvious that g_{zz} does not reach the value of heavy hole g-factor in stained germanium. Moreover, this value is smaller than $|g_{zz}| = 13.53$ for Ge nanocluster with $l = 30$ nm, $h = 1.5$ nm. This effect is caused by vanishing the contribution of orbital momentum **L** for 2D Ge layer. These given values of g-factor have been obtained for Ge nanocluster with atomically sharp Ge/Si interface. The Ge/Si mixing may be induced in the calculation procedure in the following way: each of atoms in the crystal lattice is substituted with probability two-thirds for one from its four neighbors. So, in this manner, one can obtain the diffused interface with graded changes of the Ge content within three monolayers. The calculation with diffused Ge/Si interface gives the following results: transverse components undergo a drastic change, for example, for the Ge nanocluster with lateral size $l = 15$ nm, $|g_{xx}|$ decreases from 0.69 to 0.6, and $|g_{yy}|$ decreases from 1.59 to 0.33. But the longitudinal component of the g-factor remains unchanged practically, $|g_{zz}| = 12.37$. So, in the case of diffused interface, the g-factor anisotropy enhances in comparison to the case of the atomically sharp interface. This is probably caused by the effective increase of the Ge nanocluster size.

For magnetic field **H** $\parallel z$, the Zeeman transition probability depends on the magnitude of the angular momentum projection J_z. For the state with $J_z = \pm\frac{3}{2}$ the transitions between Zeeman sublevels are forbidden. For allowed transitions, the condition $\Delta J_z = \pm 1$ must be satisfied.

The admixture of the states with $J_z = \pm\frac{1}{2}$ leads to the weakening of this restriction. Therefore, the Zeeman transitions probability becomes higher for nanoclusters with smaller lateral size l. For any chosen direction of the magnetic field, the Zeeman energy is determined by the projection J_h of the angular momentum on the direction **h**. When the direction of **h** is not parallel with principal axis of symmetry z, the states $|J, J_h\rangle$ cannot be considered as the heavy, light, and split-off hole states. For example, the state $|\frac{3}{2}, \pm\frac{1}{2}\rangle$ with $J_h = \pm\frac{1}{2}$ cannot be considered as the light-hole state. The state $|J, J_z\rangle$ is transformed into $|J, J_h\rangle$ in following way:

$$|J, J_h\rangle = \sum_{J_z} R^J_{J_z J_h}(\theta, \varphi)|J, J_z\rangle$$

where θ, φ are the azimuth and polar angles of the vector **h** in the coordinate system (x, y, z), and the matrix **R** can be expressed via standard rotation matrix: $R^J_{J_z J_h}(\theta, \varphi) = D^J_{J_z J_h}(0, -\theta, -\varphi)$.[117]

In the special case $\theta = \pi/2$, $\varphi = 0$, the magnetic field lies in the plane of the nanocluster base and coincides with axis x. Let us consider the heavy hole state with $J_z = \frac{3}{2}$, without any admixture. In the representation $|J, J_z\rangle$, the vector of this state can be written in the following form:

$$|\psi\rangle = a\left|\frac{3}{2}, \frac{3}{2}\right\rangle + b\left|\frac{3}{2}, \frac{1}{2}\right\rangle + c\left|\frac{3}{2}, -\frac{1}{2}\right\rangle + d\left|\frac{3}{2}, -\frac{3}{2}\right\rangle$$

$$= \begin{pmatrix} a \\ b \\ c \\ d \end{pmatrix} = \begin{pmatrix} 1 \\ 0 \\ 0 \\ 0 \end{pmatrix}$$

where squares of coefficients a^2, b^2, c^2, d^2 reflect contributions of the states with corresponding J_z, $a^2 + b^2 + c^2 + d^2 = 1$. Under application of $R^J_{J_z J_h}(\pi/2, 0)$, the heavy hole state transforms into superposition of the states with $J_h = \pm\frac{3}{2}$ and $J_h = \pm\frac{1}{2}$:

$$\begin{pmatrix} 1 \\ 0 \\ 0 \\ 0 \end{pmatrix} \rightarrow \begin{pmatrix} \sqrt{1/8} \\ \sqrt{3/8} \\ \sqrt{3/8} \\ \sqrt{1/8} \end{pmatrix}$$

From this equation it is clear, that the contribution of the state with $J_h = +\frac{1}{2}$ is $\frac{3}{8}$ of whole state, the state with $J_h = -\frac{1}{2}$ makes the same part. They contain together 75%. So, for magnetic field **H**, lying in the plane of pyramid base, the contribution of the states with $J_h = \pm\frac{1}{2}$ becomes higher in comparison with **H** $\parallel z$. Therefore, the probability of Zeeman transitions for in-plane magnetic field is higher. This is also true for the hole state with initial admixture of the states with $J_z = \pm\frac{1}{2}$, as for the ground hole state in the considered Ge quantum dot, where the contribution of the states with $J_z = \pm\frac{1}{2}$

is about 16%. The probability of induced transitions between the Zeeman sublevels is determined by the interaction of the magnetic momentum with oscillating microwave magnetic field $H_\perp \cos 2\pi\nu t$ ($H_\perp$ is perpendicular to the external magnetic field $\mathbf{H}$) and is proportional to the square of the matrix element $|\langle\downarrow|\hat{\mu}_\perp H_\perp|\uparrow\rangle|$, where $\mu_\perp$ is the magnetic momentum projection on the direction of microwave field $H_\perp$,[118]

$$P_{\uparrow\downarrow} \sim |\langle\downarrow|\hat{\mu}_\perp H_\perp|\uparrow\rangle|^2$$

For external field $\mathbf{H} \parallel z$ the microwave magnetic field $H_\perp$ lies in the plane of the nanocluster base and the projection of magnetic momentum $\mu_\perp$ is proportional to the principal values of g-tensor: g_{xx} (the direction [110]) and g_{yy} (the direction [$\bar{1}$10]). For microwave field $H_\perp$, which is parallel to the direction [110], the probability is proportional to the square of the principal value g_{xx}: $P_{\uparrow\downarrow} \sim g_{xx}^2$. For external field $\mathbf{H}\perp z$, the projection of magnetic momentum $\mu_\perp$ lies in the plane containing the axis z. For microwave field $H_\perp$, which is parallel to direction [100], the probability is proportional to the principal value g_{zz}: $P_{\uparrow\downarrow} \sim g_{zz}^2$.

For quantum dot with $g_{zz} = 12.28$, $g_{xx} = 0.69$, $g_{yy} = 1.59$, the estimation of induced transitions probability gives the probability for $\mathbf{H} \parallel z$ approximately two orders smaller than for $\mathbf{H}\perp z$:

$$\frac{P_{\uparrow\downarrow}(\mathbf{H}\perp z)}{P_{\uparrow\downarrow}(\mathbf{H} \parallel z)} \approx 100$$

Taking into account the decrease of transverse components ($g_{xx} = 0.6$, $g_{yy} = 0.33$) caused by the Ge/Si mixing at the interface, the ratio amounts to thousand:

$$\frac{P_{\uparrow\downarrow}(\mathbf{H}\perp z)}{P_{\uparrow\downarrow}(\mathbf{H} \parallel z)} \approx 10^3$$

The obtained results give the evidence that the driving force of g-factor size dependence is the change of the contribution of the $|\frac{3}{2}\rangle$-states to the hole state in QD. The existing ratio between contributions of the $|\frac{3}{2}\rangle$-state and the $|\frac{1}{2}\rangle$-state composing the hole state in QD, was explained by simple model of the band structure without interaction of the electronic bands.[106] It was considered separately the energy spectrum of hole with $J_z = \pm\frac{3}{2}$ and the energy spectrum of hole with $J_z = \pm\frac{1}{2}$ in QD (Fig. 16). In frame of this model the deepest energy levels in QD belong to hole with $J_z = \pm\frac{3}{2}$. In the region of the excited states one can find the levels of both $|\frac{3}{2}\rangle$-states and $|\frac{1}{2}\rangle$-states. If the mixing between the $|\frac{3}{2}\rangle$-states and the $|\frac{1}{2}\rangle$-states is included into consideration then the true spectrum of a hole in QD can be obtained. In the region of the excited states there are some "mixed" states with comparable contributions of both holes. The ground state mainly consists of the $|\frac{3}{2}\rangle$-state. This qualitative model is justified by results of numerical expansion of hole states in QD on the $|\frac{3}{2}\rangle$-states and $|\frac{1}{2}\rangle$-states.
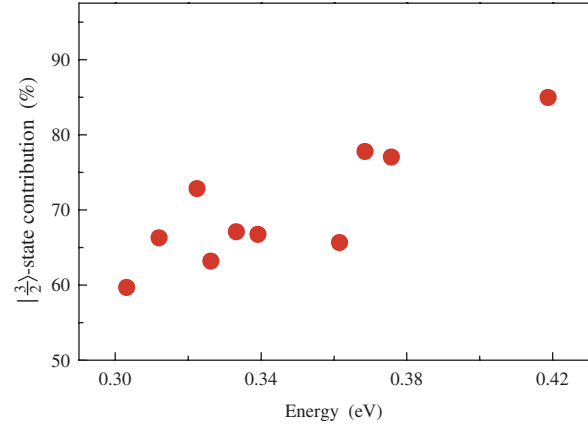
Fig. 17. The $|\frac{3}{2}\rangle$-state contribution for the ground state and nine excited states in Ge quantum dot as a function of the state energy. The energy is counted from the valence band edge in bulk Si, the energy of the ground state $E_0 = 420$ meV.

Figure 17 presents the contributions of the $|\frac{3}{2}\rangle$-states for the ground and excited states of confined hole in the quantum dot with sizes $l = 15$ nm, $h = 1.5$ nm. These results show that the contributions of the $|\frac{3}{2}\rangle$-states are smaller for more excited states than for deeper states. For example, for the first excited state, the $|\frac{3}{2}\rangle$-state contribution goes down until 79%, while for the ground state it is about 84%. For the ninth excited state, the $|\frac{3}{2}\rangle$-state contribution is about 60% of the wave function. The contribution of the $|\frac{3}{2}\rangle$-state in the QD hole states is not described by smooth function of the energy. For explanation of this stepwise change, we construct the wave functions of $|\frac{3}{2}\rangle$-states and $|\frac{1}{2}\rangle$-states separately.

The calculated wave functions of these states for the first four levels in QD are presented in Figure 18. The $J_z = \pm\frac{3}{2}$ part of the ground state has the s-like wave function. Regarding $J_z = \pm\frac{1}{2}$, which is about 16% of the ground state, it has the d-like wave function (Fig. 19). Certainly, the lowest state is the s-like state, followed by the p-like state, then the d-like state, and so on. A degree of the $|\frac{1}{2}\rangle$-state admixture to the $|\frac{3}{2}\rangle$-state is determined by the energy gap between these states and is proportional to $(E_{\pm 3/2} - E_{\pm 1/2})^{-1}$. From the data in Figure 18, one can conclude that the ground state is formed by mixing of the s-like state from the spectrum of hole with $J_z = \pm\frac{3}{2}$ and the d-like state from spectrum of hole with $J_z = \pm\frac{1}{2}$. In this case, the admixture of the $|\frac{1}{2}\rangle$-states is determined by the energy gap $\Delta E_0 = E_{\pm 3/2}^s - E_{\pm 1/2}^d$. The first and the second excited states in QD are formed by mixing of the p-like states from both spectra. At first glance the character of these wave functions is not clear. But the superposition $1/\sqrt{2}(|\psi_1\rangle \pm |\psi_2\rangle \cdot \exp(i\varphi))$ has p-like character (see panels with asterisks in Figure 18) which classifies its parts as p-like wave functions. In these cases, the energy gaps are the same ($\Delta E_1 = \Delta E_2 = E_{\pm 3/2}^p - E_{\pm 1/2}^p$) and the $|\frac{1}{2}\rangle$-state contributions are equal. The third excited state is formed by mixing the d-like state from the spectrum of hole with $J_z = \pm\frac{3}{2}$ and the s-like state from the spectrum of the hole
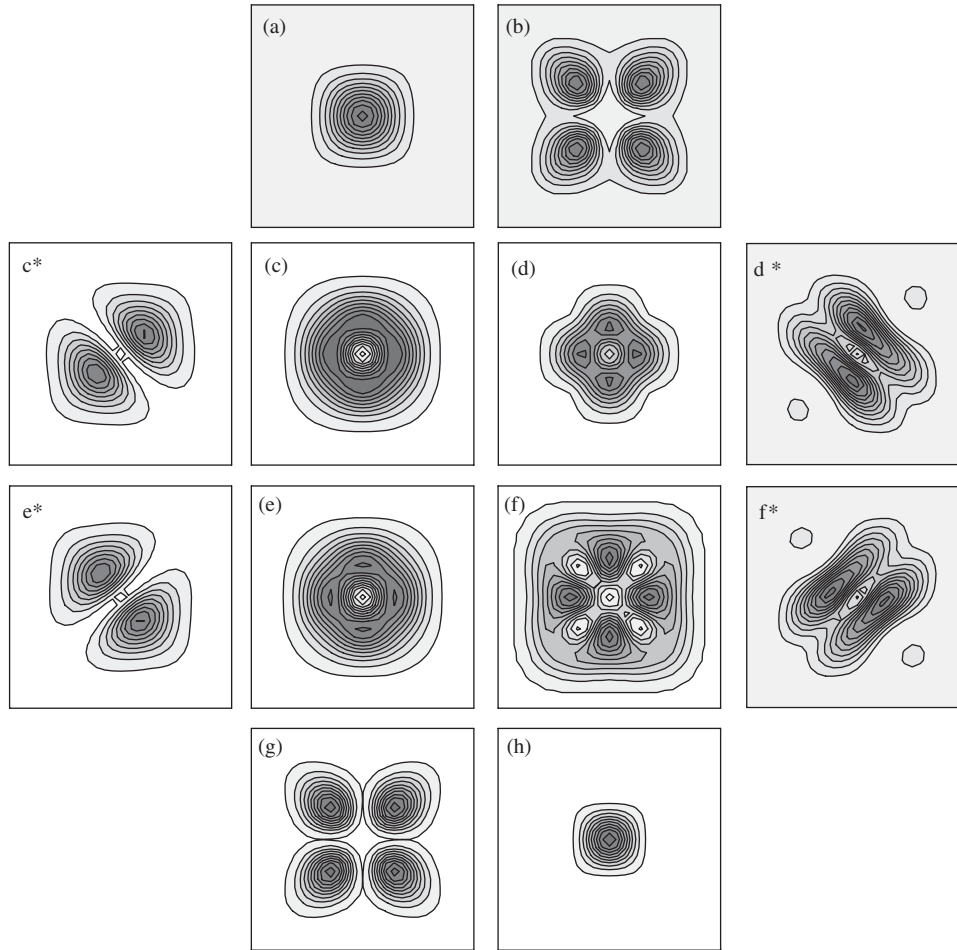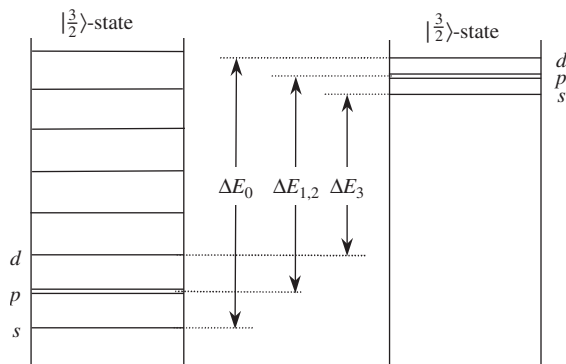
Fig. 18. The wave functions of $|\frac{3}{2}\rangle$-states and $|\frac{1}{2}\rangle$-states for first forth levels in quantum dot: ground state (a), (b); first excited state (c), (d); second excited state (e), (f); third excited state (g), (h). The center right panel presents $|\frac{1}{2}\rangle$-states; the center left panel presents $|\frac{3}{2}\rangle$-states. For clarifying the character of wave functions for first and second excited states, we create the superposition of these wave functions $(1/\sqrt{2})(|\psi_1\rangle \pm |\psi_2\rangle \cdot \exp(i\varphi))$ with any optimal phase φ, which demonstrates *p*-like character ($*$). Panel c^* corresponds to "+", e^* corresponds to "−" in this superposition; both are related to the $|\frac{3}{2}\rangle$-states. Analogously, the d^* and f^* correspond to the $|\frac{1}{2}\rangle$-states.

with $J_z = \pm\frac{1}{2}$. In this case, the $|\frac{1}{2}\rangle$-state admixture is determined by the energy gap $\Delta E_3 = E_{\pm 3/2}^d - E_{\pm 1/2}^s$, the distance between the interacting energy levels is smaller and the $|\frac{1}{2}\rangle$-state admixture is higher than for underlying levels. By this way, one can find the ratio between the energy gaps

Fig. 19. The schematic sketch of energy spectra of $|\frac{3}{2}\rangle$-states and $|\frac{1}{2}\rangle$-states in the model of noninteracting electronic bands.

in all four cases ($\Delta E_0 > \Delta E_1$, $\Delta E_1 = \Delta E_2$, $\Delta E_2 > \Delta E_3$) and explain the degree of the $|\frac{1}{2}\rangle$-state admixture for the first four levels in the quantum dot. For higher levels, the interpretation is more difficult because the wave functions of these states are more complicated, and it is impossible to classify them as *s*-like, *p*-like, *d*-like, ... wave functions. So, the contribution ratio between the $|\frac{3}{2}\rangle$-state and the $|\frac{1}{2}\rangle$-state is determined by the energy gap, which depends on the character of the wave functions of interacting states.

When shape of the pyramid ($h/l = 1/10$) is preserved, the spatial distribution of strains and their magnitude in the quantum dot are not significantly changed by increasing nanocluster sizes. The strain splitting between the light and heavy hole states remains the same in this case. The quantum confinement energy becomes smaller for larger nanoclusters; for example, for nanocluster with sizes $l = 100$ nm, $h = 10$ nm, it is about a few millielectronvolts. Therefore, the ground hole state shifts to the bottom of the potential well. The excited states are not so sensitive to the change of the quantum confinement energy because their

localization lengths are larger than the nanocluster size. The tails of the wave function penetrate into Si surrounding Ge nanocluster. Hence, the shift of the excited states is smaller than for ground state. The energy gap ΔE_0 between the *s*-like state of hole with $J_z = \pm\frac{3}{2}$ and the *d*-like state of hole with $J_z = \pm\frac{1}{2}$ increases. Consequently, the $|\frac{1}{2}\rangle$-state contribution to the hole ground state decreases and the wave function becomes closer to the heavy hole state. In this case, the main reason determining the change of the contribution ratio between the $|\frac{3}{2}\rangle$-state and the $|\frac{1}{2}\rangle$-state is the quantum-confinement factor (the change of the confinement energy).

The obtained results give the evidence that the knowledge of the hole wave function structure is very important for interpretation of magnetic properties. Experimentally the hole *g*-factor is usually obtained from optical measurements. In these experiments, the photoluminescence spectra in magnetic field are studied.[119–121] The hole *g*-factor was derived from experimental value of exciton *g*-factor (g_{ex}) and electron *g*-factor (g_e) using the equation $g_{ex} = g_h \pm g_e$ ("−" for bright excitons, "+" for dark excitons). To avoid the systematic inaccuracy caused by the existing of exchange interaction between the electron and the hole, one must carry out the experiment with "free" hole (not bounded in exciton). It may be the magneto-tunnelling experiment, which is analogous to experiment with an electron.[122] In this case, the choice of the direction of magnetic field plays an important role because the Zeeman splitting and the probability of Zeeman transitions are in strong dependence on the magnetic field direction. For direction $\mathbf{H} \| z$, Zeeman transitions are almost forbidden. But in the case $\mathbf{H} \perp z$, the Zeeman splitting is vanished. Therefore, it would be better to carry out the experiment in the tilted magnetic field when the ground hole state in QD is sufficiently split and Zeeman transitions are allowed.

3.4. Electronic Configuration of Excitons and Excitonic Complexes

Ge/Si(001) QDs exhibit a type-II band lineup. The large (∼0.7 eV) valence band offset in this heterojunction leads to effective localization of holes in the Ge regions, whereas these Ge regions represent potential barriers for electrons. When the hole is captured by the Ge dot, its Coulomb potential results in binding of an electron in the vicinity of the Ge dot. The spatially separated interacting electron and hole are usually referred to as a "spatially indirect exciton." To obtain the binding energy of the excitonic complexes consisting of various numbers of electrons and holes captured on the Ge/Si QD, a mathematical model of the excitonic complex based on the effective-mass approximation was developed.[85, 123, 124] The realistic geometry of the Ge island is included in the model. The length of the pyramid base is assumed to be equal to 15 nm. Because only the ground state of the excitonic complex was considered, the model restricted by consideration of only the

lowest minimum of the conduction band and the highest VB maximum. From the strain distribution[74] and deformation potential values[110] it was found that two Δ valleys, oriented along the growth direction, offer the lowest CB minimum in Si. The heavy hole branch produced the highest VB maximum in the Ge island. The confining potential for electrons and holes consists of the band offset between unstrained Si and Ge and strain-induced modification of conduction and valence bands. The band offset values of 0.34 eV for the Δ minimum of the CB and 0.61 eV for the VB have been used in model. Values of deformation potentials are taken from Ref. [87]. Effective masses of both electrons and holes are taken to be anisotropic, and it is assumed for simplicity that masses are coordinate independent. The effective masses in the growth direction and in the plane orthogonal to it are correspondingly m_z and m_{xy}. The values of longitudinal and transversal effective masses of the Δ minimum in Si were used as following: $m_z = 0.92m_0$ and $m_{xy} = 0.19m_0$ for the CB. In the VB, these values are $m_z = 0.2m_0$ (the heavy hole mass in Ge in the $\langle 001 \rangle$ directions) and $m_{xy} = 0.39m_0$. The value of m_{xy} for the VB is taken so as to make the value of averaged effective mass $m_{av} = (m_{xy})^{2/3}(m_z)^{1/3}$ coincide with the averaged heavy-hole mass in Ge. The interaction between charged particles is taken in the form of the Coulomb potential.

To solve the many-particle problem, the Hartree approximation is used; that is, a separable exciton wavefunction is assumed and the single electron and hole states are determined self-consistently. The set of Schrödinger equations was solved by the finite-difference method using the grid with period of 0.543 nm (the lattice constant of Si) containing $50 \times 50 \times 60$ nodes. To reduce an error that arises from the finite size of the grid, the calculation was performed twice with different boundary conditions applied: once with Dirichlet boundary conditions ($\psi|_{boundary} = 0$) that gives an upper estimate for energy levels and with Neumann boundary conditions ($\partial\psi/\partial n|_{boundary} = 0$) that gives a lower estimate. The arithmetic mean of the two estimates is taken as a final result. According to the Pauli principle, filling each VB level with only two holes and each CB level with only four electrons was permitted. Four electrons can occupy the same CB level because there are two equivalent Δ valleys and two equivalent spin states.

Energies of interband optical transitions corresponding to adding an exciton to the Ge/Si QD was calculated. The energy of transition from the empty dot state to the state with one electron and one hole in the QD was denoted as $E_{0e0h \rightarrow 1e1h}$, and so on. Calculated values are $E_{0e0h \rightarrow 1e1h} = 629.6$ meV, $E_{0e1h \rightarrow 1e2h} = 639.3$ meV, $E_{1e1h \rightarrow 2e2h} = 639.8$ meV. Therefore one excess hole in the dot causes an increase of the excitonic transition energy by 9.7 meV. This blueshift of the excitonic line is a consequence of the spatial separation of electrons and holes, which is a characteristic of type-II QDs. Indeed, neglecting for simplicity the perturbation of electron and hole
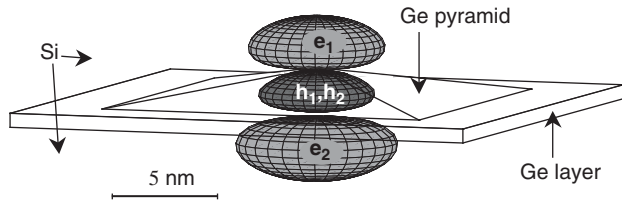
Fig. 20. Wavefunctions of electrons ($e1$, $e2$) and holes ($h1$, $h2$) in the ground state of biexciton. The surface of constant wavefunction equals to 0.5 of its peak value.

wavefunctions by the second hole in the dot, one may get:

$$E_{0e1h \to 1e2h} = E_{0e0h \to 1e1h} + V_{eh} + V_{hh}$$

where V_{eh} and V_{hh} are electron–hole and hole–hole interaction energies. Because the mean distance between electron and hole is larger than between two holes, then $|V_{eh}| < |V_{hh}|$. Therefore $E_{0e1h \to 1e2h} > E_{0e0h \to 1e1h}$.

In the case of an exciton consisting of one electron and one hole, the hole is located in the centre of the pyramidal Ge island, and the electron is confined in the Si vicinity of the island apex.[123, 124] This location of the electron is first, due to, inhomogeneous strain that forms the confining potential for electrons near the apex of the pyramid and, second, the Coulomb attraction to the hole. When a new electron is added to the QD, it is found to be spatially separated from the first one and located under the base of the pyramid symmetrically to the first electron Figure 20. At further filling of the dot, the third electron added to the apex well, the fourth to the base well, and so on. The energy of excitonic transition in the QD already containing an exciton, $E_{1e1h \to 2e2h}$, is larger by 10.2 meV as compared with $E_{0e0h \to 1e1h}$, the excitonic transition energy in the empty QD. This follows because the second electron in the excitonic complex is localized in a shallower potential well than the first one.

The experimental verification of the calculation results will be presented in Section 7.1 on the optical properties.

The electron binding energy (i.e., the energy needed to move an electron to infinity) have been calculated in the excitonic complex containing different numbers of electrons N_e and holes N. Calculations show that for $N_e < 8$ QDs can keep $N + 1$ electrons. For a single layer of Ge islands, a shallow bound electron state exists even when no holes are in the dot ($N = 0$, $N_e = 1$). This is due to nonuniform strain of the silicon matrix. The addition of one electron and one hole to QD gives rise to an increase of binding energy because, in this case ($N = 1$, $N_e = 2$), the extra electron and hole form a dipole which creates an additional attractive potential. When N increases, the binding energy of the $N + 1$th electron increases up to $N = 2$, and then slightly decreases (Fig. 21). For $N = 8$, the ninth electron cannot be captured by the QD because each electronic potential well (above and below the Ge island) has one fourfold degenerate quantum level, and both these levels are fully occupied by eight electrons.
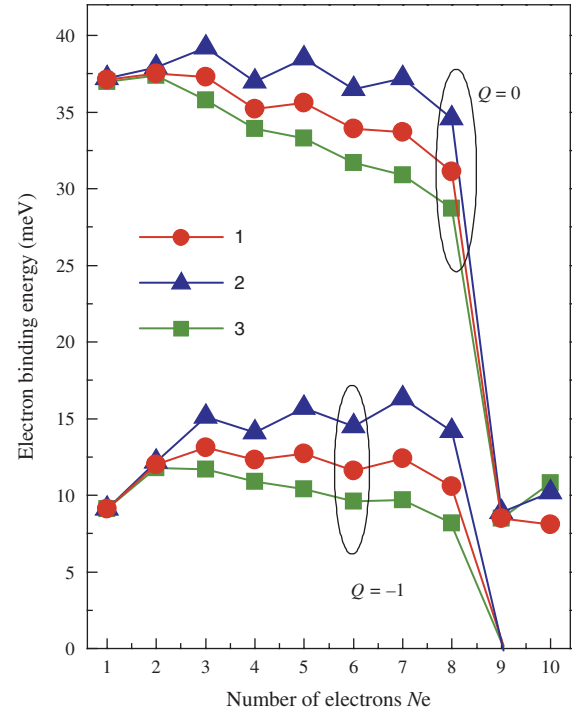

Fig. 21. Binding energy of electron trapped by the Ge/Si QD, as a function of number of electrons N_e in the excitonic complex. Q is the total charge of quantum dot ($N_e + N$). Curve 1 represents the binding energy of exciton or excitonic trion, curve 2 corresponds to the energy of the topmost occupied electron state, curve 3 depicts the energy of the first empty electron state. (The energies for 2 and 3 are counted from the CB edge in bulk Si).

In the case when $N_e = N$ (the upper curve in Fig. 21) potential wells for electrons are deeper than for the case $N_e = N + 1$ (the lower curve); therefore, the dot with nine holes can trap the ninth electron. The dependence of electron binding energy on the number of electrons and holes provides an explanation for the negative photoconductivity observed in the n-type Ge/Si QD structure (see Section 7.3 on the optical properties). QDs serve as traps for free electrons. When electron–hole pairs are photogenerated, nonequilibrum holes, and electrons are captured by QDs. As a result, the depth of traps for electrons (or the electron binding energy) increases with increasing number of electrons and holes (Fig. 21, lower curve) and therefore additional equilibrium electrons are trapped. Thus the concentration of free electrons decreases under illumination, and conductivity falls. The negative photoconductivity is one of the characteristic feature for type-II QDs only.

3.5. Strain Distribution and Electronic States in Multiple Layers of GeSi/Si Quantum Dots

There are two main types of band-edge alignment, namely type-I and type-II, in heterostructures with semiconductor QDs. In type-I QDs, the band gap of the narrow-gap material lies entirely within the gap of the wide-gap semiconductor, and both electron and hole are confined
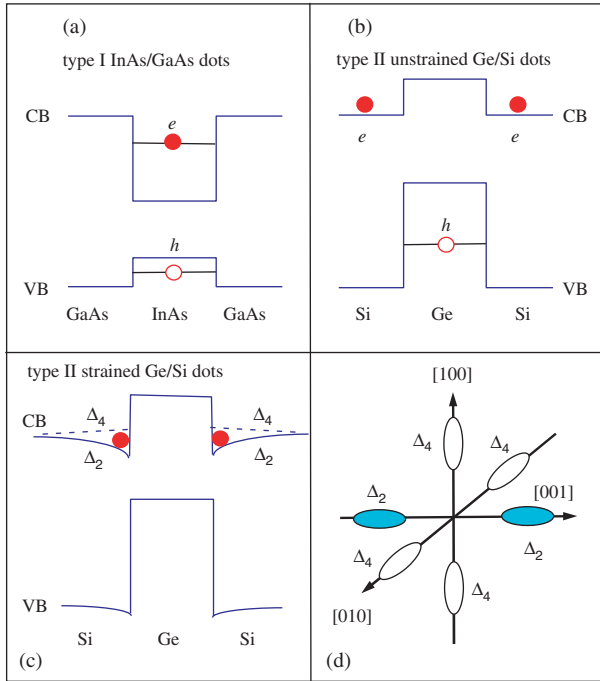
Fig. 22. Schematic overview of the band alignment in (a) type-I and (b) type-II QDs. (c) Band structure in Ge/Si(001) QDs modified by a tensile strain. The conduction band (CB) in Si just above and below the Ge dot splits into Δ_4 and Δ_2 valleys. (d) Fermi surface in the Si conduction band.

inside the same region (Fig. 22(a)). A typical example of type-I band-edge line-up is the InAs QDs in GaAs matrix. For type-II QDs, the localization inside the dot occurs only for one of the charge carriers, whereas the dot forms a potential barrier for the other particle (Fig. 22(b)). A system like this is that of Ge/Si(001) dots formed by strain epitaxy, in which the holes are strongly confined in the Ge region, and the electrons are free in the Si conduction band. The above consideration disregards possible modification of the band structure due to inhomogeneous strain in the dots and the surrounding matrix. Tensile strain in the nearby Si causes splitting of the sixfold-degenerate Δ-valleys ($\Delta 6$) into the fourfold-degenerate in-plane $\Delta 4$-valleys and the twofold-degenerate $\Delta 2$-valleys along the [001] growth direction. The lowest conduction band edge just above and below the Ge island is formed by the $\Delta 2$-valleys yielding the triangle potential well for electrons in Si near the Si/Ge boundary (Fig. 22(c)). Thus one can expect three-dimensional localization of electrons in the strained Si near the Ge dots. The electron binding energy in a strain-induced potential well in a single Ge/Si QD was predicted to be very small (<10 meV). This value is expected to enlarge vastly in multilayer Ge/Si structures with vertical stacking of Ge islands due to accumulation of strain energy from different dot layers in a stack and increase of the potential well depth. In this section we present the results of modeling the strain distribution and electronic states in Ge/Si QDs stacked in a multilayer structure.[125, 126]

The stacked QD structure is modeled by fourfold stacked Ge_cSi_{1-c} QDs aligned along the growth direction z and separated by Si. The first and second Ge islands in a stack as well as the third and fourth Ge dots are separated by 3-nm Si spacers, while the distance between the second and third Ge nanoclusters is 5 nm. Each Ge_cSi_{1-c} QD has a truncated-pyramid shape with base orientation along [100] (x) and [010] (y) directions. The length of the base side was 23 nm, the height is 1.5 nm. Each pyramid lies on a 4.5 ML Ge_cSi_{1-c} wetting layer and contains $(1-c) \times 100\%$ Si atoms randomly distributed within QD. The size of computational cell (GeSi island plus Si environment) is $50a \times 50a \times 50a$ along x, y, and z axes, respectively, where $a = 5.431$ Å is the Si lattice constant. The size of the pyramid base is $28a \times 28a$, the height is $2a$. Calculated strain distribution was then scaled by a factor of 1.5 in all three dimensions to reach realistic sizes of Ge/Si island (base length of ≈ 23 nm and height of ≈ 1.5 nm). The strain distribution was found in terms of atomic positions, using VFF model with a Keating interatomic potential. To obtain strain distribution in a stacked island arrangement, the calculated strain fields of single islands are superimposed and added in real space. This approach overestimates the strain in Si by only 10%.[68] In order to check whether the calculation volume is large enough to give the proper (size-independent) result we performed numerical analysis also for smaller computational cells ($32a \times 32a \times 50a$ and $32a \times 32a \times 32a$) and found that the strain distribution does not depends on the size of supercell to within 5% of accuracy.

It is naturally to expect that the maximum strain is realized in the middle of the stack. The calculated strain components along the z and x directions through the centre of symmetry of a fourfold stack of $Ge_{0.7}Si_{0.3}$ islands is shown in Figure 23. The positive strain values correspond to tensile strain and the negative ones to compressive strain. The tension in the Si above and below GeSi islands is evident. In the lateral direction the strain in Si relaxes from the centre at a scale comparable to the diameter of underlying GeSi island and then changes its sign, demonstrating that the Si is laterally compressed near the edges of GeSi islands. Above the stack, strain goes to zero with z over a length of about $\ell = 15$ nm.

Now let us consider the strain-modified conduction band-edge diagram at the $\Delta 2$ valleys in which the electron localization is expected. The 3D potential energy distribution of electrons in $\Delta 2$ states with respect to the unstrained Si conduction band-edge can be expressed as Ref. [110]

$$V(\mathbf{r}) = \Delta E_c x(\mathbf{r}) + \Xi_d \mathrm{Tr}[\epsilon(\mathbf{r})] + \Xi_u \epsilon_{zz}(\mathbf{r}) \qquad (18)$$

where ΔE_c is conduction band offset between unstrained Si and GeSi, $x(\mathbf{r}) = 1$ on conditions that the vector $\mathbf{r}$ points to the atom inside GeSi island, otherwise $x(\mathbf{r}) = 0$; Ξ_d and Ξ_u are the deformation potentials. The quantity $(\Xi_d + \frac{1}{3}\Xi_u)$ corresponds to a_c, the hydrostatic deformation
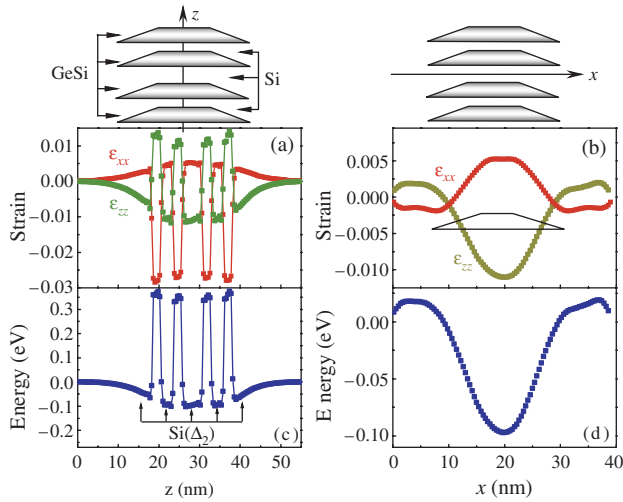
Fig. 23. Strain tensor components ϵ_{zz} and ϵ_{xx} ($\epsilon_{yy} = \epsilon_{xx}$) for a four-fold $Ge_{0.7}Si_{0.3}$ island stack (shown on top panels) along (a) the z-axis and (b) the x-axis. In a latter case the strain profiles are plotted for the central Si separation layer above the tip of GeSi island. (c) and (d) The strain-modified confinement potential for electrons with respect to the conduction band-edge of unstrained Si along the same directions.

potential for the condcution band. $\mathrm{Tr}[\epsilon(\mathbf{r})]$ is equal to $\epsilon_{xx} + \epsilon_{yy} + \epsilon_{zz}$ which is hydrostatic component of the strain. Values of deformation potentials a_c and Ξ_u are taken from Ref. [110]. The conduction band offset between unstrained Si and $Ge_{0.7}Si_{0.3}$ is about 0.29 eV.[126] The final conduction band-edge alignment along the z and x directions through the centre of symmetry of a fourfold stack of $Ge_{0.7}Si_{0.3}$ islands is shown in Figure 23. One can see that potential well for electrons is more shallow in the layer plane ($\sim$100 meV) and just its depth determines the electron binding energy.

The electron bound states are found by numerical solving the 3D Schrödinger equation using the effective-mass approximation:

$$\left(\frac{\hat{p}_x^2 + \hat{p}_y^2}{2m_{xy}} + \frac{\hat{p}_z^2}{2m_z} \right)\psi + V\psi = E\psi \qquad (19)$$

where $V = V(\mathbf{r})$ is defined by Eq. (18). We took the values of longitudinal and transversal effective masses at the Δ minimum in Si as m_z and m_{xy}, correspondingly; so $m_z = 0.92m_0$ and $m_{xy} = 0.19m_0$. The size of computational cell is $62 \times 62 \times 120$ along x, y, and z axes, respectively, in unit of three-fourths the lattice constant of bulk Si, i.e., $25.2 \times 25.2 \times 48.9$ nm^3. To calculate the energy levels and electron wave functions we employ the free-relaxation method (see, Section 3.2).

In Figure 24 we show the isosurface plots of the charge density $|\psi_i(\mathbf{r})|^2$ for the first 6 electronic states. The values of the electron binding energies E_i ($i = 1, \ldots, 6$) for the same states are shown in Figure 25 for different Ge contents in the dots. The isosurface level is selected as $1/e$ ($e = 2,71828\ldots$) of the maximum wave-function amplitude $|\psi_{\max}(\mathbf{r})|$. The lowest three electron states are an
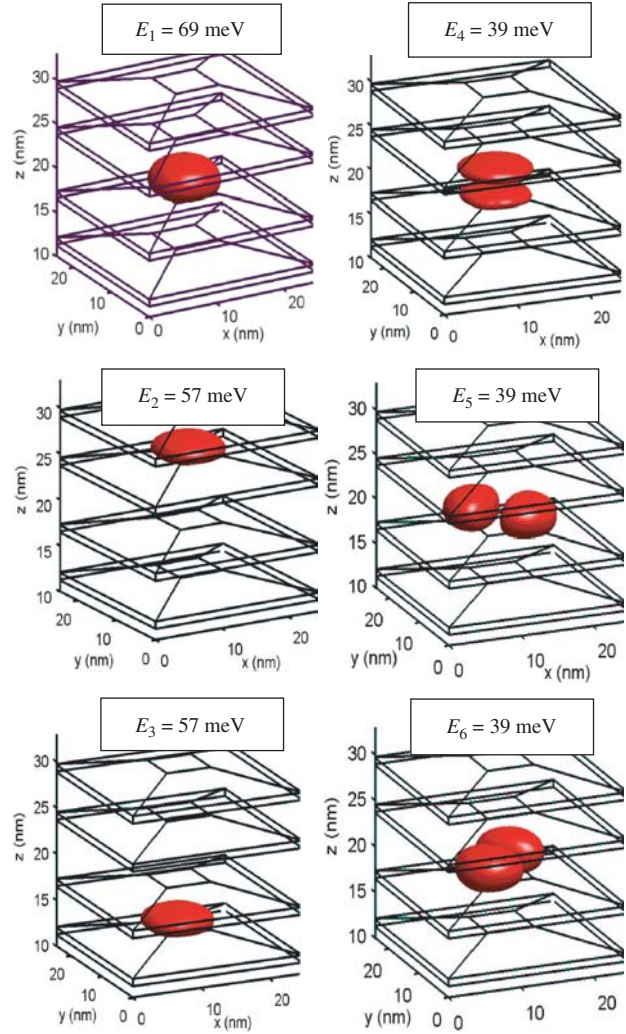
Fig. 24. Three-dimensional view of the isosurface of the electron charge density for the six lowest conduction states. The isosurface level is selected as $1/e$ ($e = 2,71828\ldots$) of the maximum wave-function amplitude $|\psi_{\max}(\mathbf{r})|$. The probability of finding the electron inside is 70–77% dependent on the state. E_i is the single-electron binding energy of the i-th state, determined with the error of ±1 meV. The pyramid base size is 23×23 nm^2, the Ge content in the island $c = 0.8$.
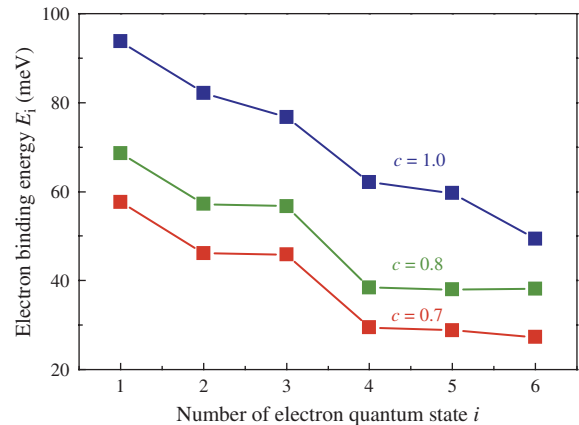

Fig. 25. Electron binding energy E_i for the first six bound states at different composition c of Ge in nanoclusters.

s-like state located in different Si spacers, while the next three are *p*-like states localized along [001], [110], and [$\bar{1}$10], respectively. As expected, the electron ground state is really confined in the middle of the stack. The electron wave functions are strongly localized near the tip of GeSi islands.

4. SINGLE-ELECTRON PHENOMENA

4.1. Single-Electron Tunneling

For the first time, conductance tunneling spectroscopy has been applied to study single-electron effects in arrays of self-assembled quantum dots in Refs. [127, 128]. The vertical structures composed of a layer of Ge quantum dots separated from two parallel circular electrodes (boron doped p^+-$Ge_{0.3}Si_{0.7}$ layers) by thin Si tunnel barriers. The mean dot in-plane diameter was 15 nm. The differential transversal conductance as a function of applied voltage is shown in Figure 26. The upper part of the figure corresponds to symmetric silicon barriers (both Si layers consist of a 9 nm thickness). On the bottom of the figure, we display conductance spectrum for the sample in which the tunneling barriers are different in thickness
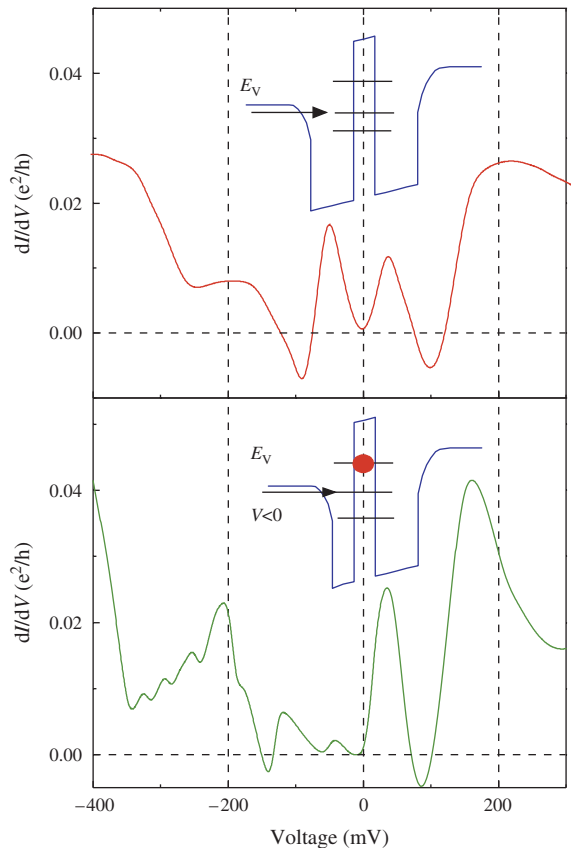
Fig. 26. Transversal differential conductance versus bias voltage for samples with different Si barrier thickness. The upper panel corresponds to symmetric Si barriers of a 9 nm thickness. On the bottom of the figure we display conductance characteristic for the sample, in which the Si tunneling barriers are different in thickness (9 nm and 6 nm, respectively).

(9 nm and 6 nm, respectively). The positive-bias direction is defined as that with holes moving from the top contact to the substrate passing first through the thick barrier and then through the thin one. In both cases, the well-pronounced conductance oscillations were observed at $T = 4$ K, implying the existence of a sharply defined discrete hole spectrum in the Ge islands. Note that the negative differential resistance (NDR) region appears to be around zero bias. The effect of NDR is a typical feature for resonant tunnelling of carriers into bound states in double-barrier structures.

A sample with symmetric barriers exhibits oscillations, which are periodic in voltage, of period 150 mV. This allows us to estimate the level spacing in the islands to be $150/2 = 75$ meV. In the asymmetric structure, the conductance peaks at negative bias are split into oscillations with a smaller period. An accumulation of holes is expected at resonance when holes are injected through the thinner emitter and are inhibited from tunnelling out due to the lower transition coefficient of the thicker collector. In this case, interaction effects should be important. An extra hole has to overcome the electrostatic repulsion of all charge already on the dot, thereby lifting degeneracy of the single-particle levels. For the other bias polarity, no charging will occur because an injected hole will leave the dot through the other side sooner than the next hole enters. A similar effect, usually observed in tunnel junction containing metallic droplets, is referred to as the "Coulomb staircase." From the conductance peak spacing, we find the charging (correlation) energy 36 meV for the ground state and 18 meV for the first excited state.

4.2. Single-Electron Charging

The capacitance tunneling spectroscopy of quantum dots is based on the fact that the charge in zero-dimensional systems can be changed only by a discrete amount $\delta Q = eN_{QD}$, where e is the electron charge and N_{QD} is the number of quantum dots in the sample.[129]

The external voltage V_g on the control electrode which biases the potential in the quantum dots with respect to the Fermi level in the contact and which is separated from the island layer by a tunneling-transparent barrier, stimulates either capture of carriers from the contact to dot energy levels or the emptying of these levels, depending on the polarity of V_g. When the Fermi level in the contact coincides with the energy of the bound state in a dot, the differential capacitance $C(V_g) = dQ/dV_g$ should exhibit a peak, attesting to the presence of a discrete energy level. The total capacitance of the structure is a sum of two contributions: The first contribution is due to the presence of a space charge region in the carrier-depleted silicon layer, while the second contribution is due to charging of the quantum dots.

In the Schottky diodes with Ge quantum dots, we varied the equivalent Ge thickness d_{eff}.[130, 131] The heterostructures
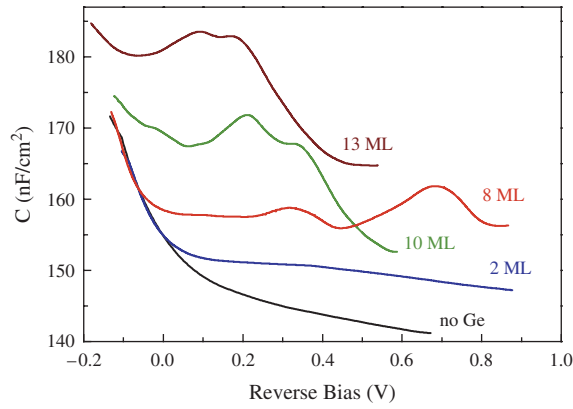
Fig. 27. Capacitance–voltage characteristics for Ge/Si samples with different equivalent thicknesses of Ge layer.

employed in our experiments consisted of the following sequence of layers, starting with the substrate:

(1) A p^+ silicon substrate with (100) orientation and hole density $p = 10^{19}$ cm^{-3}.

(2) A $Si_{0.8}Ge_{0.2}$ layer of thickness $L = 10$ nm, ensuring a sharp heterointerface of the subsequent Si tunnel barrier.

(3) A tunnel Si barrier, $p = 7 \times 10^{16}$ cm^{-3}, $L = 7$ nm.

(4) A layer of Ge SAQDs.

(5) A Si blocking layer, $p = 7 \times 10^{16}$ cm^{-3}, $L = 50$ nm.

(6) An Al control electrode, forming a Schottky barrier on the silicon surface; the area of the Al electrode was equal to 8×10^{-3} cm^2, and a cylindrical mesostructure of this size was etched out to a depth of the order of 5 μm.

The capacitance–voltage characteristic for the sample without a Ge layer is featureless and has the form of standard curve of a p-Si Schottky barrier (Fig. 27). In the case $d_{eff} = 2$ ML, a plateau characteristic for a two-dimensional carrier gas appears in the voltage range $V_g = 0.1$–0.3 V. In the range of equivalent Ge thickness $8 \leq d_{eff} \leq 13$ ML, two peaks appear on the C–V curves at positive polarity. The splitting between these peaks and their width and position on the voltage (energy) scale depend on d_{eff}: as d_{eff} increases, the peaks become narrower and the energy gap between them decreases. The energy gap ΔE between the states that correspond to the capacitance peaks can be found from capacitance data using $\Delta E = e\Delta V_g b/L_T$, where ΔV_g is the voltage splitting between peaks, b is the distance from the dot layer to the substrate, L_T is the total thickness of the epitaxial structure. The calculations yield $\Delta E = 87$ meV for the 8 ML sample (dot lateral dimension $l = 10$ nm), 36 meV for $d_{eff} = 10$ ML ($l = 15$ nm), and 32 meV for the 13 ML sample ($l = 25$ nm). The value $\Delta E = 36$ meV for the structure with 10 ML Ge coverage is in a reasonable agreement with the charging energy in the ground state $E_C = 36$ meV obtained previously in the tunneling spectroscopy experiments (Section 4.1). This makes it possible to interpret the two capacitance peaks as a hole ground state splitting by the electron–electron interaction.

The appearance of capacitance oscillations has been attributed to the formation of an array of Ge nanoclusters[130, 131] whose sizes are quite uniform and, hence, the density of hole states in the array is a δ-like function of energy. The area under each capacitance peak divided by the electron charge turns out to be equal to the areal density of the islands [$(3–4) \times 10^{11}$ cm^{-2}]. This means that

(i) all the Ge dots are involved into the charging process and

(ii) the level degeneracy is lifted by the interaction indeed.

Further confirmation of the Coulombic origin of the splitting has been revealed by capacitance spectroscopy of samples containing two layers of the Ge islands in close proximity.[130] We have observed that in the double-layer structures the peak splitting increases due to Coulomb interaction between the dots in successive layers.

4.3. Tunneling Currents in Schottky Diodes

A schematic representation of a structure used for investigation of the tunneling currents in Ge/Si Schottky diodes with Ge SAQDs is shown in Figure 28. The samples were made in the variant of Schottky diodes with a short base in order to decrease the barrier height at the metal-semiconductor contact through the Schottky effect and, hence, to observe experimentally the change in the effective barrier height due to the electrostatic charging of QDs.[132]
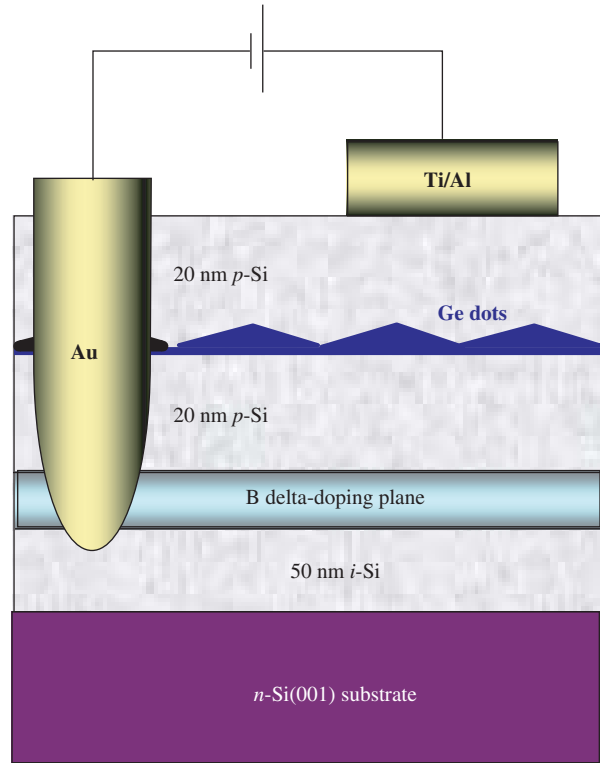
Fig. 28. Schematic representation of a cross-section of a silicon Schottky diode with Ge quantum dots.
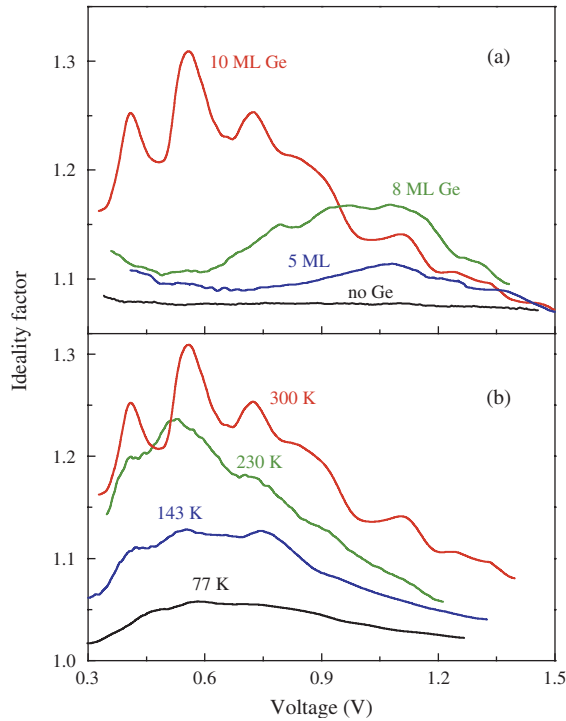
Fig. 29. Dependence of the ideality factor on the reverse bias. (a) Curves for various Ge coverage d_{eff} at $T = 300$ K. (b) Curves for various temperatures for a sample with $d_{eff} = 10$ ML.

The current–voltage characteristics of the metal-semiconductor junction are often written in the form $I = I_s[\exp(eV/nk_BT) - 1]$, where I_s is the diode saturation current, n is the ideality factor. At a low doping level and relatively high temperatures, n is close to unity. The deviation of n from unity in Schottky diodes is mainly associated with the appearance of the tunneling current component; therefore, an analysis of n provides information on tunneling processes in structures with SAQDs.[133]

The ideality factor for reverse bias is determined by the equation[134]

$$n(V) = \frac{e}{k_B T} \frac{\partial V}{\partial \ln\left[\frac{I\exp(eV/k_B T)}{\exp(eV/k_B T) - 1}\right]} \quad (20)$$

Figure 29 displays experimental curves of n versus the reverse bias for samples with various amount of Ge deposited d_{eff}. As d_{eff} increases, the ideality factor grows, and peaks appear in $n(V)$ curves at $d_{eff} \geq 5$ ML, which points to a resonance character of the tunneling current. Resonance tunneling processes are a characteristics feature of the charge transport in double-barrier structures of reduced dimensionality and are due to the quantization of the energy spectrum of electrons, or holes, in the region confined between the barriers. As the reverse bias increases, the energy levels of holes in the QD layer, in turn, reach a resonance with the quasi-Fermi level in the metal. In this case, the probability of tunneling through the Schottky barrier and, hence, the ideality factor must increase, which is actually observed in experiments.[132]

A peak in $n(V)$ at voltages $V \approx 1.1$ V is observed for all samples containing a Ge layer; therefore, it can be associated with the penetration of holes through the energy level of a two-dimensional state in the wetting Ge layer, because this layer is the same in all samples. The peaks at lower voltages in samples with $d_{eff} = 8$ and 10 ML are due to the tunneling of holes through discrete levels in QDs lying above the energy level in the wetting Ge layer. The period of oscillations in curves $n(V)$ is reproduced sufficiently well at various temperatures (Fig. 29(b)). The average period at $d_{eff} = 10$ ML is $\Delta V = 160$ mV. Assuming that the QD layer is introduced exactly in the middle of the diode base and neglecting the bend bending due to the potential of the ionized impurities in the diode base, one can estimate the energy gap between the hole levels in Ge SAQDs as $\Delta E \approx e\Delta V/2 = 80$ meV. This value is in a reasonable agreement with the value of the quantization energy in the same Ge QDs determined by resonant tunneling in p^+–i–p^+ structures (see, Section 4.1).

The experiments described above demonstrate that the phenomenon of oscillations of the ideality factor in the case of a reverse bias in Schottky diodes with SAQDs may serve as a basis for the development of a new method of electron spectroscopy of energy levels in systems with reduced dimensionality.

5. HOLE AND ELECTRON ENERGY LEVELS PROBED WITH ADMITTANCE SPECTROSCOPY

5.1. Energies of Hole Ground States

Admittance spectroscopy is a well-known method to characterize deep impurity levels in semiconductors.[135] In these experiments, the ac conductance G of a pn junction or Schottky diode with the electronic states of interest is measured as a function of temperature for a fixed reverse bias U_b and test frequency $\omega = 2\pi f$. In the case of a deep trap the correlation between thermal emission rates and the binding energy can be easily worked out from the detailed balance between thermal emission and thermal capture rates of charge carriers. For a QD system the mechanism of ac response is suggested to be similar to those commonly considered for defect states.[136–138] An analysis of the QD ac response based on the Shockley-Read-Hall dynamics was made by Chang et al.[139] The small ac voltage with a frequency ω will alternatively fill and empty the QD carrier levels located in the space-charge region. The thermionic emission rate of holes from the dots as well as from deep impurities depends exponentially on temperature T,[140] i.e.,

$$e_p(T) = B\sigma_p T^2 \exp(-E_a/k_B T) \quad (21)$$

where $B = 16\pi m^* k_B^2 / g_t h^3$ is a temperature independent factor, m^* is the effective mass of the density of states, h is the Plank's constant, σ_p is the capture cross section,

E_a is the activation energy being determined by the actual path whereby holes escape from the dots to the Si valence band. Following this approach, the QD ac conductance is given[139]

$$G(\omega, T) = Sq^2 A n_{QD} N_q \frac{\partial \phi_{QD}}{\partial U_b} \frac{f(1-f)}{k_B T} \left(\frac{\omega^2 \tau}{1 + \omega^2 \tau^2} \right) \quad (22)$$

where N_q is the number of quantum hole states in the dot, and $\tau = (1-f)/e_p$ is the characteristic time for the hole exchange between the QDs and the barrier. The function $f(1-f)$ exhibits a peak when $f = 1/2$. Then, for a given measurement frequency, the conductance G reaches a maximum at a temperature T_{max} which corresponds to the condition[139]

$$\omega = \frac{1}{\tau} \approx 2e_p(T_{max}) \quad (23)$$

By measuring the $G(T)$ dependencies at various ω, the activation energies of hole emission rate can be deduced from the Arrhenius plot of $e_p(T_{max})/T_{max}^2$ versus $1/T_{max}$. With changing of the reverse bias U_b, the chemical potential scans through the density of hole states in the QD layer. At higher reverse bias, the chemical potential crosses deeper states in the dots. Thus, from the temperature- and frequency-dependent measurements at different U_b the energy of hole emission from different confined states can be determined.

In this section, we discuss the experiments in which the admittance spectroscopy has been used to study the energy levels of both electrons and holes confined in Ge/Si SAQDs.

First we describe experiments with p-type structures. In Figure 30 we display the capacitance–voltage (C–V) and conductance–voltage (G–V) characteristics for Al/p-Si Schottky diodes with embedded layers of Ge nanoclusters. The area of the Al contacts was $A = 4.3 \times 10^{-3}$ cm^2. Samples were grown by molecular-beam epitaxy on a p^+-Si(001) substrate with a resistivity of 0.005 Ω cm doped with boron up to a concentration of $\sim 10^{19}$ cm^{-3}. A Ge layer about 6 ML thick was introduced into the 0.7-μm epitaxial p-Si layer (boron concentration is $\sim 3 \times 10^{16}$ cm^{-3}) at a distance of 0.4 μm from the substrate. Here we varied the Ge deposition rate from $R = 0.02$ ML/s to $R = 2$ ML/s while maintaining the substrate temperature (500 °C) and Ge coverage being the same for all samples. The structural properties of similar samples were discussed in Section 2.6. For all devices, we observe a plateaulike structure caused by an additional capacitance due to positive charge trapped in the dot layer. Figure 31(a) shows the temperature evolution of the C–V and G–V characteristics of the device with the Ge layer grown at $R = 2$ ML/s for a test frequency of $f = 10$ kHz. Similar graphs were also obtained for the other p-type QD samples. At high temperature, there is a well-pronounced capacitance plateau from 0.2 to 4 V associated with the positive charge accumulation in the dot layer.[141] The width of a plateau depends
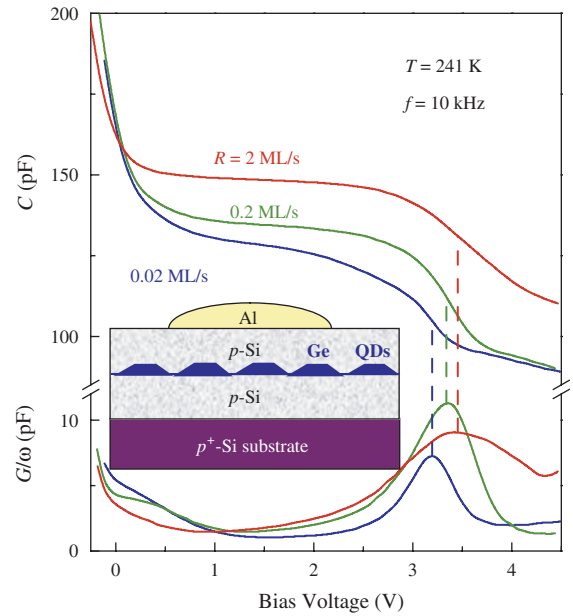
Fig. 30. Capacitance–voltage and conductance–voltage characteristics measured at modulation frequency of 10 kHz and temperature of 241 K for samples with the Ge QD layer grown at 500° and at different deposition rates R (see Fig. 6). Inset: Schematic representation of a cross-section of a p-type Si Schottky diode with a layer of Ge QDs.

on the steady-state occupation of hole levels in the dots. Due to the p-type doping in the Si matrix, the Ge QDs are charged by holes at a zero bias. When a reverse bias is applied to the diode, the holes are gradually swept from the shallower QD states to the deeper states. At $U_b \gtrsim 4$ V, all holes escape from the QDs and the QD contribution to the measured capacitance disappears.

The corresponding step in the capacitance is accompanied by the peak in the measured parallel conductance near the edge of the capacitance plateau. The emergence of a conductance peak can be regarded as a fingerprint of a resonant condition for charging/discharging the QDs,
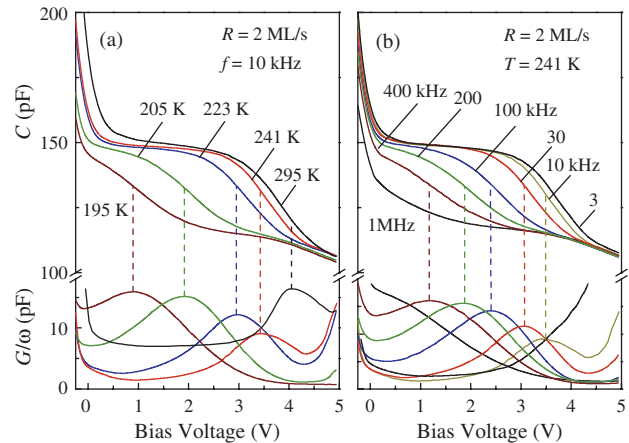
Fig. 31. (a) Temperature dependence of the capacitance–voltage and conductance–voltage characteristics measured at $f = 10$ kHz. (b) C–V and G–V characteristics measured at $T = 241$ K for various frequencies. The layer of Ge QDs was deposited at $R = 2$ ML/s.

which is $\omega\tau = 1$. The characteristic time τ for hole exchange between the dots and the barrier depends on both the QD confined energies and the temperature. At low temperatures, holes freeze onto deep states in the dots and do not participate in the ac response. Therefore, as the temperature is reduced, the capacitance plateau is suppressed and the conductance peak shifts towards lower biases, at which the applied ac frequency resonates with emission rate from shallower QD states. Similarly, the resonant condition should be fulfilled at a lower bias for a higher frequency. Figure 31(b) shows the C–V and G–V traces recorded at $T = 241$ K for different test frequencies. A clear shift of the capacitance step and the conductance maximum towards lower biases is seen as the frequency is increased. This is consistent with the arguments outlined above.

The temperature dependencies for both the capacitance and the normalized conductance measured at different modulation frequencies and bias voltages are displayed in Figure 32. The behavior of $C(T)$ and $G(T)/\omega$ can be qualitatively explained as follows. At a fixed bias, the charging/discharging process corresponds to the QD hole level coinciding with the Fermi level in undepleted part of the p-Si buffer layer. The rate of hole emission from this level becomes more slow when the temperature is reduced; therefore, with a decrease in the modulation frequency, the condition for the capacitance step and the conductance maximum (23) is satisfied at lower temperatures (Fig. 32(a)). With an increase in reverse bias, the holes localized at deeper QD levels, for which condition (23) at a fixed frequency is satisfied at higher temperatures, contribute to the admittance signal. For this reason, the capacitance step and the conductance peak in Figure 32(b) shift towards higher temperatures with increasing U_b.
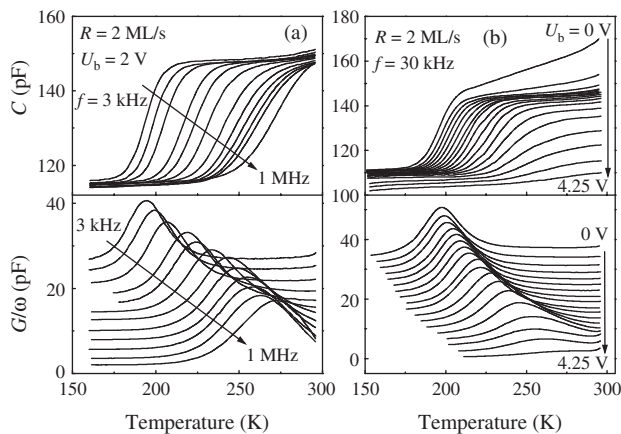
Fig. 32. (a) Temperature dependence of the capacitance C and the normalized conductance G/ω recorded at $U_b = 2$ V and modulation frequencies 3, 5, 10, 30, 50, 100, 200, 300, 400, 500, 600, and 1000 kHz. (b) Temperature dependence of the capacitance and conductance measured at modulation frequency $f = 30$ kHz under different bias voltages. The reverse bias are increased from $U_b = 0$ V to 4.25 V with an increment of 0.25 V. Each conductance curve has been offset by 2 pF for clarity.
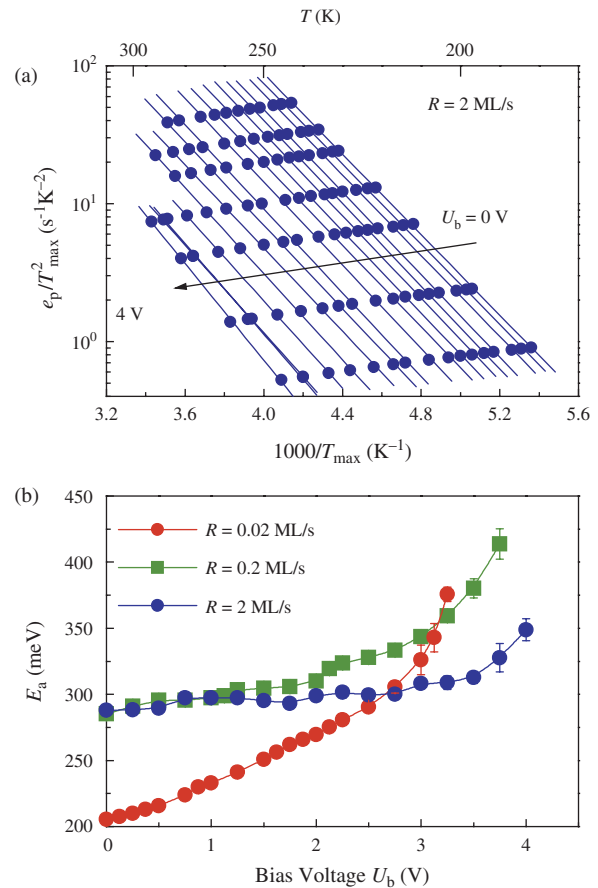
Fig. 33. (a) The Arrhenius plots of the hole emission rate obtained from G/ω-T traces with different bias voltages. The reverse bias are increased from $U_b = 0$ V to 4 V with an increment of 0.25 V. (b) Bias dependent activation energies of hole emission rate for samples with the Ge QD layer grown at different deposition rates R.

At $U_b > 4$ V, Ge QDs become completely depleted and the maximum on the $G(T)/\omega$ curves disappears. This is consistent with the observation from the C–V measurements of the same sample.

Figure 33(a) shows the typical dependencies $e_p/T_{max}^2(T_{max}^{-1})$ obtained using Eq. (23) from the temperature variation under different modulation frequencies. The activation energies E_a of the hole emission rate were found from the slope of the approximating straight lines. The linear correlation coefficients of all the lines are larger than 0.9995. The resulting values E_a for three QD samples are shown in Figure 33(b) as a function of reverse bias voltage. Note that the energies E_a are quite close to the ground-state hole energy levels calculated for such GeSi QDs (see, Fig. 13). For all samples, the activation energy decreases with decreasing of the bias voltage. With increasing of the reverse bias, the chemical potential scans through the density of hole states in the QD layer. At higher reverse bias, the chemical potential crosses deeper states in the dots. In QDs, which can be charged by more than two carriers and in which conclusively higher energy levels than the ground state are occupied, the dependence of the activation energy

on the QD occupation is usually attributed to the state-filling effect.[138, 142] However, the effect of state-filling is not relevant in a system of small QDs which are studied in this paper and contain no more than two holes. Thus, the change of the activation energy with bias may be attributed to the dispersion of the hole ground state eigen energy due to the size distribution of the quantum dots.

5.2. Localization of Electrons in Multiply Layers of GeSi/Si Quantum Dots

Admittance spectroscopy was also employed to obtain the experimental evidence for the electron localization in the strain-modified Si conduction band of a stack of four layers of GeSi QDs embedded in an *n*-type Si(001) matrix.[126] This phenomenon was analyzed theoretically in Section 3.5.

For the experiments, GeSi/Si heterostructures with GeSi islands were fabricated on a n^+-Si(001) substrate with a resistivity of 0.01 Ω cm doped with antimony up to a concentration of $\sim 10^{19}$ cm^{-3}. A fourfold stack of GeSi islands was inserted into the 0.8-μm epitaxial *n*-Si layer at a distance of 0.5 μm from the substrate. The amount of deposited Ge was gradually reduced from 6 ML in the first layer to about 4 ML in the fourth layer to ensure defect-free island formation with equal island sizes and densities in all layers.[143, 144] The *n*-type remote doping was achieved by insertion of a Sb δ-doping Si layer 0.2 μm below the GeSi QD layer. The first and second Ge layers in the stack as well as the third and fourth Ge layers are separated by 3 nm Si spacers, while the distance between the second and third Ge layers is 5 nm (the same structure was modeled theoretically in Section 3.5). As it has been demonstrated in Ref. [126], Ge nanoclusters fabricated by such a way demonstrate good vertical correlation. From cross-sectional transmission electron micrographs, we observe the GeSi dots to be approximately 20 nm in lateral size and about 2 nm in height. The scanning tunneling microscopy of a sample without the Si cap layer showed that the Ge islands have a shape of hut clusters. The density of the dots is about 10^{11} cm^{-2}. The average Ge content of 80% in the islands was determined from Raman measurements. To separate response from the stacked GeSi/Si islands, the reference sample was fabricated under conditions similar to the multilayer sample, except that only a single layer of GeSi QDs was grown. For the capacitance and conductance measurements, Pd Schottky gates with the area of 7.5×10^{-3} cm^2 were deposited on top of the samples through a shadow mask.

Figure 34 shows experimental *C–V* characteristics for the reference and the multilayer samples. The dependence of the capacitance on voltage for the single-layer sample has the form of the conventional *C–V* characteristic of an *n*-type Schottky diode. For the multilayer sample, we observe a steplike structure, which we associate with the negative charge accumulation in the Si layers between the
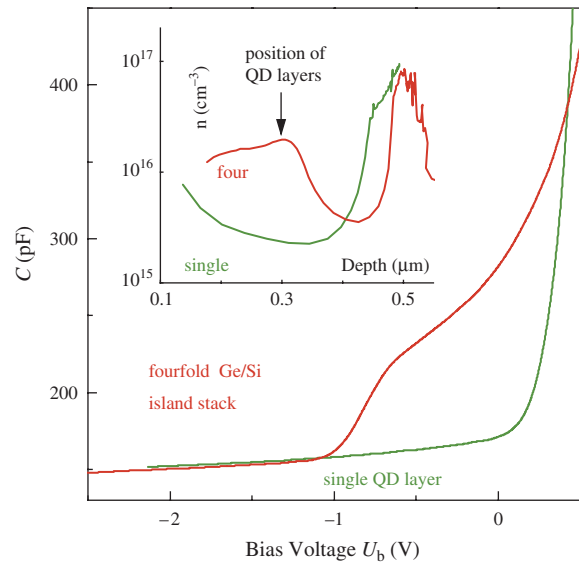

Fig. 34. Capacitance–voltage characteristics measured at modulation frequency of 10 kHz and at $T = 77$ K for the single-layer and multilayer samples with an *n*-type doping. The inset displays the apparent electron distribution derived from the measured *C–V* curves using the full depletion approximation.

stacked Ge islands (see, inset of Fig. 34). The QD contribution to the capacitance disappears at temperatures below ~ 50 K (Fig. 35) due to "freezing" the electrons in the $\Delta 2$ bound states in the strained Si. The corresponding step on the temperature dependence of capacitance is accompanied by the conductance maximum (peak *C* in Fig. 35) which is not seen for the reference sample. Thus we may attribute the conductance peak *C* to the ac response of electrons confined in GeSi/Si islands stacked in a multilayer structure. With increasing reverse bias, the position of peak *C* shifts towards higher temperatures, its amplitude gradually decreases (Fig. 36) and the peak disappears
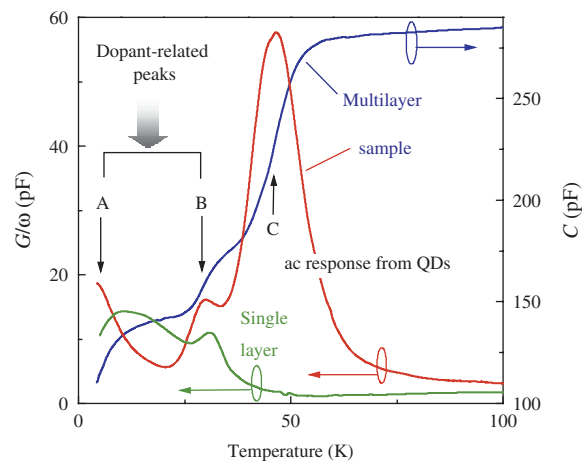
Fig. 35. Temperature dependence of conductance and capacitance measured at bias voltage $U_b = 0$ V and modulation frequency of 1 MHz for the single-layer sample (green line; only conductance is shown) and for fourfold GeSi/Si island stack (red and blue lines).
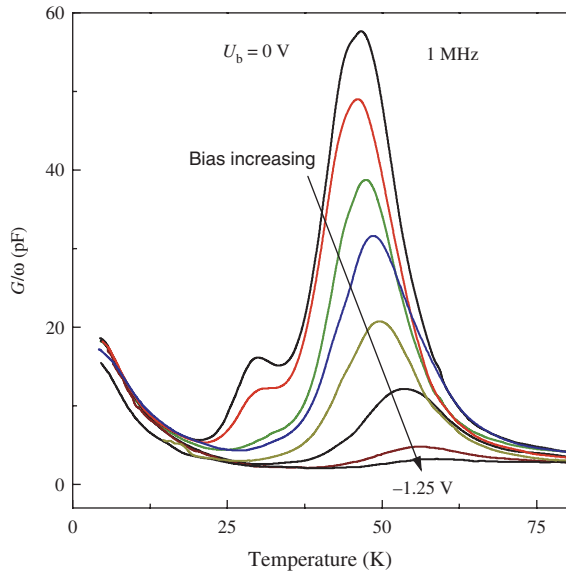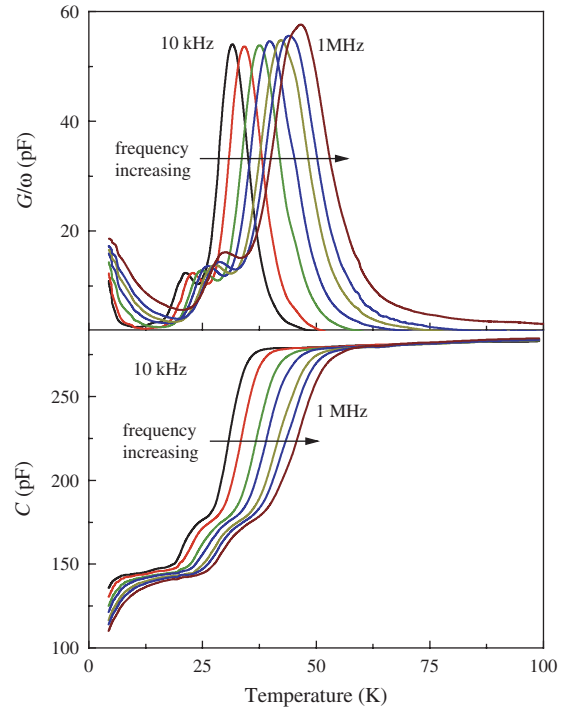
Fig. 36. Conductance spectra of the multilayer sample at the frequency of 1 MHz under different bias voltages. The voltages are 0 V, −0.2 V, −0.5 V, −0.7 V, −0.9 V, −1.0 V, −1.2 V, and −1.25 V from top to bottom.

at voltages $|U_b| > 1$ V just after the ending of the QD-related capacitance plateau in $C–V$ characteristic. Peaks A and B are observed in both samples. They are assigned to a dopant-related admittance signal associated with the carrier freeze-out effect in the highly doped δ-doping Si layer (peak A) and in Si layers with a lower doping Sb concentration (peak B).[145, 126]

Typical conductance spectra measured at different frequencies are shown in Figure 37. Admittance signal originated from electron traps can be used to extract the electron binding energy. For a given measurement frequency $\omega = 2\pi f$, the conductance reaches a maximum at a temperature T_{max} which corresponds to the condition $e_n(T_{max}) \approx \omega/2$, where $e_n = e_0 \exp(-E_a/kT)$ is the emission rate of electrons from the bound to extended states which depends on the electron binding energy E_a. Just as in Ref. [136], we assume the preexponential factor e_0 to be temperature independent because it is not *a priori* clear how the e_0 depends on temperature for shallow levels in QDs. Arrhenius plots necessary for deriving the activation energy are depicted in inset of Figure 38. The activation energies of the electron emission rate were found from the slope of the approximating straight lines. The resulting values of E_a are shown in Figure 38 as a function of reverse bias voltage. The theoretical values of electron binding energies E_i found in Section 3.5 are shown in Figure 38 by arrows. Obviously, the calculated E_i agree well with the experimental data providing the evidence for the electron confinement in GeSi/Si QDs stacked in a multilayer structure.

In summary, admittance spectroscopy was employed to study electronic structure of single and multiple layers of GeSi islands embedded in an *n*-type Si(001) matrix.

Fig. 37. Conductance and capacitance spectra of the multilayer QD sample at the bias voltage of 0 V under different modulation frequencies. The frequencies are 10 kHz, 30 kHz, 100 kHz, 200 kHz, 400 kHz, 600 kHz, and 1 MHz.

For a multilayer sample, the evidence for an electron localization in strained Si in the vicinity of GeSi dots was found. From the admittance measurements the electron
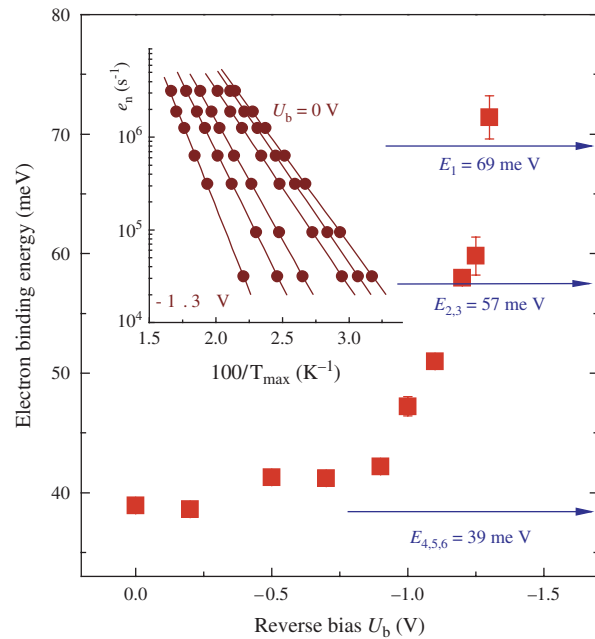
Fig. 38. Bias dependent activation energies of electron emission rate. The arrows show the calculated electron binding energies for the average Ge content of 80%. Inset displays the Arrhenius plots of the electron emission rate e_n obtained from $G–T$ spectra with different bias voltages. The voltages are 0 V, −0.5 V, −0.9 V, −1.1 V, −1.2 V, and −1.3 V.

binding energy was determined to be 40–70 meV. The electron accumulation was not observed in a sample with a single layer of GeSi islands. Existence of localized electronic states is explained by a modification of the conduction band alignment induced by inhomogeneous tensile strain in Si around the buried GeSi dots.

6. HOLE TRANSPORT AND CORRELATION EFFECTS

In a single quantum dot weakly coupled by tunneling barriers to two leads, the interplay of single-electron charging effects and resonant tunneling through quantized states leads to conductance oscillations as the electrochemical potential of the dot is tuned.[146] This phenomenon underlies working of nano-scale single-electron transistors that have a number of practical uses, ranging from metrology to computing. Recently, researches focused on the double-dot systems[147] whose behavior is found to be mainly affected by electrostatic coupling between the two dots inside the artificial molecule. The next step is to create and study large arrays of QDs in close proximity, allowing Coulomb interaction and tunneling between them.[148] Such systems can be considered as potential electronic networks for quantum computers[149] and therefore are particularly valuable in future high-power digital processors. The behavior of a multi-dot structure is expected to be more complicated for several reasons:

(1) The QDs are inevitably not sufficiently identical in size that can cause smearing of their atomic-like properties.

(2) In contrast to a single dot, the interaction of the charged dots in an ensemble can be significant.

(3) Transport through the system may be dominated by thermally assisted hopping between the dots rather than by resonant tunneling between source and drain electrodes.

Variable-range hopping (VRH) is a general conduction mechanism in systems with strongly localized carriers at sufficiently low temperatures. In a regime of VRH, the hopping distance increases as temperature is lowered, and the temperature dependence of conductivity is given by

$$G(T) = G_0 \exp[-(T_0/T)^x] \qquad (24)$$

where, in the two-dimensional case in the absence of long-range Coulomb interaction, the exponent $x = 1/3$ and $T_0 \equiv T_M \propto [g(E_F)\xi^3]^{-1}$ (Mott VRH); $g(E_F)$ is the density of states in the vicinity of the Fermi level E_F and ξ is the localization radius. If the interaction energy of a displaced electron and the hole it leaves behind is large compared with disorder energies, the conductivity is described by the Efros-Shklovskii (ES) law with $x = 1/2$ and $T_0 \equiv T_{ES} \propto e^2/(\epsilon_r\xi)$, where ϵ_r is the relative permittivity.

In this section, we describe a set of experiments in which we have studied hopping transport in Si metal-oxide-semiconductor field-effect structures containing a two-dimensional array of Ge self-assembled quantum dots

as a conductive channel.[91] The dots are separated from each other by weakly doped silicon, and the only conduction mechanism at low temperatures is tunneling of holes between them. The pseudomorphic Ge islands grown epitaxially on a Si(001) surface exhibit a large band discontinuity in the valence band and can be viewed as doping "artificial atoms." They provide a system in which the number of confined holes, the structure of energy levels, the shape of wavefunctions, and the strength of interaction can be controlled. First, we discuss the field effect and the temperature dependence of conductance of the samples with dots whose occupation with holes was changed by varying the potential of a gate electrode. Second, we describe the effect of screening in samples in which the holes on the dots are supplied by a boron δ-doping layer near to the QD layer. And, finally, we discuss the phenomenon of spin correlations in the hopping magnetoresistance.

Samples were fabricated on a silicon-on-insulator (SIMOX) wafer (*p*-type Si substrate, 400 nm buried SiO$_2$ and 170 nm top Si) or on a semi-insulating *p*-Si substrate with resistivity of 1000 Ω cm by molecular-beam epitaxy in the Stranskii-Krastanov growth mode. The amount of Ge deposited was 10 ML, the deposition temperature $T_s = 300$ °C. From scanning tunelling and transmission electron micrographs of similarly grown samples, we observe the Ge dots to be approximately 15 nm in diameter and 1.5 nm in height. Their dimensions vary within a 20% range. The areal density of the dots is 3×10^{11} cm^{-2}.

For the field effect measurements, the channel was patterned by photolitography to form a Si island of 100 μm width and 108 μm length, etched down to the underlying SiO$_2$ (Fig. 39(a)). The thickness of the Si cap layer (d_{Si}) in this case was 40 nm. Source and drain electrodes were made using Al evaporation and annealing at 450 °C in a N_2 atmosphere. A plasma-enhanced chemical-vapor deposition oxide of 60 nm thickness was deposited as the gate insulator and, finally, a square-shaped (100×100 μm^2) Al gate was deposited. (The distance between the gate and the dot layer in this set of samples, 100 nm, was large enough to avoid screening effects in the temperature range investigated.) The active channel of this type of samples contains about 3×10^7 Ge dots.

In the samples used for the experiments with screening, the holes on the dots are supplied by a boron δ-doping layer near to the QD layer (Fig. 39(b)). The number of holes per a dot was varied from 1/2 to 13/2 by varying the doping. The silicon cap layer has a thickness of $d_{Si} = 10$ nm. Au source and drain electrodes were deposited on top of the structure and heated at 400 °C to form reproducible Ohmic contacts. A thin ($d_{SiO_2} = 25$ nm) layer of anodic SiO$_2$ was grown to separate the conductive channel (dot layer) from a Au screening electrode (100 nm thick) which was deposited over the oxide parallel to the dot layer. The screening layer was only deposited between

(a)

(b)
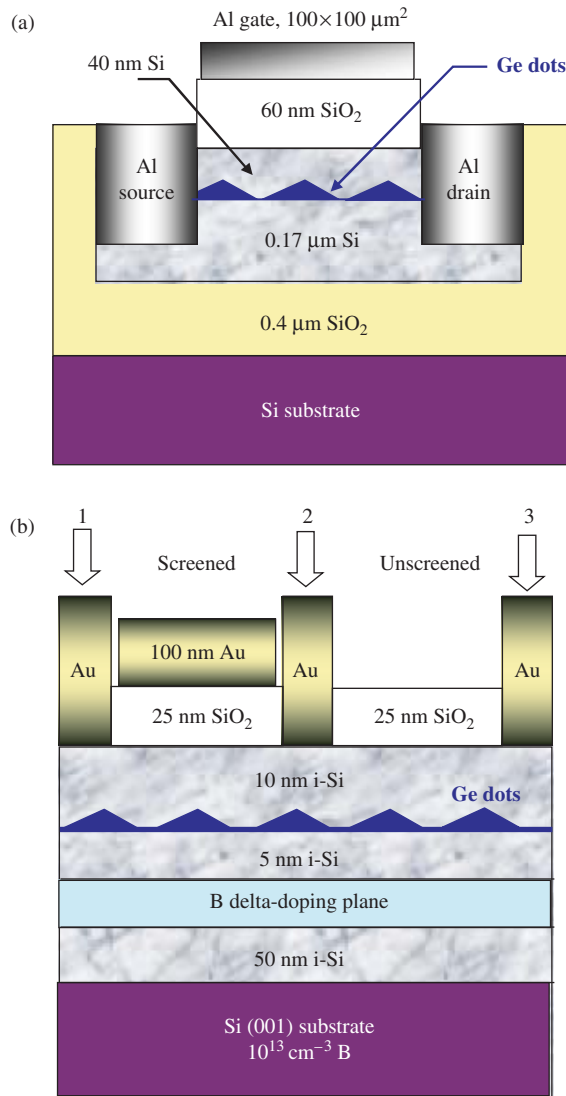
Fig. 39. Schematic diagram of the structure of the samples used for the field effect experiments (a) and for the experiments with screening (b). Screened samples are defined by the contacts 1 and 2, whereas unscreened samples are measured between 2 and 3. Each sample is a strip 7 mm long and 5 mm wide.

contact 1 and 2 and this area (7×5 mm²) provides the screened sample with a screening length $d = d_{Si} + d_{SiO_2} = 35$ nm. A corresponding unscreened sample is provided by the area between contacts 2 and 3 which has no screening layer. Samples prepared in a similar way but containing no dots were not conductive at low temperatures.

6.1. Field Effect in Array of Charge-Tunable Quantum Dots

The channel conductance ($G \equiv I_d/V_d$) of a sample shown in Figure 39 versus the gate voltage in linear and semilog-arithmic plots is depicted in Figure 40. At room tem-perature, the G–V_g characteristic shows a shoulder which evolves into a broad conductance peak in the voltage
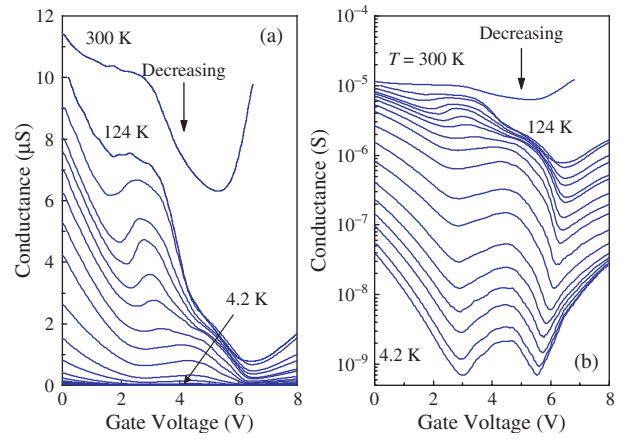
Fig. 40. Channel conductance versus gate voltage characteristics in lin-ear (a) and semilogarithmic (b) plots. The source–drain voltage is 10 mV. The temperature decreases from top to bottom.

range from 2 V to 6 V as the temperature decreases. To analyze the peak's structure, we subtract the smoothly varying background (see below). After the background is subtracted, the conductance modulation can be very well described by a sum of four Gaussian peaks. Figure 41 demonstrates the result of decomposition of the several experimental curves into four Gaussians, labeled as QD6, QD5, QD4, and QD3. We label the dot states in terms of the number of holes on each dot. For example, the peak observed at $V_g \approx 5.5$ V is labelled QD3 because it corre-sponds to loading of the third hole into the dots, this hole entering the first of the excited states with the two ground state levels already fully occupied. The peak corresponds to a mean loading of 5/2 holes per dot.
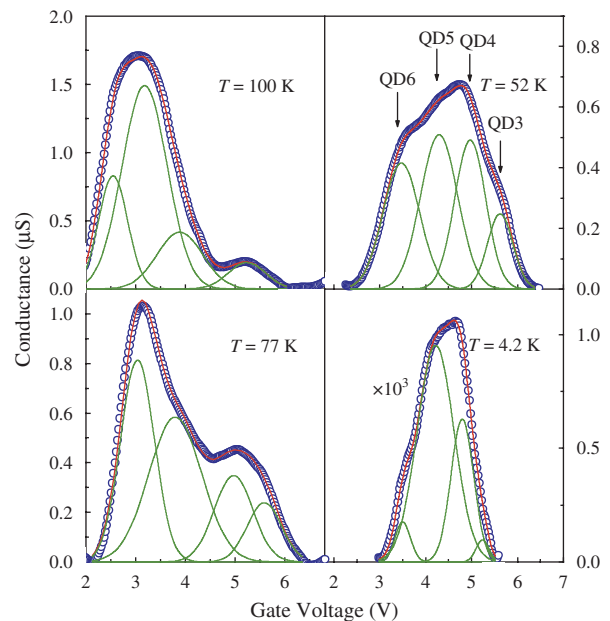
Fig. 41. Dot conductance versus gate potential for four temperatures. Circles show the experimental data with the background subtracted; solid lines give the result of decomposition into Gaussians.
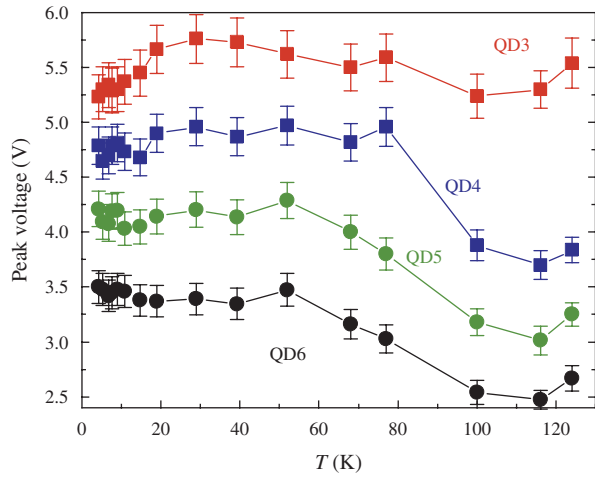
Fig. 42. The position of the peaks in Figure 41 as a function of temperature.

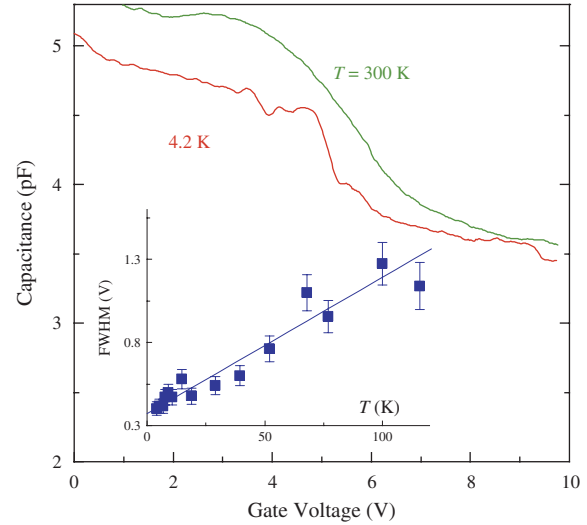**Fig. 43.** Capacitance–voltage characteristics. The capacitance was measured between the source and drain joined together and the gate. Inset: Temperature dependence of FWHM of the QD3 peak in Figure 41 with a linear fit to the data.

The position of those peaks as a function of temperature is displayed in Figure 42. Clearly, the fourfold structure with a gate voltage separation $\Delta V_g \approx 0.7$ V between the peaks is well-defined and completely reproducible over the whole temperature range. The observed shift of the peak's position to lower gate voltage at $T > 80$ K is attributed to the temperature induced diminishing of the Si and Ge band gaps. This effect is commonly observed in the photoluminescence measurements performed on the samples with QDs at different temperatures.

To demonstrate that the observed conductance peaks come from charging of the quantum dots, we first estimate the charge density induced by the change in the gate voltage ΔV_g and compared this quantity with the density of QDs. A change of gate potential ΔV_g induces a change Δn in the two-dimensional carrier density given by $\Delta n = C_g \Delta V_g / e$, where C_g is the capacitance per unit area between the gate and the dot layer. Taking the geometrical parameters of the gate, relative permittivity $\epsilon_r = 3.9$ for SiO$_2$, $\Delta V_g = 0.7$ V for the separation of successive peaks, and supposing the electrostatic fields are 1-dimensional, we find $C_g = 4.7 \times 10^{-4}$ F m^{-2} and $\Delta n \approx 2.1 \times 10^{11}$ cm^{-2}. The latter value is consistent with the density of quantum dots, $n_{QD} \approx 3 \times 10^{11}$ cm^{-2}, strongly supporting the interpretation that each constituent conductance peak originates from loading of *one hole* into each dot. The maximum conductivity occurs when the given level is half-filled as this maximizes the product of possible initial and final states for the tunnelling process that avoids increasing on-site correlation energy.

The above analysis can be checked by using C–V_g measurements to verify the electrostatics necessary for charging of the dots. We measured the capacitance between the source and drain connected together and the gate. Remember that the source and drain contact the underlying Si. The 100 kHz C–V_g characteristics at $T = 300$ K and at 4.2 K are shown in Figure 43. The capacitance

falls with increasing V_g corresponding to the increasing depletion layer thickness in the Si below the gate oxide. At 4.2 K, we see, superimposed on the falling capacitance, structure in the 3–6 V range associated with filling of the excited state and also structure in the 8–9.5 V range which we attribute to filling of the twofold degenerated ground state. We may use values of C_g together with the background acceptor concentration in the Si, $N_B = 7 \times 10^{16}$ cm^{-3} (determined by Hall measurements) to estimate the electrostatic configuration at various values of V_g. At $V_g = 9.5$ V, just before filling of the ground state levels, $C_g \approx 3.4$ pF which corresponds to the depletion layer extending to some 88 nm below the dot layer. The corresponding band bending between the deep Si and the dot layer is 414 mV. Just before the extended states start to fill, $C_g \approx 3.7$ pF and the depletion thickness below the dot layer is 62 nm with a corresponding band bending of 220 mV. These simplistic results are compatible with the known Si–Ge valence band offset and the expected energies of the hole bound states.[85] After the excited states are filled, $C_g \approx 4.7$ pF implying that the effective boundary of the depletion region is now at the dot layer. The depletion layer thickness d_d then continues to fall as V_g is decreased. At $V_g = 0$ V, $d_d = 23$ nm and the dot layer is about 17 nm into the unperturbed Si. The capacitance measurements are thus consistent with the interpretation of the conductivity results.

At large positive V_g, capacitance only decreases weakly with increasing gate voltage in contrast to the conductance which shows a strong rise (see Fig. 39). Separate measurements confirm that in this region leakage current through the insulator becomes comparable with the source–drain current. Therefore we conclude that the apparent increase of background conductance at $V_g > 6$ V is is a result of leakage through the gate SiO$_2$.

REVIEW

The energy level separation (ΔE) of the different charge states in the dots can be estimated by using $\Delta E = \eta e \Delta V_g$, where the gate modulation coefficient η relates the gate voltage to the hole energy inside the dot. This coefficient can be determined in two ways. One way is to calculate η from the temperature dependence of the full width at half maximum (FWHM) of the conductance peaks which should be broadened with T as $3.5 k_B T/(\eta e)$. By measuring the FWHM of the peak QD3 as a function of temperature (Fig. 42), we obtain $\eta = 3.4 \times 10^{-2}$ with a residual FWHM of about 0.37 V which is a result of statistical fluctuation in the dot ensemble. Another way of calculating η has been proposed in Ref. [151]. When most of the charge induced by a change of gate voltage, ΔV_g, is captured by the QDs as discussed above, then the change in potential of the dot is given by $\Delta\phi = e\Delta n/C_{QD} = C_g\Delta V_g/(n_{QD}C_{QD})$, where C_{QD} is the dot self-capacitance. Thus $\eta = \Delta\phi/\Delta V_g = C_g/(n_{QD}C_{QD})$. The value of C_{QD} for a disk-shaped dot with diameter D in classical electrostatics is given by $C_{QD} = 4\epsilon_r\epsilon_0 D$. For $D = 15$ nm and $\epsilon_r = \epsilon_{Si} = 11.7$, this yields $C_{QD} = 5.5$ aF and $\eta = 3.5 \times 10^{-2}$. Obviously, the agreement between the two above estimates of the gate voltage-dot energy modulation coefficient is very satisfactory. Based on these calculations the estimated charging energy is about 23 meV. Again, this value is consistent with the results of tunneling spectroscopy described in Section 4.1.

A useful way to identify the mechanism of carrier transport is to study the temperature dependence of conductance. In the regime of resonant tunneling through discrete energy levels, conductivity depends weakly on temperature. The current peak height should increase as the temperature is reduced due to diminished thermal broadening of the resonance. In contrast, hopping conduction is thermally activated. Figure 44 shows the temperature dependence of the four conductance peaks, QD3–QD6. For all maxima (symbols) we see a temperature-dependent activation energy reminiscent of variable-range hopping. A best fit to these curves (dotted lines) indicates that below 100 K the temperature dependence can be described by Eq. (24) with $x \simeq 0.5$ and $T_0 = 395$–565 K (see Table III).

We can check the hopping model for our structure and extract a value of localization radius ξ by making a quantitative comparison with the theoretical prediction. With $k_B T_0 = 6.2 e^2/(4\pi\epsilon_r\epsilon_0\xi)$ (Ref. [152]) the spatial dimension of the wave functions is found to be $\xi = 15$–21 nm (Table III). For variable-range tunneling to be occurring, the temperature dependent optimum hop distance $R_{opt} = 0.25\xi(T_0/T)^{1/2}$ must be larger than both the localization length and inter-dot distance (3–4 nm). At $T = 10$ K and with $T_0 = 395$–565 K, we have $R_{opt} = 29$–34 nm. Therefore these conditions are satisfied.

To obtain further evidence to support a hopping mechanism in the MOSFET, we have fabricated two test samples without any oxides or gate. Both samples contain a
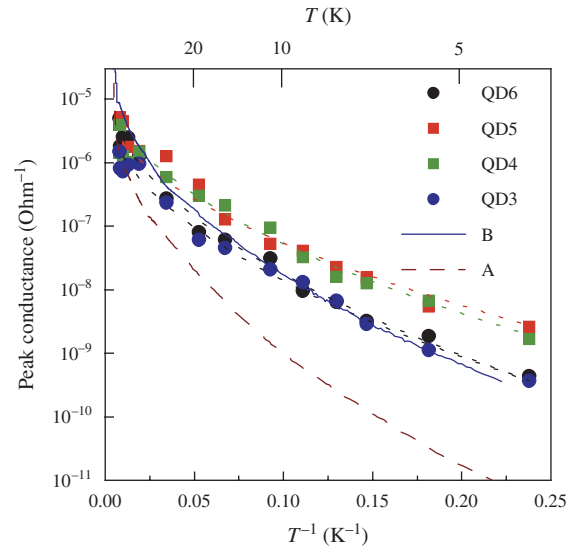
Fig. 44. Temperature dependence of the conductance maxima (symbols). Dotted lines are the best fit of the experimental data to Eq. (24). Broken and solid lines represent the temperature dependence of conductance in the test samples A and B, respectively (see the text).

remotely doped layer of Ge SAQDs grown on a semi-insulating Si(001) substrate. In sample A the doping level is such that only the ground state contains holes, there being 3/2 holes per dot taken from impurities, while in sample B, the ground state is full and the first excited state is partially occupied with a total of 5/2 holes per dot. The results of $G(T)$ measurements for the two samples are shown in Figure 44 by solid and broken lines, respectively. For both samples, best fits again give $x \simeq 0.5$, with $T_0 = 1176$ K for sample A and $T_0 = 581$ K for sample B. The latter is close to the value found for the corresponding state (QD3) in the MOSFET structure (see Table III). Moreover, the actual values of $G(T)$ for sample B match the temperature dependence of conductance maximum QD3. These results provide strong support for the assertion that the observed conductance oscillations do originate from hopping of holes through the discrete energy levels of the first excited state.

6.2. Crossover from Efros-Shklovskii to Mott Variable-Range Hopping

It should be remarked that the ES form for $G(T)$ does not necessarily result from intersite correlations. It only

Table III. Fitting parameters for the variable-range-hopping conduction through the charge-tunable quantum dots in the field-effect transistor.

Conductance maximum	x	T_0 (K)	ξ (nm)
QD6	0.49 ± 0.11	565 ± 58	15.4 ± 1.6
QD5	0.49 ± 0.14	395 ± 48	21.4 ± 3.1
QD4	0.51 ± 0.14	405 ± 49	21.1 ± 2.2
QD3	0.51 ± 0.10	536 ± 52	16.2 ± 1.5
Sample A	0.50 ± 0.01	1176 ± 36	7.6 ± 0.2
Sample B	0.51 ± 0.01	581 ± 37	15.0 ± 0.9

requires a density of states having the appropriate dependence on energy in the vicinity of the Fermi level.[153] In this section, we demonstrate that the hopping conductance of an array of QDs may be enhanced substantially and show crossover from ES VRH to Mott VRH with decreasing temperature, by putting the dot layer in proximity with a metal plane. The results provide strong evidence for the dominant role played by long-range Coulomb interaction between the charges of distant dots in electronic transport in dense ensembles of QDs.

The large spatial scale of intersite correlations allows one to examine the role of Coulomb interaction experimentally by making use of intentionally-introduced screening. If one places a metal plane parallel to the conductive channel at a distance d, the interaction may be described by including images of the real charges in the screening electrode. If the separation of initial and final states in a hop is small compared with the distance between a charge and its image ($= 2d$), the screening electrode makes little difference and the interaction remains monopolar. At large distances, however, a charge and its image behave as a dipole and interactions fall off more rapidly with distance. The general expression for the interaction potential is Ref. [154]

$$U(r) = \frac{e^2}{4\pi\epsilon_r\epsilon_0}\left(\frac{1}{r} - \frac{1}{\sqrt{r^2 + 4d^2}}\right) \quad (25)$$

Thus, distance d plays the role of a screening length. This means that, at low temperatures, when the hopping distance becomes longer than about $2d$, initial and final states become electrostatically independent and one should observe breakdown of ES VRH and crossover to a Mott regime with $x = 1/3$ in two dimensions. One would expect the screened conductance to be larger than that in the unscreened regime. However, Entin-Wohlman and Ovadyahu[155] found a reduction of hopping conductivity and transition to a simply activated law in screened In_xO_y film. Similar behaviour was obtained by Adkins and Astrakharchik in experiments with ultrathin bismuth films.[156] The explantion put forward was that in those systems the screened hopping was to nearest neighbours with the observed activation energy simply a characteristic disorder energy. Only Van Keuls et al.[157] have reported the observation of a universal crossover from ES to Mott hopping, driven by variation of temperature, magnetic field and electron density in GaAs/AlGaAs MSFETs.

It should be pointed out that, in the Mott regime of a screened system the effective (constant) density of states is not that which would be present in the absence of interaction. It is only the low-energy interactions, those corresponding to long distances, that are screened, and they are the interactions responsible for suppression of the density of states at low energies, close to E_F. At higher energies, the density of states still falls off similarly to the unscreened ES situation. Thus, the constant density

of states at low energies when there is screening is not equal to some background density of states but is given by the ES density of states at the energy corresponding to charges separated by the effective screening length ($\sim 2d$). The density of states at low energies with screening thus depends only on d and the local relative permittivity. One obtains[154]

$$g(0) = \alpha(4\pi\epsilon_r\epsilon_0/e^2 d) \quad (26)$$

where α is a numerical constant estimated in unpublished calculations by Mogilyanskii and Raikh as $\alpha \approx 0.1$ (see Ref. [154]).

Here we present results of low-temperature conductance studies in two types of samples. The samples of the first type (to be referred to as "screened samples") have a planar metallic gate close to the dot layer. (The distance between the channel of QDs and the gate is $d = 35$ nm.) Samples of the second type (reference or unscreened structures) contain no gate electrode. The top oxide layer is present in both cases, however. In all structures the holes on the dots are supplied by boron impurities. The temperature dependence of the conductance $G(T)$ of screened and unscreened samples is shown in Figure 45 as Arhenius plots. In contrast with the experiments,[155, 156] the low temperature conductance of the screened QD systems is found to be larger than that of unscreened samples except for the $N = 1/2$ sample where $G(T)$ does not change significantly with screening (in the range of temperature studied).

To analyze the characteristic behavior of $G(T)$, we examine the temperature dependence of the reduced activation energy $w(T) = d\ln G/d\ln T$.[158] For an exponential hopping dependence of G, $w(T) = x(T_0/T)^x$ and

$$\log_{10} w(T) = A - x\log_{10} T; \quad A = x\log_{10} T_0 + \log_{10} x \quad (27)$$
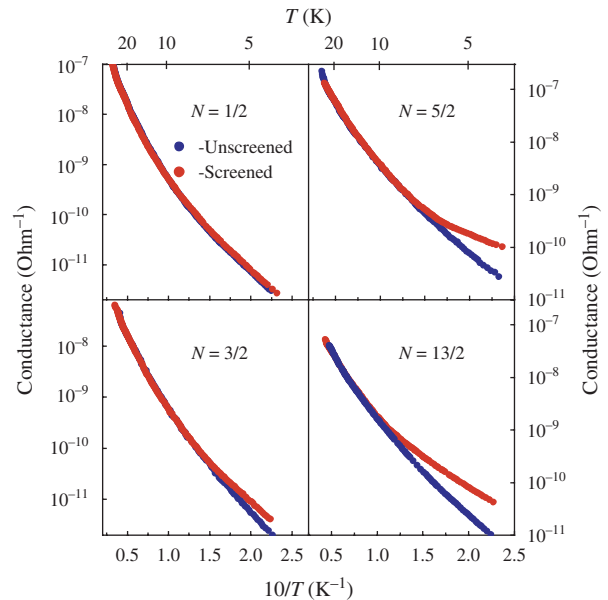
Fig. 45. Temperature dependence of conductance for various dot occupation N.
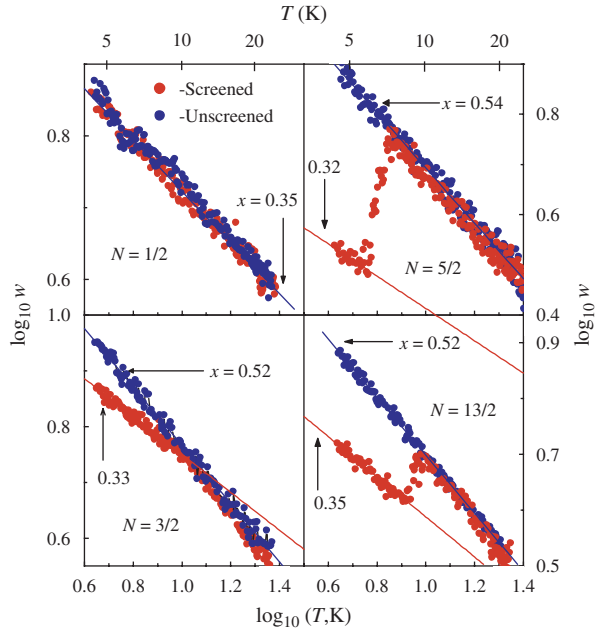
Fig. 46. Plot of $\log_{10}$ of the dimensionless activation energy w against $\log_{10}T$. The solid lines are least-square fits to linear dependencies. The slopes of the solid lines yield the hopping exponents x, and the characteristic hopping temperature T_0 is found from the y intercepts. The fitting parameters of all the curves are listed in Table IV.

Thus a plot of $\log_{10} w(T)$ against $\log_{10} T$ yields the values of the exponent x from the slope and of the characteristic temperature T_0 from the y intercept A: $T_0 = (10^A/x)^{1/x}$. Figure 46 contains $w(T)$ data obtained by numerical differentiation of the $G(T)$ curves. Linear regression was used to determine the best slopes x and the best intercepts A for both high and low temperature intervals (solid lines in Fig. 46).

The fitting results are summarized in Table IV. In unscreened samples with $N > 1/2$, the slope of the w plots yields $x \approx 0.5$, consistent with ES VRH over the whole temperature range. Screened samples with $N > 1/2$, however, exhibit a crossover from ES VRH at high temperatures to Mott VRH, with $x \approx 1/3$, at low. As explained above we expect this to occur when the optimum hop distance, $R_{\rm opt}$, becomes greater than the screening length.

Table IV. Fitting parameters for the variable-range hopping conduction through the quantum dots in screened and unscreened regimes.

| | | Data at $T > T_{\rm cross}$ | | Data at $T < T_{\rm cross}$ | | |
| | | | $T_0 = T_{\rm ES}$ | | $T_0 = T_{\rm M}$ | $T_{\rm cross}$ |
N	Screened	x	(K)	x	(K)	(K)
1/2	No			0.38	4.8×10^4	
1/2	Yes			0.35	5.4×10^4	
3/2	No	0.52	1260			
3/2	Yes	0.53	1392	0.33	4.3×10^4	6.5
5/2	No	0.54	900			
5/2	Yes	0.52	890	0.32	1.0×10^4	6.7
13/2	No	0.52	1044			
13/2	Yes	0.54	1072	0.35	2.6×10^4	8.7

We return to the $N = 1/2$ results. Here, screening only produces a very small reduction in x from 0.38 to 0.35 and no crossover is seen. The absence of ES VRH for this sample can be understood as follows. At $N \ll 1$, most of the dots contain neither holes nor nearby impurities and are neutral. A dot is charged only when it contains a carrier (hole) supplied by the rare impurities. Since a displaced hole leaves behind the neutral state, the correlation between initial and final sites in most of hops becomes unimportant, relevant energies are dominated by disorder and one observes Mott conduction. In fact, one should remember that not all transitions are from singly charged sites to neutral sites so correlation energies are not entirely absent. This is probably why the hopping exponent in the $N = 1/2$ sample is slightly larger than 1/3 predicted for the "pure" Mott hopping.

An interesting feature of our results is the form of the transition as seen in the temperature dependence of w shown in Figure 46. First, the transition is extraordinarily sharp. If it simply resulted from a situation in which two different processes were present with the transition occurring as one becomes more dominant than the other, then one would expect it to be much more spread out. Second, with larger values of N, we see an actual discontinuity of w at the transition. There is a certain resemblance to second-(3/2) and first-order ($N = 5/2$ and 13/2) thermodynamic phase transitions. One wonders whether there may not be a cooperative aspect to the transition from the Mott to the ES regime as correlation energies become greater. A possible explanation of such cooperative behavior at low temperatures can be formation of a 2D Vigner crystal.

An important observation is that the crossover, when w is discontinuous, is characterized by a *drop* of w at $T_{\rm cross}$ corresponding to reduction of the hopping activation energy as a result of the screening. This behavior is reported for the first time and is a direct evidence for the suppression of long-range correlations between initial and final hole sites on the dots.

6.3. Universal Prefactor in Unscreened Regime of Variable-Range Hopping

Notice that the data obtained in the previous section imply a temperature-independent prefactor G_0. Figure 47 shows the conductance in units of e^2/h, the quantum of conductance, of unscreened samples with different dot occupation N plottted versus $T^{-1/2}$; the symbols are the experimental points and the broken lines are the least-squares fits to the $T^{-1/2}$ ES dependence. Here we also plot the amplitude of conductance maxima taken from Figure 44. An impressive feature is that all the curves extrapolate to the same prefactor $G_0 \simeq e^2/h$. This is more evident when $G(T)$ is plotted against the dimensionless parameter $(T_{\rm ES}/T)^{1/2}$ (see inset of Fig. 9). In this plot, the data collapse onto a single universal curve with intersept $G_0 = (1.05 \pm 0.05)e^2/h$. This observation is similar to that found
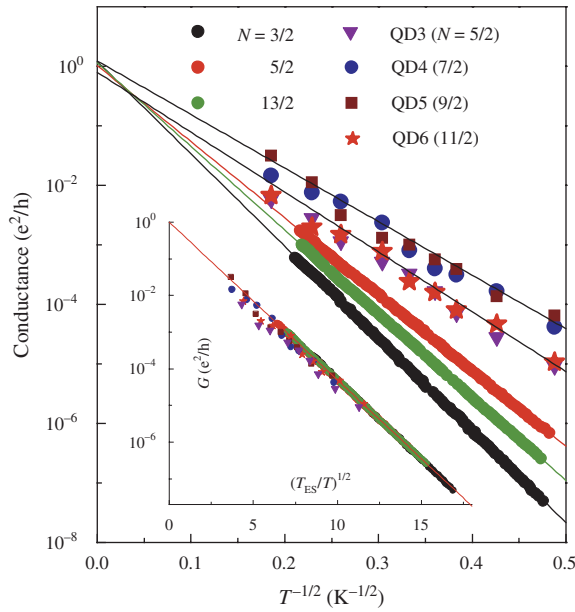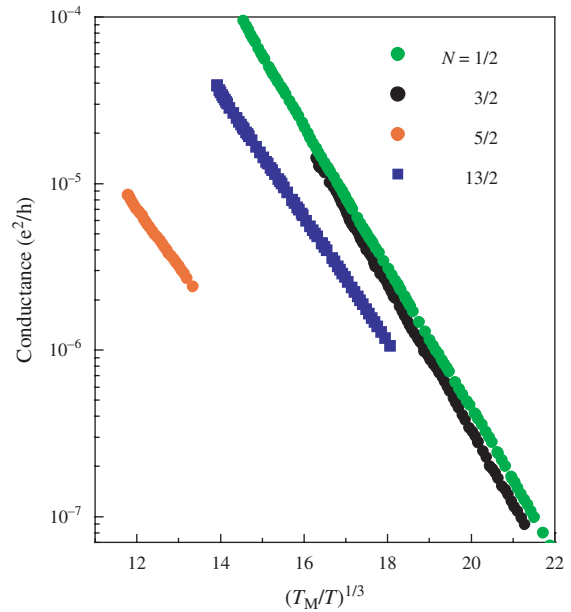
Fig. 47. The conductance $G(T)$ versus $T^{-1/2}$ for different dot occupation N in unscreened samples. Data from Figure 44 are also included. The inset shows the same data plotted versus $(T_{ES}/T)^{1/2}$.

Fig. 48. Plots of the conductance $G(T)$ versus $(T_M/T)^{1/3}$ for screened samples at $T < T_{cross}$.

for the two dimensional impurity hopping conductance in both ES and Mott unscreened regimes in Si MOSFET's[159] and in delta-doped GaAs/AlGaAs heterostructures.[160] Universality of the prefactor signals against the conventional phonon-assisted hopping mechansim where the prefactor would depend on material parameters such as the localization length. To resolve this descrepancy it was suggested by Kozub, Baranovskii, and Shlimak[161] that the phononless hopping is assisted by electron–electron interaction. According to this model the current-carrying single electron moves via quantum resonant tunneling between localized states brought into resonance by a time dependent random Coulomb potential created by fast electron transitions in their environment. The dependence of the fluctuation amplitude of energies of hopping sites on temperature gives rise to the temperature dependence of conductance.

If the universal prefactor does result from interaction, its universality would be destroyed in the presence of screening. The ratio $G(T)/(e^2/h)$ is plotted against $(T_M/T)^{1/3}$ in Figure 48 for data from screened samples at temperatures below T_{cross}. In contrast to the unscreened regime, the data do not collapse onto a single curve.

6.4. Spin Effects in Hopping Magnetoresistance

The localized states of holes in the Ge QD are characterized by the angular momentum **J** and its projection J_z on the growth direction z. This projection can be considered as an analog of electron spin for hole states. In this section, we describe how the hole spin can affect magnetoresistance in the hopping regime of hole transport through arrays of Ge QDs. The idea of this experiment is based on the results of recent theoretical calculations

which have demonstrated that probability of interdot tunneling processes with spin-flip for the hole states in 10-nm sized Ge QDs is two orders of magnitude smaller than that with spin conservation.[162] For simplicity, we will consider only the ground hole state with the maximum occupation $N = 2$ disregarding excited states due to the large ($\sim$50–70 meV) energy-level separation and neglect the intradot Coulomb correlations. When a magnetic field is applied, all hole spins in the system become polarized. For the average dot filling factor $N < 1$ and $N > 1$ the hopping of holes between QDs occurs with spin conservation (Fig. 49, top and bottom panels). When $N \approx 1$, the hopping transition is accompanied by the spin-flip process
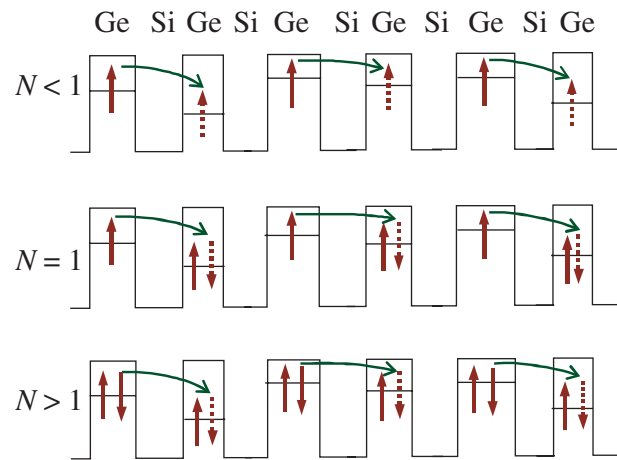
Fig. 49. The schematic sketch of the valence band profile along the layer of Ge/Si quantum dots and the interdot hole transitions (arrows denote hole spin orientation) in the presence of magnetic field at various dot filling factors N.
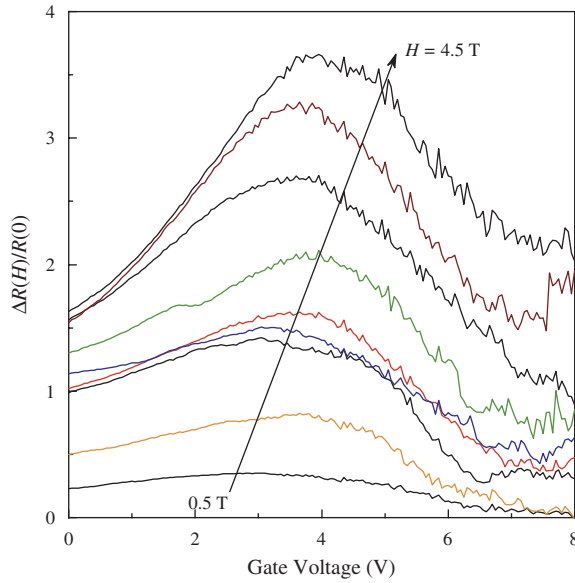
Fig. 50. Experimental magnetoresistance of a Ge/Si MOSFET as a function of gate voltage in different magnetic fields. The field varies from 0.5 T to 4.5 T with an increment of 0.5 T. Data were taken at $T = 4.2$ K.

(Fig. 49, middle panel) which has a much lower probability. The suppression of hopping process by a magnetic field gives rise to a positive magneoresistance (MR) resulting in a resonant increasing of the hopping MR at $N \approx 1$ due to spin correlations.

This prediction was checked for a Ge/Si metal-oxide-semiconductor field-effect transistor containing remotely doped Ge dots in a buried active channel.[163] The average filling factor of the QD array was varied by the gate potential V_g down to $N = 0$. Experimental results are shown in Figure 50. The MR peak emerging in a magnetic field and superimposed on the positive magnetoresistance is really observed at $V_g \simeq 4$ V. We suppose that the positive background is due to the wave function shrinkage effect while the MR peak is related to the spin correlations described above.

Summarizing this section, we have described a set of experiments in which we have studied hopping transport in field-effect structures containing from 3×10^7 to 10^9 quantum dots. We demonstrate that below ~ 100 K this system is able to show conductance oscillations associated with filling of the dots by successive single holes. From the temperature dependence of conductance maxima, we identify the conduction mechanism as variable-range hopping in a density of states determined by Coulomb interaction between the dots. In samples with screening, we observe a crossover from Efros-Shklovskii VRH with $\ln \sigma \propto T^{-1/2}$ to Mott VRH with $\ln \sigma \propto T^{-1/3}$ as temperature is reduced. The data in the ES regime collapses onto a universal curve with a prefactor $G_0 \simeq e^2/h$, while all traces in the screened regime do not show the universal behavior. The results demonstrates the important role of the long-range interdot Coulomb interaction and spin correlations in

the dense ensembles of quantum dots and they raise interesting issues relating to the mechanisms of the hopping processes.

## 7. OPTICAL PROPERTIES

7.1. Spatially Indirect Excitons

A fundamental feature of staggered QDs is the spatial separation of electrons and holes resulting in formation of spatially indirect excitons,[164, 165, 68] whose intriguing properties are still poorly understood. In particular, little is known about the influence of Coulomb interactions on the-excitonic properties of charged quantum dots.

In this section, we describe electron-filling modulationabsorption spectroscopy (EFA) used to study effect of dot charging on the interband transitions in Ge/Si SAQDs.[123, 124, 166, 167] This kind of spectroscopy has been also used to study photoluminescence[168] and reflectance[169] properties of charged InAs and In$_x$Ga$_{1-x}$As QDs. In the present experiments, Ge dots (15 nm in diameter) are embedded into a n^+–p–p^+ Si diode, in which the number of holes in the QDs can be finely tuned by an external applied bias. When a state is occupied by a hole, no interband transition from this state is possible (Fig. 51). When the hole is evacuated from the level, the interband transition is allowed. Modulating the holes in and out of the state by applying an ac bias voltage therefore induces corresponding changes in the infrared absorption. Thus the absorption signal measured under different bias conditions reflects directly properties of excitons at charged quantum dots.
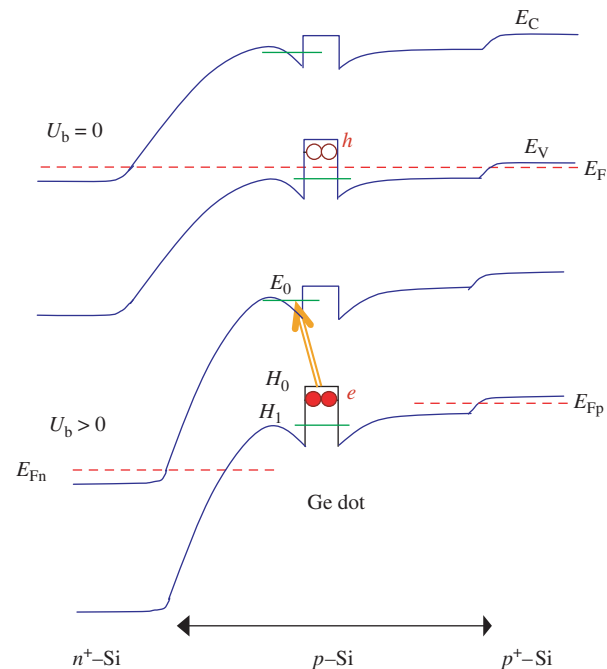
Fig. 51. Schematic of the band diagram of the sample under unbiased and reverse biased conditions.
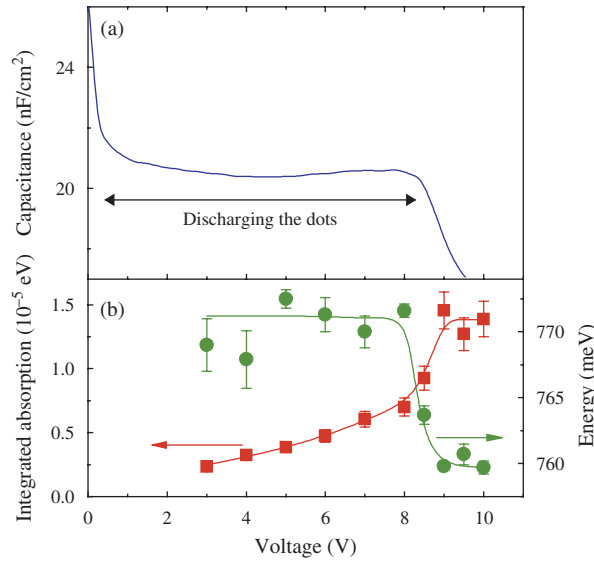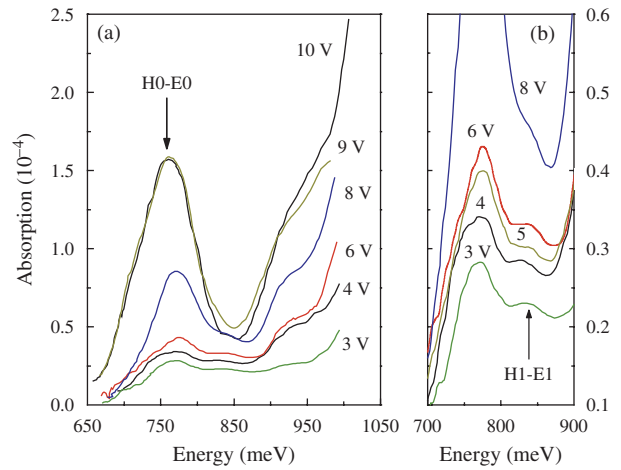
Fig. 52. (a) Capacitance–voltage characteristic measured at $T = 300$ K with a modulation amplitude 10 mV and a modulation frequency 100 kHz. (b) Integrated absorption strength of the $H0 - E0$ transition and its energetic position as a function of bias voltage U_b.

Fig. 53. (a) Room-temperature electron-filling absorption spectra at different reverse bias. (b) Expanded view of the spectra at low bias.

Infrared absorption measurements were performed in normal-incidence geometry on mesa diodes at room temperature. Unmodulated light from a globar source illuminated the front side of the diode. The transmitted light then passed through the monochromator and was detected by a Ge photodiode. Differential absorption was measured by applying a reverse bias modulated between a low level U_L and a high level U_H.

The 100 kHz capacitance–voltage characteristic measured at 300 K is shown in Figure 52(a) and illustrates the charge state of the sample investigated. To determine the position of the QD layer we used the approximate relation $L = \epsilon_0 \epsilon_r / C$, where ϵ_r is the relative permittivity. For $C \approx 20$ nF/cm², the result is $L = 0.5$ μm which is in agreement with the nominal position of the Ge layer. The dots are charged with holes at zero bias. The holes begin to escape at $U_B > 0.5$ V and the dots become totally depleted at $U_B > 8.5$ V (Fig. 52(a)). In the discussion that follows, we modulate the bias voltage between $U_L = 0$ V and $U_B = 2$–10 V. All measured EFA signals were normalized to the source spectrum so that any spectral response not associated with the modulated part of the sample is eliminated from the results. This approach is appropriate for the case of weakly absorbing samples.

Figure 53 shows the EFA signal measured at different values of the bias U_B. Below the energy gap of Si, at energies ≈ 760–770 meV, an absorption maximum with a Gaussian line shape and a broadening of ≈ 50–70 meV is observed and interpreted as indirect excitonic transition between the hole ground state ($H0$) in the Ge dots and the electron ground state ($E0$) confined in Si near the heterojunction.[124, 123, 166, 167] A similar peak at ≈ 730–750 meV has been observed in photocurrent spectra of a Ge/Si heterostructure with quantum dots of similar size.[37] The broadening of the interband transition is mainly due to the dispersion of the carrier confinement energies of dots with different sizes.

An additional fine structure at ≈ 850 meV is assigned to the transition between the hole excited state ($H1$) and the electron excited state ($E1$). The separation of the two hole states in the Ge dot is ≈ 70–80 meV.[91, 151] The energy difference between the $H0 - E0$ and $H1 - E1$ transitions is ≈ 90 meV. This implies that the separation of the two electron states, ≈ 10–20 meV, is much less than that for holes. A probable reason is that the holes are localized in a small dot, while the electrons are more spread out.

At higher energies, the absorption gradually increases due to excitations to extended states in the conduction band of Si and Ge, superimposed on the several absorption bumps, which are tentatively attributed to transitions between highly excited states in the dots or in the wetting layer. To make a careful analysis of the absorption edges, one should take into account the energy dependence of absorption coefficient for spatially indirect transition from a confined state to a delocalized band. Since a theoretical treatment of such a dependence is a formidable task, we will not make this analysis in the present work.

The assignment of the peak near 750 meV to the $H0$–$E0$ transition is supported by analysis of the integrated absorption I_a as a function of U_B (Fig. 52(b)). (I_a is obtained by calculating the areas under Gaussians fitted to the absorption peaks). In our geometry

$$I_a = he^2 n_e f / 2 m_0 \epsilon_0 c (1 + \sqrt{\epsilon_r}) \tag{28}$$

where n_e is the density of electrons in the highest valence band state of the Ge dots, f is the oscillator strength and c is the speed of light. Since $I_a \propto n_e$, the $I_a - U_b$ curve illustrates the change in the charge state of the dots. At $U_b > 8.5$ V, the integrated absorption does not depend on the voltage. Below 8.5 V, the EFA intensity weakens
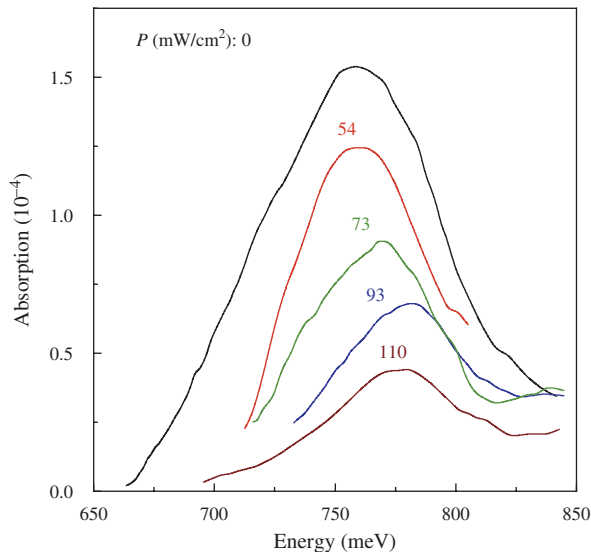
Fig. 54. Effect of optical pumping on the EFA spectra at different pump intensities. The modulation bias amplitude is fixed at $U_B = 9$ V.

Fig. 55. Ground-state transition energy as a function of the hole occupation per dot. The data were taken at different bias in the dark (solid squares), and at different pump intensities at fixed bias voltage ($U_b = 9$ V, open symbols).

indicating a decrease in the number of modulated electrons in the valence band of the dots, in agreement with the CV measurements.

To obtain further evidence to support the proposed origin of the EFA peak, we have studied the effect of additional interband optical excitation of the sample by a tungsten halogen lamp with a bandpass filter as source. The absorption spectra obtained at a fixed modulation voltage ($U_B = 9$ V) and at different pump excitation densities are depicted in Figure 54. When the sample is illuminated, nonequilibrium electrons and holes are photogenerated. The holes are captured by the dots while the electrons are accumulated near the dots forming the indirect excitons. At high pump intensities, the hole and electron ground states become fully occupied and the Pauli exclusion principle forbids the $H0 - E0$ transition. One can see in Figure 54 that the experimental EFA signal is strongly suppressed by the optical pumping.

The integrated absorption at $U_B > 8.5$ V can be used to determine the oscillator strength per dot. For the $H0 - E0$ transition, the density of absorbers is twice the dot density. (The maximum occupation of the ground state is 2). From the measured value $I_a \simeq 1.4 \times 10^{-5}$ eV we find $f = 0.5$. This value is more than twenty times less than that obtained for direct excitons in InAs/GaAs QDs (10.9).[170] Such a difference is not unreasonable since the difference between the two types of QDs is large. Similar conclusions were reached in Ref. [171] from analysis of the PL time decay of type-II GaSb/GaAs SAQDs. Large values of the oscillator strength and the exciton binding energy for type-II quantum dots with finite offsets was predicted by Rorison.[172] They are explained by two aspects of the system. The first is the localization of one of the particles which allows the other particle of the exciton to correlate more strongly with it. The second is leakage of the
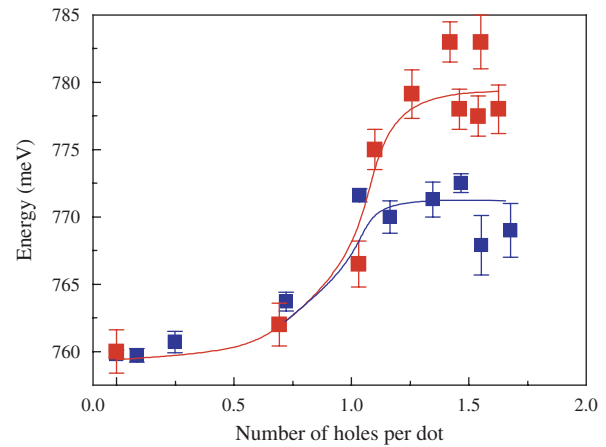
wave-functions into the barrier regions allowing greater overlap of electron and hole wave functions.

One of the results is that the $H0$–$E0$ transition shows a substantial stepwise blueshift of about 11 meV with decreasing reverse bias (Fig. 52(c)). A qualitatively similar effect is seen with increasing the pump excitation density at fixed U_B (Fig. 54). This result differs drastically from what has been observed for direct excitons, in which case charging leads to a redshift of the excitonic transition.[168, 170] It can bee seen in Figure 52(c) that the transition energy begins to increase when holes are injected into the originally empty QDs. From the oscillator strength obtained above and the measured integrated absorption we calculate the number of holes per dot, N_h, at different biases in the dark and at different pump intensities. The energetic position of the indirect excitonic transition is shown in Figure 55 as a function of N_h. It should be noted that the transition energy increases sharply when the first hole enters the ground state and then is approximately insensitive to further increase in the hole concentration.

When a $H0$–$E0$ exciton is created in a positively charged dot, an exciton–hole complex is formed consisting of two holes in the dot and an electron confined near the dot. There are two additional contributions to the energy of the exciton–hole complex as compared to e–h excitation in a neutral dot.[170] The first is a positive Coulomb energy due to correlation between the two holes in the dot, E_{hh}, and the second is a negative contribution from the Coulomb attraction between the excited electron in the nearby silicon and the second hole on the dot, E_{eh}. Here we neglect the exchange interaction between the two holes since they have antiparallel spin orientation.[173] For direct excitons, the electron–hole interaction dominates and the resulting shift $\Delta E_{h-ex} = E_{hh} - E_{eh}$ is negative.[170] Hence the expected reduction of the overlap factor for type-II excitons as compared with type-I systems yields a smaller magnitude of the electron–hole interaction energy E_{eh}. As a result, the

energy of the exciton–hole interaction referenced to a neutral exciton energy can be positive. Taking the experimentally observed shift of 11 meV and $E_{hh} = 36$ meV (see Section 4.1), the exciton binding energy is determined to be $E_{eh} = 25$ meV. Note that this value is consistent with theoretical simulation (Section 3.4).

As can be seen from Figure 55, optical pumping affects the transition energy more strongly than the bias voltage. This stems from the fact that illumination creates both holes and electrons while the field effect only induces holes in the dots. Under illumination we have two interacting excitons in the dot: the first is generated by the pump illumination, the second is excited by the infrared probing light. As compared to a single exciton, the transition energy now increases by $\Delta E_{ex-ex} = E_{ee} + E_{hh} - 2E_{eh}$, where E_{ee} is the energy of repulsive interaction between two electrons confined near the dot. For $\Delta E_{ex-ex} = 20$ meV, $E_{hh} = 36$ meV, and $E_{eh} = 25$ meV, we obtain a surprising results $E_{ee} = 34$ meV. It is quite improbable that E_{ee} could be so close to E_{hh} in a system where the hole states are more strongly localized that the electron states. This problem has been resolved by making self-consistent calculations of the expected electronic structure (Section 3.4).

The confining potentials for electron and hole along the vertical z axis in the structure and the carrier wave functions are given in Figure 56(a). Figure 56(b) shows the isosurfaces of the electron and hole wave functions. Note that the electron is localized near the dot apex, where the strain is maximum. The electron–hole overlap is calculated
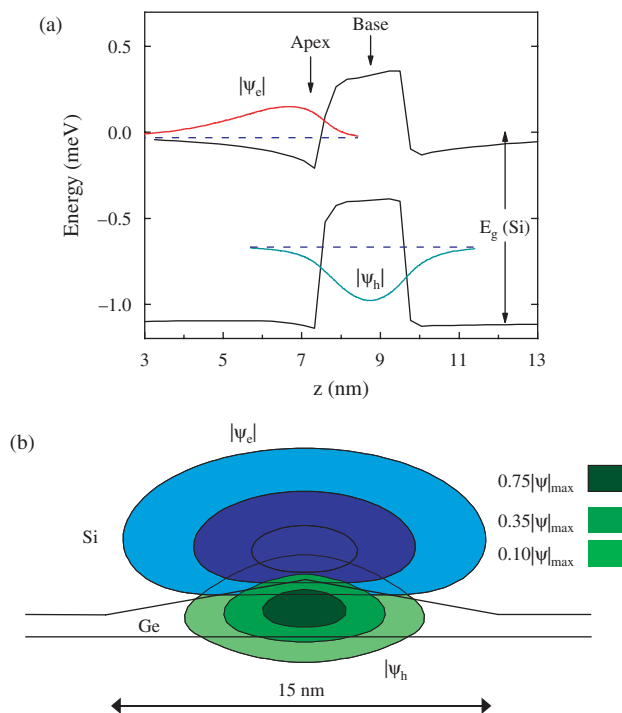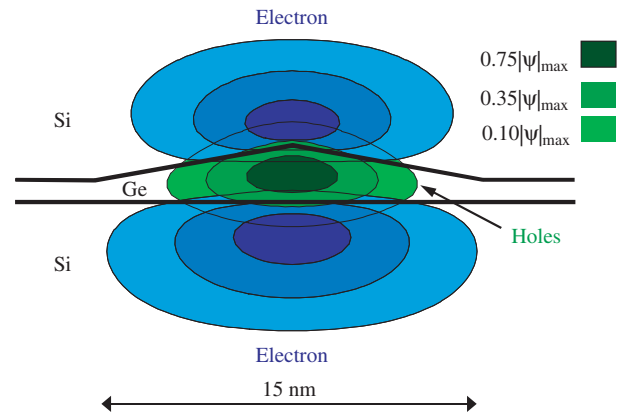
Fig. 57. Isosurface plots of the electron and hole states for a exciton–exciton complex.

to be 15%. If we take an electron–hole overlap of 80% for type-I InAs/GaAs SAQDs[174] and an oscillator strength of 10.9 as observed also for InAs/GaAs,[170] we expect for the dots with an electron–hole overlap of 15%, an oscillator strength of about 0.38, in a reasonable agreement with experiment (0.5).

The electron–hole interaction energy is calculated to be 31 meV, in a reasonable agreement with the exciton binding energy found experimentally (25 meV). The blueshift of the excitonic transition for the exciton–hole complex as compared to a single exciton is determined to be 9.7 meV that agrees with the experimental value 11 meV (Fig. 55).

The calculations were extended to examine the structure of the exciton–exciton complex. In Figure 57 we depict the the wave functions for two excitons in the dot. It would be worth mentioning that the two electrons in the exciton–exciton complex are *spatially separated*. Electron–electron repulsion causes the second electron to localize below the dot base. As a result, the *e–e* interaction energy turns out to be only 19 meV, i.e., about two times less than the energy of the *h–h* interaction.

7.2. Stark Effect in Ge/SiO$_x$/Si Quantum Dots

QDs display many effects known from atomic physics. One of such exciting phenomena is the red-shift of the optical transition induced by an electric field [so called, the quantum-confined Stark effect (QCSE)]. Recent theoretical[175–178] and experimental studies[179–182] reported for type-I InAs/GaAs and InGaAs/GaAs QDs, wherein the narrow-gap dot material presents a potential well for both electron and hole, demonstrated that the Stark shift can provide very useful information on the polarity of intra- and interdot electron–hole alignment and the vertical separation.

The change of the potential energy of a dipole with a moment **p** in an electric field **F** is given by $U = -\mathbf{p}\mathbf{F}$. For the electron–hole system, $\mathbf{p} = e(\langle \mathbf{r}_h \rangle - \langle \mathbf{r}_e \rangle)$, where $\langle \mathbf{r}_{e,h} \rangle$ is the mean electron (hole) position. In type-II QDs,

Fig. 56. The confining potentials and the wave functions for electron and heavy hole along the principle axis of symmetry in the dot (a). Isosurface plots of the electron and hole states (b).

only one of the charge carriers is confined inside the dot whereas another carrier resides outside the dot. In contradistinction with the case of type-I QDs, one can expect that in such a system the Stark effect should be extremely large because of the permanent spatial separation of electron and hole and the presence of the built-in electron–hole dipole.[178] To date, most work in the field of QCSE has concentrated on InAs/GaAs QDs, and little is known about Stark effect in excitonic transitions of type-II QDs.

As it has been already mentioned, Ge/Si(001) quantum dots exhibit a type-II band lineup. When an electron–hole pair is photoexcited, the hole is captured into the quantum well of the Ge dot and creates an attractive Coulomb potential resulting in a binding of an electron in Si (Fig. 58(a)) at the Si/Ge interfaces and forming the spatially indirect excitons. In this section, we will describe the effect of an electric field on the interband transitions in Ge/Si(001) quantum dots studied by photocurrent (PC) spectroscopy.[183, 184]

For controlled tuning of the electric field, the Ge QDs are embedded in the intrinsic region of an Si p–i–n diode (p^+ region uppermost), allowing fields up to 90 kV/cm to be applied parallel to the growth direction z (applying a reverse bias to a p–i–n structure results in an electric field pointing from n^+ substrate to p^+ surface). The band profile under reverse bias condition is shown schematically in Figure 58(b).
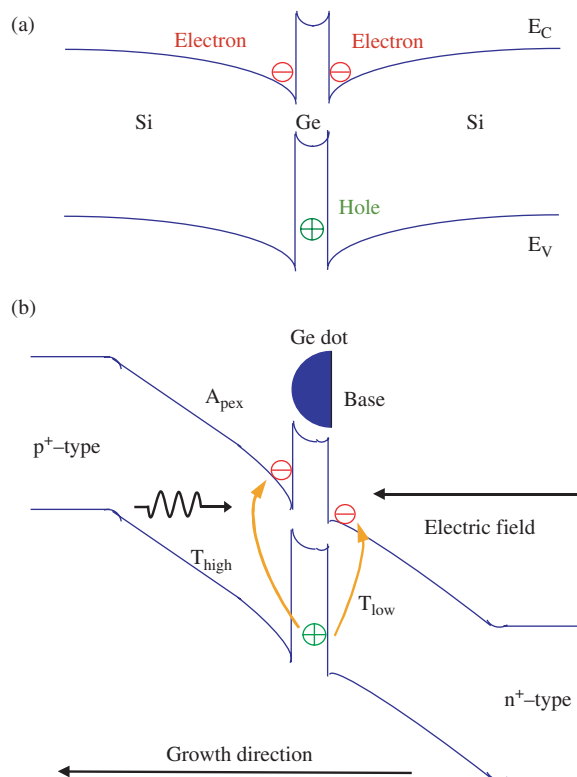

Fig. 58. (a) Band structure of the type-II Si/Ge/Si heterostructure along the growth direction through the center of the Ge dot. (b) Schematic band diagram of the p–i–n diode under reverse bias.

Ge/Si QDs, more suitable for the Stark spectroscopy, must meet the following conditions. First, the size of the dots in all three dimensions should be small enough to provide actual zero-dimensional density of hole states. In this case, the localization of hole in all three dimensions of Ge dot allows the electron in the Si conduction band to correlate more strongly with it, resulting in increase of the exciton binding energy as compared with quantum-well systems. Second, the electron and hole must be well separated to ensure the large dipole moment, so that the dots should be rather steep. However, conventional Ge/Si(001) self-assembled QDs, grown by Stranskii-Krastanov growth techniques, are always flat, i.e., they have an aspect ratio (height divided by base length) much less than unity.[37] To fabricate steep Ge islands with small lateral size, we grow the Ge dots on a Si(001) substrate covered with an ultrathin SiO$_x$ film. This approach uses Volmer-Weber growth mode and allows to form Ge nanoclusters which exhibit an epitaxial relationship with the underlying silicon substrate and reside on *bare* Si region similar to the case of Stranskii-Krastanov islands.[39] The Ge islands have a hemispherical shape with a base diameter of 5.8 ± 0.5 nm and a height of about 3–4 nm. The apex of the dots is oriented along the growth direction. The areal density of the islands was approximately 1.8×10^{12} cm^{-2} (Fig. 59).

Figure 60 shows photocurrent spectra as a function of reverse bias. There is an apparent PC peak below the silicon interband absorption edge (1126 meV) which is not seen in the reference sample without Ge SAQDs (violet line in Fig. 60). Since intra-valence band hole transitions in Ge/Si QDs occur at much lower energies (70–400 meV), the observed photocurrent maximum cannot be attributed to transition between hole states in the dots. At low bias, this peak has a symmetric line shape and is believed to come from the indirect excitonic transition between the hole ground state in the small Ge dots and the electron ground state confined in Si near the heterojunctions. The electron–hole pairs created by interband absorption thermally escape from the dots and give rise to the measured photocurrent. As the reverse bias increases, the current maximum becomes wider and splits into two peaks which are changed with the applied voltage in a different way. The position of the low-energy peak T_{low} is practically unchanged with the bias while the high-energy component T_{high} apparently shifts to *higher* energies.

To explain splitting and the blueshift of the high-energy transition, one needs to consider the electronic structure of excitons in type-II Ge/Si QDs. The modeling of the confined electron and hole states[68, 124] predicts that holes are concentrated at the bottom of the dot, and the electrons are localized in Si both on top and below the Ge island. This is the result of strain distribution and Coulomb forces around the dot. It follows from the second-order perturbation theory that the field dependence of the transition
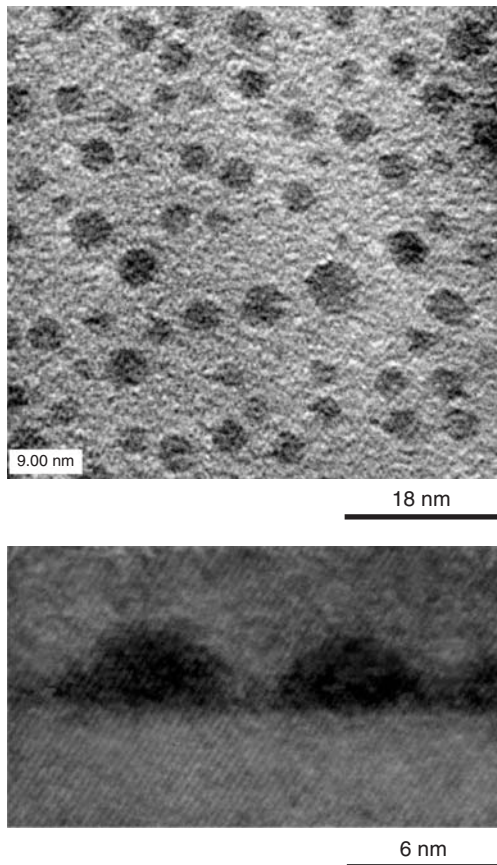
Fig. 59. Plan-view (top) and cross-section (bottom) transmission electron microscopy images of a dot sample. The Ge islands appear in dark contrast.
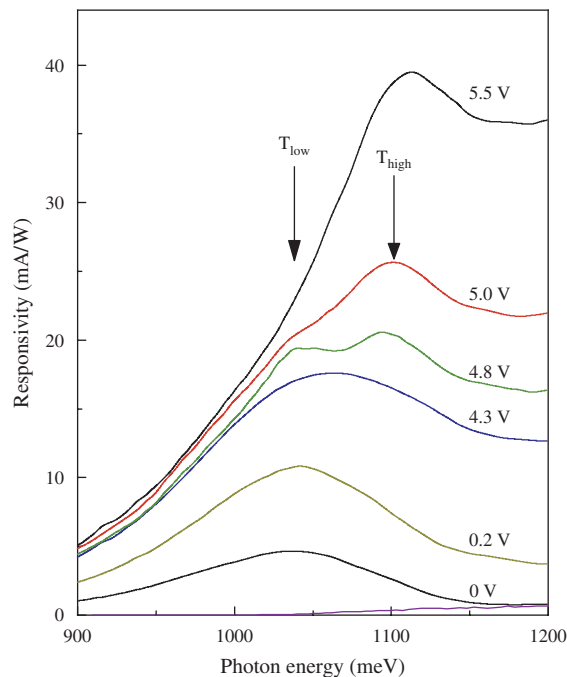
Fig. 60. Photocurrent spectra as a function of applied reverse bias (lines). The short circuit photoresponse from a reference Si photodiode containing no Ge SAQDs is shown by violet line.

energy can be described by

$$E(F) = E(0) - eF(\langle z_h \rangle - \langle z_e \rangle) - \beta F^2 \qquad (29)$$

where $e = -|e|$ is the electron charge, $E(0)$ is the transition energy at zero field, $\langle z_{e,h} \rangle$ is the mean electron (hole) position along the growth direction (along the nanocrystal axis), and β is the polarizability of the electron–hole system.[176] In a system possessing an extremely large nonzero dipole moment, the second order term in Eq. (29), quadratic in the applied field, may be less important than a linear one, and the transition energy is expected to vary linearly with the field.

In frame of this conception, the high-energy maximum T_{high} has been interpreted as a transition between the hole ground state in the Ge dot and the electron state confined in Si near the dot apex. The low-energy peak T_{low} is assigned to the transition between the same hole state and the electron state localized in Si near the dot base (see Fig. 58(b)). Obviously, the term $eF(\langle z_h \rangle - \langle z_e \rangle)$ is negative for the first case and positive for the second one since the electron–hole dipoles formed as a result of the T_{high} and T_{low} transitions have the opposite directions.

One can check this explanation by extracting the values of electron–hole and electron–electron separation from the observed Stark shift. Keeping in mind that the observed PC maximum is a superposition of the two peaks, the maximum was decomposed into two Gaussians. A self-consistent one-dimensional simulation of our *p–i–n* device was performed to calculate the electric field near the apex and the base of the dots. It was found that electric field is uniform across the intrinsic region and can be well described by $F = (U + V_{bi})/W$, where U is the applied reverse bias, V_{bi} is the built-in potential (~ 1 V), and $W = 0.8$ μm is the intrinsic region width. Independent capacitance–voltage measurements carried out on the samples demonstrated that W does remain unchanged within the bias range studied and equal to the nominal growth width. This supports our calculation.

The field dependence of the transition energies are plotted in Figure 61. As expected for a system with built-in dipole moments, the Stark shift for both transitions appears to be linear. Moreover, due to the linear behavior, the type-II Ge/Si QDs exhibit a QCSE of approximately one order-of-magnitude stronger than type-I InGaAs/GaAs QDs of similar height.[181] From a fit to the data using the Eq. (29), the electron–hole distance was found to be (5.1 ± 0.2) nm for the electron near the dot apex (top electron) and $-(0.8 \pm 0.3)$ nm for the electron near the dot base (bottom electron). It is worth to note that separation of these two electrons (≈ 6 nm) is somewhat larger than the mean dot height (≈ 4 nm), which is quite reasonable for QDs with a staggered band line-up and provides clear support for the explanation. The small separation of the bottom electron and the hole agrees with the fact that hole is localized towards the base of the dots.
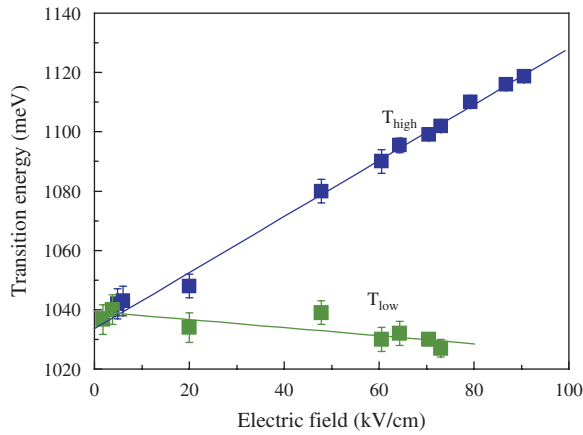
Fig. 61. Transition energies as a function of electric field. The solid lines are theoretical fits to the experimental data.

The magnitude of the exciton polarizability is found to be $\beta/e^2 = (120 \pm 100)$ nm^2/eV for the T_{high} transition and $\beta/e^2 = (1.5 \pm 60)$ nm^2/eV for the T_{low} transition. Large error in determination of β is consistent with that the linear Stark shift is certainly dominated by the extremely large permanent exciton dipole. Since the polarizability is determined predominantly by the height of the quantum dots,[176] and the spatial extent of the electrons wave functions above and below Ge QDs is close to the dot vertical dimension,[124] the polarizability values turn out to be comparable with those found for III–V dots of similar height.[176, 177]

We now focus attention on the variation of the PC intensity with electric field. The amplitude of the low-energy signal increases with increasing F at low fields and saturates at bias $U \geq 5$ V. The intensity of the high-energy maximum continues to increase even at highest F. The increasing value of both PC peaks at low F can be related to an increasing rate of carrier escape with F. By applying a reverse bias, the electric field pushes the top electron towards the hole in the dot and pulls the bottom electron out from the hole. As a consequence, the electron–hole overlap and the corresponding absorption strength are increased for the T_{high} transition and reduced for the T_{low} transition. At highest F, no bound state can further exist for the bottom electron and the T_{low} transition transforms into a smooth PC tail on the low-energy side of the T_{high} signal.
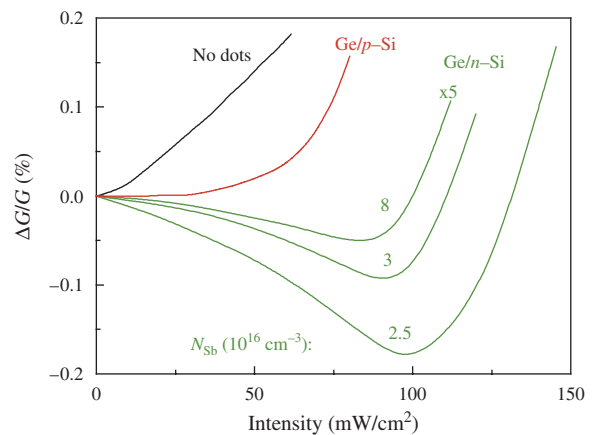
7.3. Negative Interband Photoconductivity

An important consequence of the spatial separation of electrons around Ge SAQDs caused by Coulomb repulsion between them is that a dot is able to trap more electrons than there are holes[85] (see, also, Section 3.4). Consider an *n*-type Si layer with embedded Ge dots. The dark conductivity of the system is determined by the mobile electrons thermally activated from the donor impurity states to the conduction band. Under interband optical excitation, hole

will start to accumulate in Ge SAQDs, charging them positively. As a result, potential wells for electrons will arise at both sides of the Si/Ge interface. The electrons (both equilibrium and photoexcited) become localized in the wells. The localization of equilibrium electrons will decrease the concentration of mobile carriers and reduce the conductivity of the system. Thus, the observation of negative photoconducivity in Ge/Si QDs can provide a proof of the spatial separation of electrons.

To verify experimentally this prediction, we investigated the conductivity and the concentration of free carriers in different Ge/Si SAQDs structures under illumination.[185, 186] Each sample consists of ten layers of Ge islands separated by 30 nm Si spacers. To obtain *n*- or *p*-type of the structure Sb- or B-doping was used, respectively. GaAs light-emitting diodes (LEDs) with an emission maximum as a wavelength of 0.9 μm were used as a light source. The emission density of the LEDs was modulated with a frequency of 2 kHz. The photocurrent and Hall signal were measured at the modulation frequency with the lock-in technique.

The relative change in the conductivity at $T = 77$ K of the samples with different Sb concentration as a function of the illumination power density P is depicted in Figure 62. Also shown is the photoconductovoty of the *p*-type sample and of the sample in which the layer with Ge QDs has been removed by chemical etching. The conductivity of the sample containing no dots and of the *p*-type Ge/Si structure is traditionally positive. The QD *n*-type samples exhibit negative photoresponse in the range of illumination intensities $P = 0$–100 mW cm^{-2}. Figure 63 demonstrates that the negative photoeffect is actually accompanied by decreasing the mobile carrier concentration, while the mobility is only weakly affected by illumination. At $P > 100$ mW cm^{-2}, a transition from negative to positive PC is observed. With increasing exciton occupation the self-consistent potential wells become

Fig. 62. Dependence of the relative photoconductivity on the interband illumination intensity in *n*-type Si samples with Ge SAQDs at different Sb concentration in epitaxial layer ($N_{Sb} = (2.5–8) \times 10^{16}$ cm^{-3}), in the sample containing no dots and in the *p*-type QD Ge/Si structure.
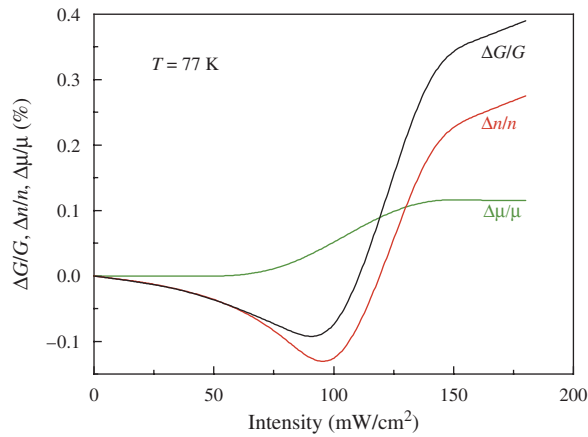
Fig. 63. Dependence of the relative photoconductivity, concentration of free electrons and mobility on the interband illumination intensity in Ge/*n*-Si heterostructure with $N_{Sb} = 3 \times 10^{16}$ cm^{-3}.

completely filled with electrons and free photogenerated carriers give rise to increasing photoconductivity.

It should be emphasized that the observed negative photoeffect is an inherent feature of the type-II quantum dots, because in type-I systems both electrons and holes are confined in the potential wells created by the conduction and valence band discontinuities independently of the charge state of SAQDs.

7.4. Depolarization Shift of the Interlevel Resonance

The motion of the electrons in a two-dimensional (2D) system is quantized in the direction z perpendicular to the plane of the layer. The z-polarized infrared radiation can be absorbed by a 2D system causing interband transitions in the well. It is well known that in a dense 2D plasma, the collective intersubband charge-density excitations (resonant screening) leads to a density-dependent blueshift of the interband resonance away from its single-particle position[187] and to a resonance line narrowing for a nonparabolic system.[188] The renormalization of the intersubband absorption energy due to collective interactions is called the "depolarization" shift.[189] In contrast to 2D systems, additional lateral confinement of carriers in quantum dots makes in-plane polarized transitions between the discrete levels possible.[91, 190]

Direct examination of the role of collective coupling for the in-plane polarized interlevel absorption of a stack of ten dense arrays of Ge/Si SAQDs has been made in Ref. [91]. The dots have a lateral size of about 15 nm and a density 3×10^{11} cm^{-2} in each layer. The interlevel absorption studied corresponds to the transition from the hole ground state to the first excited state in the dot; the states are associated with in-plane confinement and belong to the same z-subband. To provide holes for intersublevel absorption, the sample was illuminated by a halogen lamp that allowed to change the average dot occupation number from zero to about 2.5 holes per dot. The photoinduced
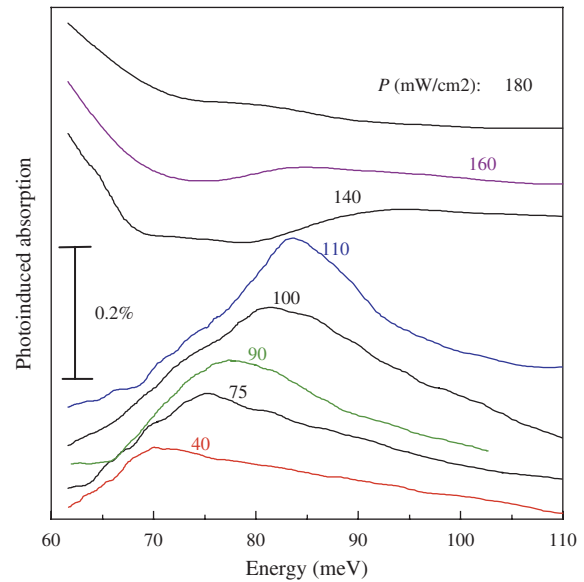
Fig. 64. The photoinduced absorption at various pump intensities. A constant offset is added for clarity. The sample consists of 10 layers of Ge dots separated by 30 nm Si barriers and was grown on a (001) oriented phosphorus doped Si substrate. The Sb-doping level of the Si barriers was 10^{16} cm^{-3}. The areal density of the dots in each layer is 3×10^{11} cm^{-2}.
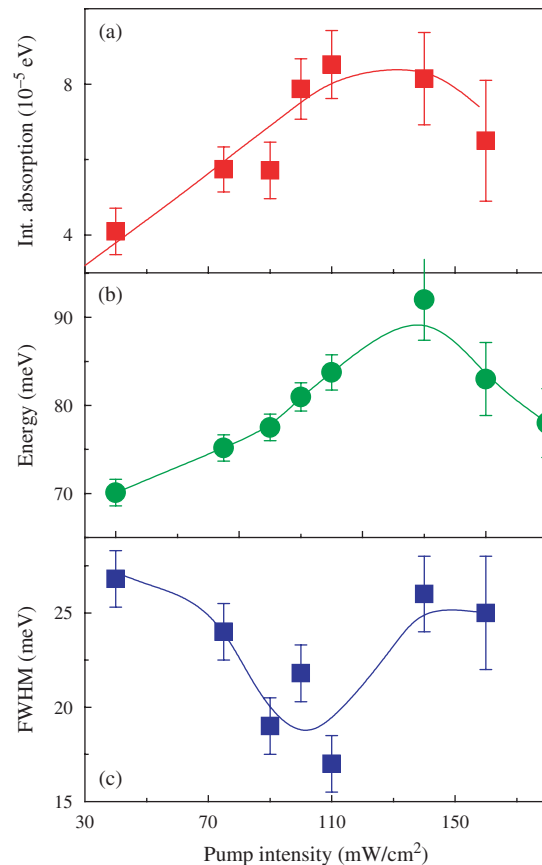
Fig. 65. Integrated absorption (a), resonance position (b), and the full width at half maximum (FWHM) (c) versus pump intensity.
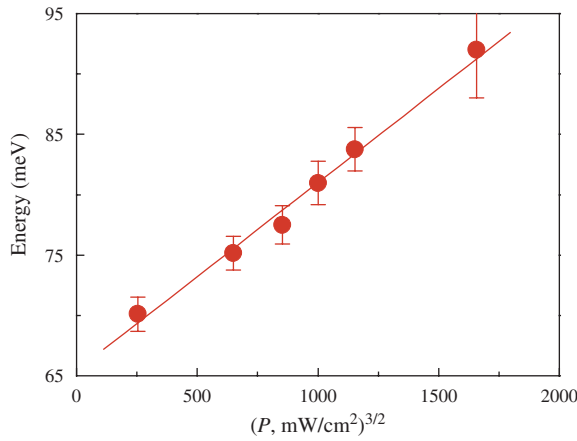
Fig. 66. The intersublevel resonance position as a function $P^{3/2}$, where P is the pump intensity.

infrared absorption spectra measured at different pump intensities P are reported in Figure 64. An absorption peak is found at 70–90 meV, in agreement with the result of tunneling spectroscopy of interlevel spacing (Section 4). The free-carrier absorption associated with carriers that are not trapped in the dots is also observed at high pump intensities as an increasing absorption towards low energy. At low intensity, the peak is strongly asymmetric that reflects the nonuniformity of the dot sizes. As the pump intensity increases, the absorption peak shifts to higher energies and becomes more symmetric, considerably reducing its linewidth (Fig. 65). All these features are a signature of the collective phenomena, here realized in a system of laterally confined states. From the magnitude of the absorption in the collective mode, the oscillator strength has been determined to be 0.95.[91]

Because the depolarization field effect is a result of dipole–dipole interaction between QDs, the energy shift of the intersublevel absorption should be propotional to $P^{3/2}$, where P is the pump intensity.[191] Figure 66 nicely demonstrates such a dependence. At large optical pump intensity, the dot-excited state becomes occupied with holes. This suppresses the depolarization effect and causes the transition energy to be shifted downward to its single-particle value.[192] Apart from the interesting issues relating to collective excitations of dense arrays of QDs, the depolarization effect gives rise to possible practical application of electric modulation in tunable infrared modulators.

8. APPLICATIONS

8.1. Quantum-Dot Metal-Oxide-Semiconductor Field-Effect Transistor

Despite the large effort to study the fundamental properties of Ge/Si SAQDs, there were only several attempts of incorporating Ge/Si islands as an active element of semiconductor devices, such as infrared photodetectors[37, 193–196] and light-emitting[197, 198] and resonant-tunneling diodes.[199]

Little work has been done on the Ge/Si quantum-dot field-effect transistors (QDFETs), which use the quantum transport through discrete energy states in zero-dimensional systems.[200] To date, most work in the field of QDFETs has concentrated on InAs/GaAs SAQDs[201–203] and on Si-based quantum dots defined by very sophisticated patterning techniques, such as electron-beam litography in combination with anisotropic etching[204–207] and selective oxidation,[208, 209] or by tunable gates.[210]

In order to rise the operation temperature of QDFETs up to 300 K, the size of QDs has to be smaller than 10 nm. This requirement considerably restrict the possibility of using the lithographic processes for fabricating ultrasmall QDs. In this way, the Ge/Si SAQDs, which are formed without additional lithography procedure and whose diameter can be achieved as small as $\sim$10 nm,[37] are more advantageous and, hence, more relevant for application in QDFETs operating at room temperature.

In Section 6.1, we demonstrated QDFET with an array of 3×10^7 Ge SAQDs embedded into the active channel of a Si MOSFET.[150] The device was fabricated on a silicon-on-insulator (SOI) substrate prepared by the separation by implanted oxygen (SIMOX) technique. The channel was a Si island of 100 μm width and 108 μm length which rests on SiO$_2$. The area of the MOSFET gate was 100 $\times$ 100 μm^2. However, clear drain current oscillations with a gate voltage due to successive loading of holes into the dots were not observed. The reasons are
(i) the leakage current across the Si layer leading to the large background varying with the voltage, and
(ii) significant broadening of the current peaks due to statistical fluctuations of the dot sizes and Coulomb potentials from randomly distributed charged QDs in the dot ensemble.

These drawbacks are eliminated in this section. First, the drain current leakage is reduced by reducing the superficial Si layer thickness in a SOI substrate. Second, the average Ge SAQDs lateral dimensions are decreased from 15 nm to 10 nm. The stronger carrier confinement in the dots provides the larger energy-level separation, resulting in a clearer resolution of the current peaks at high temperatures. Third, inhomogeneous broadening due to long-range dot size variations and random Coulomb potentials are reduced by decreasing the QDFET size from 100 μm to $\sim$1 μm and by using the gate recess configuration.[202]

The starting material was a SOI (001) substrate with a 150-nm-thick p-type superficial Si film. First, the SOI layer was thinned to 47 nm by thermal oxidation. After removing SiO$_2$, a 20-nm-thick undoped Si buffer layer was grown at 800 °C by molecular beam epitaxy. Next, the Ge self-assembled dots were grown at 300 °C with nominal thickness of 8 monolayers and subsequently embedded in 20-nm of Si. The average in-plane diameter and height of the Ge dots are 10 and 1 nm, respectively. The density of the dots is 4×10^{11} cm^{-2}. To supply holes on
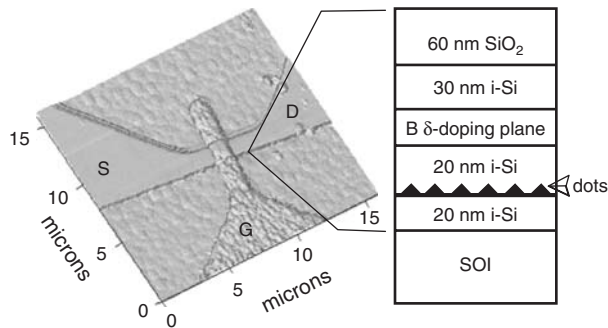
Fig. 67. Atomic force microscopy image and schematic cross section of the transistor channel. The source, drain, and the gate are labeled by S, D, and G, respectively.

the dots, a boron delta-doping (6×10^{12} cm^{-2}) Si layer inserted 20 nm above the Ge layer was grown. A 30-nm-thick undoped Si cap layer was then deposited at 500 °C. The channel was patterned by photolithography to form a Si island of 4-μm length and 1-μm width, etched down to the underlying SiO$_2$. Source and drain electrodes were made using Al evaporation and annealing at 450 °C in a N$_2$ atmosphere. A plasma-enhanced chemical-vapor deposition silicon dioxide of 60 nm thickness was deposited as the gate insulator and, finally, a Al gate of 4 μm width and 1 μm length was formed. The amount of oxide charge, estimated from the admittance measurements, was about 3×10^{10} cm^{-2}. Figure 67 shows an atomic force microscopy picture of the transistor. Several samples with designed channel widths W ranging from 2 to 1 μm are fabricated. The sidewall depletion width is determined to be 0.9 μm from measurements of drain current versus W at zero gate voltage. Assuming a uniform density of 4000 dots per μm^2 these different gate areas of the samples contain number of active dots from 400 to 4000.

The hole concentration in the boron δ-doping Si layer is sufficient to fill, after spatial transfer, all hole bound states in the Ge islands and to populate two-dimensional states in the Ge wetting layer. As a result, the channel conductance at zero gate voltage is found to show the non-activated behavior and depend only slightly on temperature.

The drain current (I_d) as a function of the gate voltage (V_g) was measured at different temperatures with the drain voltage fixed at 5 mV. Figure 68 shows the typical $I_d - V_g$ characteristics of the 1 μm gate QD transistor. When a positive bias is applied to the gate the channel is depleted and current flow between the source and drain contacts is suppressed. Above the threshold voltage $V_{th} \simeq 4$ V the deep hole states in the dots come into resonance with the Fermi energy and the current starts to oscillate (Fig. 69).

At room temperature, the current bump is clearly observable around 6 V. As the temperature decreases, four well-pronounced equidistant peaks with a gate voltage separation $\Delta V_g \simeq 1.1$ V appear after onset of the conductance. The number and relative position of the peaks are well reproducible at different cold cycles and in different
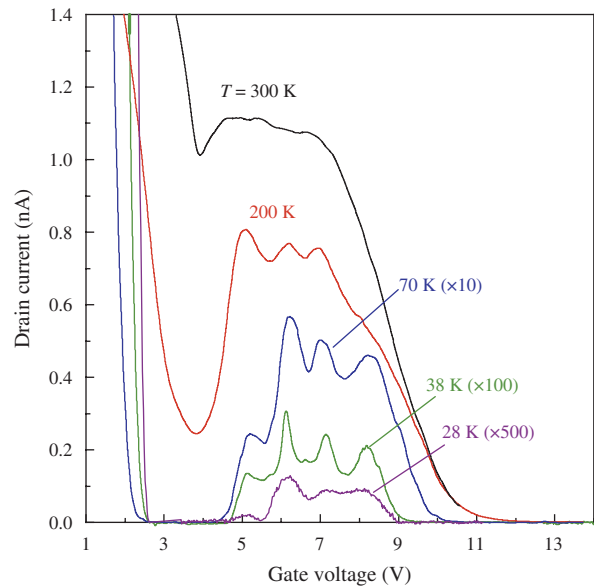
Fig. 68. Gate voltage dependence of drain current at various temperatures.

samples of similar sizes. It follows from previous investigations of the field effect, admittance and capacitance spectra in Si modulation-doped structures with similar Ge quantum dots[150, 151, 211] that when we leave the continuum and enter the tunneling regime with increasing gate bias, we would expect four equidistant current peaks (tunneling through fourfold-degenerate excited state in the Ge QDs), then a voltage (energy) gap and two additional peaks corresponding to transport through the twofold-degenerate hole ground state (Fig. 69). Since we only observe four maxima
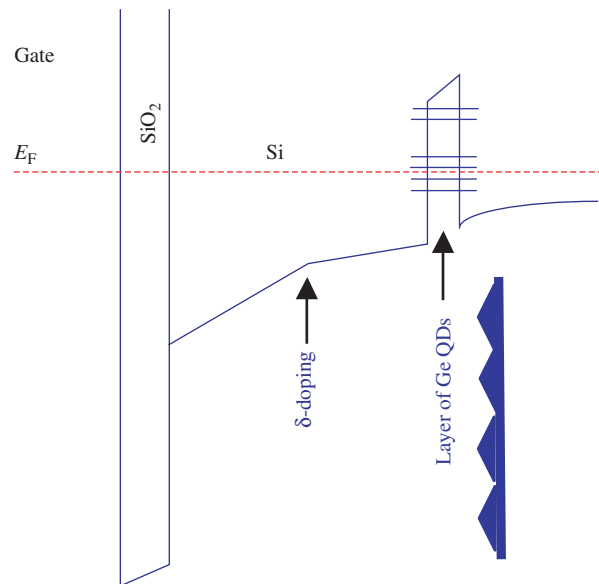
Fig. 69. Top of the valence band of the transistor for positive gate bias. The SOI substrate is not shown. The holes reside in the Ge dots. When the Fermi level is aligned with the quantum levels in the Ge dots at a certain gate voltage, holes will flow through that quantum level in the plane of Ge SAQDs.

REVIEW

right above the transport continuum, we relate these peaks to hole transport through the excited state of Ge/Si SAQDs. A very similar fine-structure consistent with four maxima, separated by the Coulomb blockade energy E_C, has been observed recently by Schmidt et al.[203] in InAs/GaAs QDFETs. We may ask why we do not observe current maxima associated with a filling of the hole ground state. Due to confinement and Coulomb effect, the energy difference between loading the second hole into the ground state and the first hole into the excited state of the 8 ML Ge SAQDs is approximately 200 meV (Ref. [151]). Simple estimates using the gate modulation coefficient (determined below) yield that filling of the ground state is expected to be at $V_g \approx 16$ V, but, in this region, large leakage current through the gate insulator prevents measurements of I_d–V_g characteristics.

The charging energy (E_C) of the dots can be determined by using $E_C = \eta e \Delta V_g$, where the gate modulation coefficient η relates the gate voltage to the hole energy inside the dots. This coefficient can be calculated from the temperature dependence of the full width at half maximum (FWHM) of the current peaks, which, for a single dot showing Coulomb blockade oscillations, should be broadening with T as $3.5 k_B T/(\eta e)$ (Ref. [212]). By measuring the FWHM averaged over four peaks as a function of temperature (Fig. 70), we obtain $\eta = (3.9 \pm 0.3) \times 10^{-2}$, with a residual FWHM $V_0 = 0.49 \pm 0.05$ V which is a result of statistical fluctuations in the dot ensemble. On the basis of this calculation, the estimated charging energy is 43 ± 3 meV.

In Figure 70, we depict the temperature dependence of the current maxima. A clear thermally enhanced transport through the dots with the activation energy $E_a = 21 \pm 3$ meV is evident. Several scenarios could lead to such
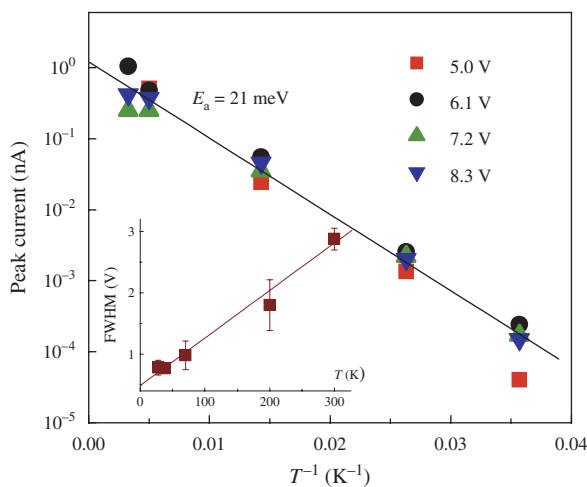
a behavior, such as thermal activation of holes from the dots over the barriers[213] and hole tunneling between neighboring dots.[214] In a latter case, the activation energy is a typical disorder energy in the system, which comes from dispersion of the dot sizes and potential fluctuations caused by random distribution of the charged dots and interface states. Because the experimental value E_a is the same for all peaks (i.e., it does not depend on the effective barrier height), the conduction mechanism is attributed to the nearest-neighbor hopping of holes between the dots. With scanning the gate voltage, the Fermi level moves across the zero-dimensional density of states. The maximum current occurs when the given hole level in the dots is half-filled because this maximizes the product of possible initial and final states for tunneling process and avoids increasing the energy of the system due to appearance of extra charge in a final dot.

The disorder energy, E_d, in ensemble of the dots can be found from residual FWHM using $E_d = \eta e V_0$. For $V_0 = 0.49 \pm 0.05$ V and $\eta = (3.9 \pm 0.3) \times 10^{-2}$, one obtain $E_d = 19 \pm 3$ meV, which is consistent with the experimental value of activation energy observed in Figure 70.

8.2. Quantum Dot Photodetectors for Near- and Midinfrared Operation

The potential advantages of the quantum dots infrared photodetectors (QDIPs) as compared with two-dimensional systems are as follows:

• Increased sensitivity to normally incident radiation as a result of breaking of the polarization selection rules, so eliminating the need for reflectors, gratings, or optocouplers.

• Expected large photoelectric gain associated with a reduced capture probability of photoexcited carriers due to suppression of electron–phonon scattering.

• Small thermal generation rate, resulted from zero-dimensional character of the electronic spectrum that renders a much improved signal-to-noise ratio.

• Possibility of the narrow-band detection due to discreteness of the density of states.

Furthermore, because the spatial extent of the electron or carrier wavefunction in QDs is in the order of 10 nm or more, the dipole matrix element for the intersubband transitions can be large,[215] which is not the case for natural deep impurities in semiconductors.

To provide a high performance of QDIPs, the photosensitive region of detectors should consist of a dense array of QDs.[4] In this way, self-assembled Ge/Si QDs are more advantageous and hence more relevant for application in QDIPs, in which the surface density of the dots can be achieved as high as 10^{11}–10^{12} cm^{-2} by choosing appropriate growth conditions.

The concept of QDIP using intersubband transitions was proposed and analyzed theoretically by Ryzhii et al.[216–221]

Fig. 70. Temperature dependence of the current maxima at different gate voltages. Inset: Temperature dependence of the average FWHM of four current maxima with a linear fit to the data. To obtain the FWHM of each peak, the observed current oscillations were decomposed into four Gaussians.
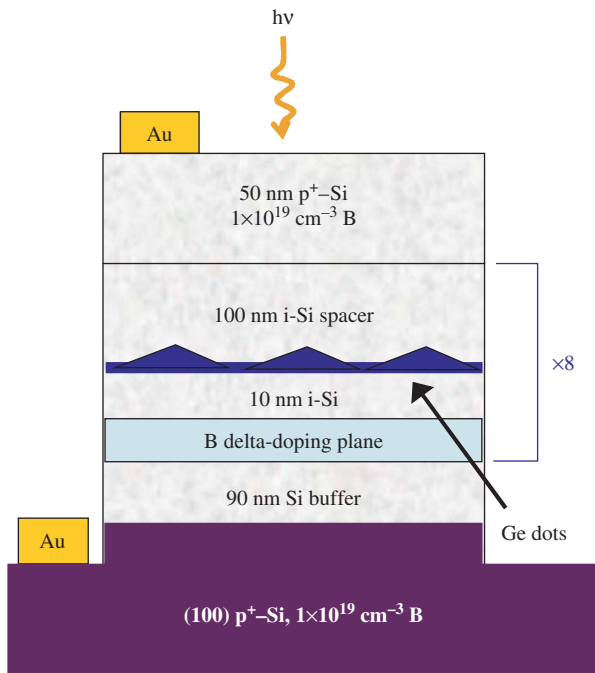
Fig. 71. Schematic of the Ge/Si phototransistor structure.

The "classical" Ge/Si QDIP with vertical photocurrent consists of a p^+–p–p^+ silicon structure with a planar array of Ge quantum dots embedded in the undoped or lightly doped with boron p-Si region. The array of QDs plays the role of the QDIP active element (the phototransistor base). Heavily doped p^+-Si regions serve as the emitter and collector of the phototransistor. An example of practical realization of Ge/Si phototransistor is shown in Figure 71.[196]

The holes captured in the Ge QDs form a sheet charge distributed in the QD plane. The current flowing from emitter to collector is limited by this space charge (Fig. 72). The holes, photoexcited from the ground to excited states in the dots (bound-to-bound transitions (Fig. 72(a)) or from bound to continuum states (Fig. 72(b)), change the space charge density in the base
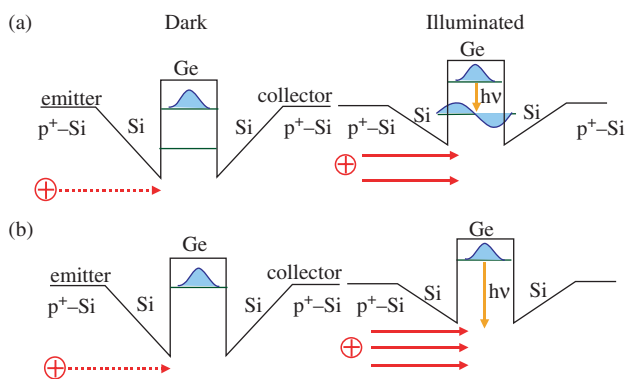

Fig. 72. Valence band profile in Ge/Si QDIPs with and without illumination with light.
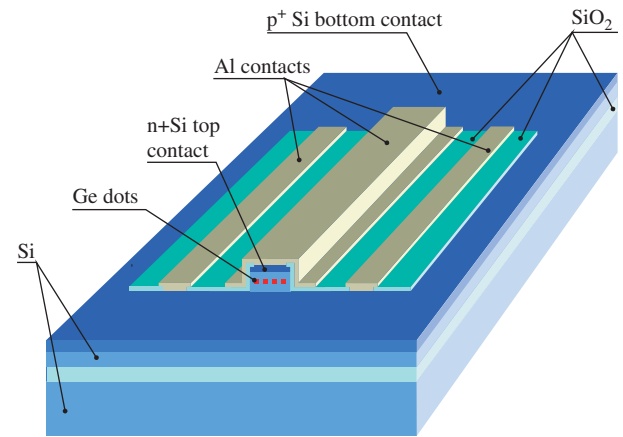
Fig. 73. Schematic layout of waveguide near-infrared photodetector on a silicon-on-insulator substrate.

region, that results in an increase of the emitter current. In a former case, a change of the charge density in the QD plane is originated from the different wavefunction extent of holes in different quantum states. Additional contributions to the photocurrent could arise from appearance of the mobile photoholes in the Si valence band due to thermal ionization of the excited state or due to direct photoexcitation.

Apart from the conventional p^+–p–p^+ structure of Ge/Si QD phototransistors, p^+–p–n^+ and n^+–p–n^+ structures were used for mid-[37] and near-infrared[36, 193, 222–224] detection. Also lateral Ge/Si QDIPs with detectivity of 1×10^{11} cm$\sqrt{\text{Hz}}$/W at $T = 20$ K have been realized and demonstrated their high potential for efficient normal incidence mid-infrared operation.[225–227]

The integration of Si/Ge heterostructures on a Si chip and their compatibility with Si-based electronic circuitry presents a high potential for designing low-cost optoelectronic modules. An example of near infrared Ge/Si p–i–n photodetector operating at the 1.3 μm and 1.55 μm telecommunication wavelengths is shown in Figure 73. To increase the interaction length between the light and the QD layers and to provide the intrachip interconnections, a vertical stacking of 36 layers of coherent Ge nanoislands was inserted into a waveguide obtained with a SOI structure. The sample was processed into ridge waveguide. Devices with lengths going from $L = 0.1$ to 5 mm were fabricated.[224] The room-temperature quantum efficiency of a 4 mm device versus reverse bias U_b is shown in Figure 74. The light is coupled through the edge of the detector. The maximum external quantum efficiency achieved is 16% for $\lambda = 1.55$ μm and 21% for $\lambda = 1.3$ μm at $L > 3$ mm and $U_b > 3$ V.

To the best of our knowledge, the first observation of midinfrared photoconductivity in Ge QDs has been reported by Yakimov et al. in 1999.[37] The QDIP under investigation was a p^+–p–n^+ silicon diode embedded with a single layer of pyramidal Ge SAQDs. The average size of
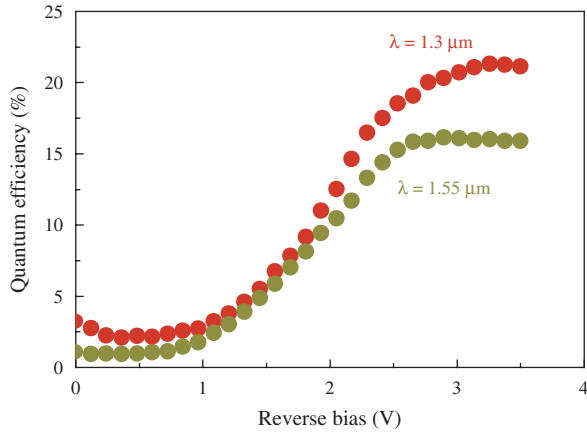
Fig. 74. Quantum efficiency of a 4 mm waveguide photodetector as a function of reverse bias.

the dot base length is 15 nm, the height is ≈ 1.5 nm. As the heterostructure was growth at low temperature (Ge layer was grown at 300 °C and covered with Si at 500 °C), the segregation and interdiffusion effects are negligible and Ge islands contain no silicon atoms. The large areal density of Ge QDs (3×10^{11} cm^{-3}) realized the high absorption coefficient.

Figure 75 depicts normal incidence PC spectral response as a function of reverse bias taken at $T = 300$ K. There are apparent two PC peaks below the silicon interband absorption edge which are changed with the applied voltage in a different way. Because the energy difference between the ground state of the dot and the Si valence band edge is about 400 meV,[41] the midinfrared absorption around 3 μm is attributed to the intraband hole bound-to-continuum transition (Fig. 76, top panel). The variation of bias voltage moves the Fermi level with respect to the quantum levels in the dot layer. The hole population in the dots decreases as the reverse bias U_b increases. At $U_b = 1.4$ V,
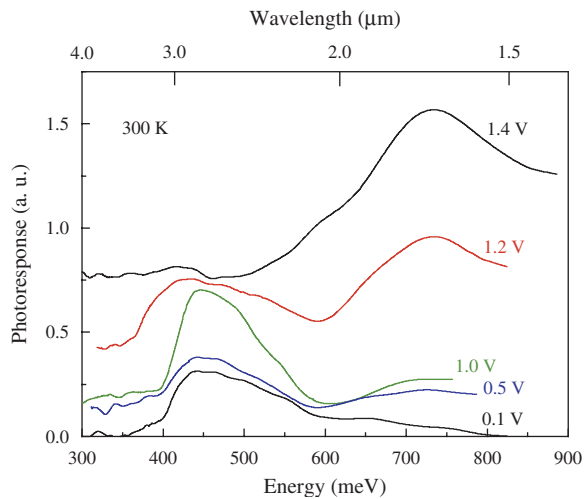
Fig. 75. Photocurrent spectra of Ge/Si p^+-p-n^+ QDIP as a function of reverse bias. The curves have been offset vertically for clarity.
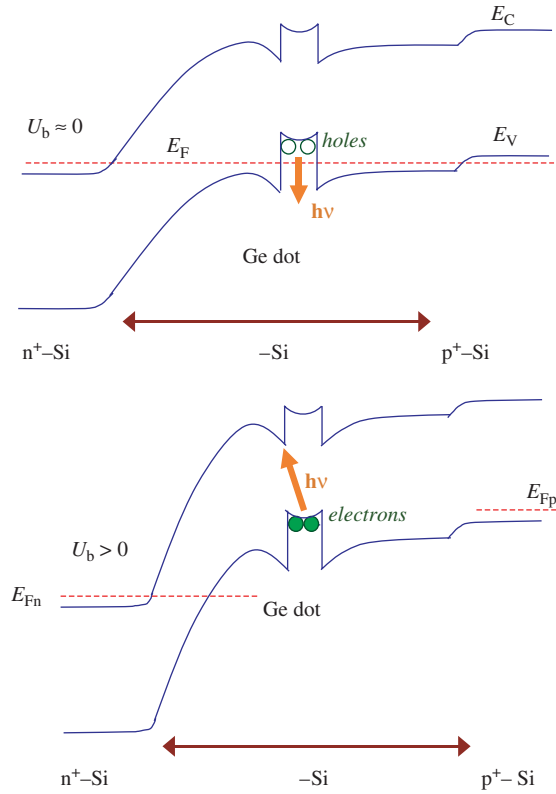
Fig. 76. Schematic diagram of photoresponse mechanisms of Ge/Si p^+-p-n^+ QDIP at low and at large reverse bias.

holes escape from the dots and 3 μm transition becomes forbidden. The 1.7 μm PC maximum shows the opposite behavior with applied voltage. Its appearance is accompanied by suppression of the 3 μm absorption. This observation establishes direct correlation between two absorptions and favors the near-infrared (1.7 μm) feature is caused by an interband indirect electronic transition from the highest valence band states in the Ge QDs and the Si conduction band (Fig. 76, bottom panel). In this case, the transition energy should be equal to the energy difference between the silicon band gap (1.126 eV at 293 K) and the hole ground energy of the dot (≈ 400 meV, estimated as the cut on energy of the 3 μm absorption). By these values the transition energy is determined to be about 730 meV (1.7 μm wavelength), which is consistent with the experimental result (Fig. 75). The device described can be implemented to form two-color detector arrays whose spectral response can be finely tuned by an external bias.

The photoresponse of Ge/Si p^+-p-p^+ QDIPs associated with bound-to-continuum intraband transitions was studied by Miesner et al.,[194, 226] Rappaport et al.,[195] and Boucaud et al.[228] The active region of samples consists of 10 periods of Ge dots separated by Si spacers. The mean dot base length is 75–100 nm and the average dot height is around 7 nm.[194, 195, 228] Typical dot areal density ranges between 10^9 and 4.4×10^9 cm^{-2}. A p-type doping with

boron was used to provide from 2 (Ref. [195]) to about a 100 (Ref. [194]) holes per each Ge dot.

For samples with Ge layer grown at 500 °C, the PC maximum was observed at ∼324 meV with peak responsivity of 5 mA/W at 20 K.[226] Because the sample was grown at a sufficiently high substrate temperature, GeSi alloy with a lower valence band offset is formed in the Ge regions. This is why the bound-to-continuum transition energy (300 meV) is smaller than that observed in Figure 75 (400 meV) when the islands consist of pure Ge. The lateral structures with similar QDs have responsivity up to 10 mA/W and detectivity of about 1×10^{11} cm Hz$^{1/2}$/W at $T = 20$ K in normal incidence geometry.[227] When the growth temperature is raised up to 600 °C, the photocurrent maximum is further red-shifted downward to ≈ 100 meV.[195, 228] These results demonstrate that by appropriate choice of the growth conditions it is possible to fabricate the effective Ge/Si QDIPs with desirable spectral range of photoresponse.

The photoconductivity associated with bound-to bound transitions was studied in a vertical p^+-p-p^+ phototransistor with eight Ge QD layers grown on a p^+-Si substrate (Fig. 71).[196] The thickness of Si regions separated the Ge layers was 110 nm. Within a 10-nm distance from each Ge layer, Si was δ-doped with boron at a layer concentration of 6×10^{11} cm^{-2}, which ensured nearly complete filling of the islands ground state with holes (two holes of opposite spins per each dot). An effective differential resistivity of the device at zero voltage of about 10^6 Ω cm is larger than that of intrinsic silicon, 2.3×10^5 Ω cm. This means that

(i) there is band bending around the dot layers due to formation of depletion regions and

(ii) carrier are localized deep in the dots, not participating in conduction.

In this situation, the dominant transport mechanism at sufficiently large voltage is associated with hole injection from the contact into the Si valence band. The temperature dependence of the dark current within the ohmic region of the current–voltage characteristic was found to follow the activation law with an activation energy close to the energy difference between the ground state of the dots and the Si valence band edge (400 meV).[196]

Figure 77 shows the room-temperature photoresponse spectra measured at normal incident radiation conditions. The curves exhibit two distinct peaks: the low-energy peak corresponds to the hole transition from the ground to the first excited state, and the high-energy peak is apparently associated with the transition to the second excited state. Combining responsivity data with the results of noise and dark current measurements, and using the following expressions

$$i_n = \sqrt{4eI_d g \Delta f}$$

$$R = \left(\frac{e}{h\nu}\right)\eta g$$
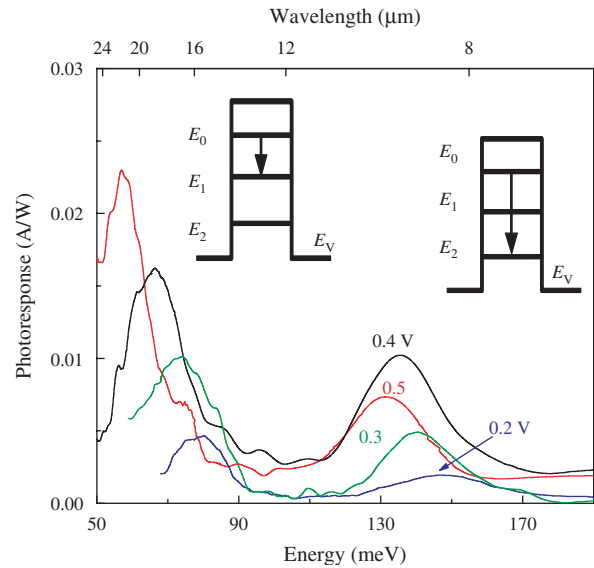
Fig. 77. Photoconductive spectral response of the Ge/Si QDIP at various bias voltages. The layer of Ge SAQDs was grown at a substrate temperature of $T_s = 300$ °C. The dots have a typical base length of 15 nm and height of 1.5 nm. The density of the dot is 3×10^{11} cm^{-2}. The measurements have been made at 300 K. E_0 is the energy of the hole ground state in the dots, and E_1 and E_2 are the energies of the first and second excited states of holes, respectively.

where i_n is the dark current noise, I_d is the dark current, g is the photoelectroc gain, Δf is the bandwidth, $h\nu$ is the photon energy, η is the responsive quantum efficiency, the maximum values of photoelectric gain and detector quantum efficiency were determined to be 4 and 0.1%, respectively.

9. CONCLUDING REMARKS

The development of new products and services depends strongly on the capability to exploit in a more advanced manner the physical and chemical properties of materials. Thus, the investigation of matter and its control at the nanoscale presents a huge potential that can benefit society as a whole and in the framework of sustainable development. It could also greatly increase industrial competitiveness. Research and technology on the nanolevel represent a great intellectual and scientific challenge where the traditional scientific disciplines converge. New interdisciplinary approaches and curricula need to be developed. To succeed in the challenging world of nanotechnology, research excellence is, however, not enough. Successful strategies for companies and research organizations include industrial innovation and attention to environmental and social issues. New manufacturing tools and appropriate standards are also required as well as a novel entrepreneurial attitude. Considerable resources and efforts are required to meet these challenges in appositive and timely manner. Furthermore, a careful analysis of the current situation has to be carried out. Future initiatives will greatly benefit from

REVIEW

coordination and focusing in order to achieve the maximum impact on industry, to improve the quality of life of the citizens and enable the new discoveries to generate wealth and employment.

References and Notes

1. S. M. Reimann and M. Manninen, *Rev. Mod. Phys.* 74, 1283 (**2002**).
2. W. G. van der Wiel, S. De Franceschi, J. M. Elzerman, T. Fujisawa, S. Tarucha, and L. P. Kouwenhoven, *Rev. Mod. Phys.* 75, 1 (**2003**).
3. D. Bimberg, M. Grundmann, and N. N. Ledentsov, Quantum Dot Heterostructures, Wiley, Chichester (**1998**).
4. A. I. Yakimov and A. V. Dvurechenskii, Selected Topics in Electronics and Systems Series, edited by V. Ryzhii, World Scientific, Singapore (**2003**), Vol. 27, p. 281.
5. N. S. Beattie, B. E. Kardynał, A. J. Shields, I. Farrer, D. A. Ritchie, and M. Pepper, *Phys. Rev. B* 70, 081304 (**2004**).
6. D. Loss and D. P. DiVincenzo, *Phys. Rev. A* 57, 120 (**1998**).
7. A. R. Woll, P. Rugheimer, and M. G. Lagally, *Int. J. High Speed Electronics and Systems* 12, 45 (**2002**).
8. K. Brunner, *Rep. Prog. Phys.* 65, 27 (**2002**).
9. I. Berbezier, A. Ronda, and A. Portavoce, *J. Phys.: Condens. Matter* 14, 8283 (**2002**).
10. C. Teichert, *Phys. Rep.* 365, 335 (**2002**).
11. J. Stangl, V. Holý, and G. Bauer, *Rev. Mod. Phys.* 76, 725 (**2004**).
12. J.-M. Baribeau, X. Wu, N. L. Rowel, and D. J. Lockwood, *J. Phys.: Condens. Matter* 18, R139 (**2006**).
13. D. J. Eaglesham and M. Cerullo, *Phys. Rev. Lett.* 64, 1943 (**1990**).
14. J. J. Lander and J. Morrison, *J. Appl. Phys.* 33, 2098 (**1962**).
15. A. A. Shklyaev, M. Shibata, and M. Ichikawa, *Phys. Rev. B* 62, 1540 (**2000**).
16. A. Barski, M. Derivaz, J. L. Rouviere, and D. Buttard, *Appl. Phys. Lett.* 77, 3541 (**2000**).
17. P. Muller and R. Kern, *J. Cryst. Growth* 193, 257 (**1998**).
18. A. A. Chernov, Handbook of Crystal Growth, edited by D. T. J. Hurle, North-Holland Elsevier, Amsterdam (**1994**), Vol. 3, p. 1086.
19. F. Liu and M. G. Lagally, *Phys. Rev. Lett.* 76, 3156 (**1996**).
20. R. J. Asaro and W. A. Tiller, *Metall. Trans.* 3, 789 (**1972**).
21. M. A. Grinfeld, *Sov. Phys. Dokl.* 31, 831 (**1986**).
22. S. A. Kukushkin and A. V. Osipov, *Physics-Uspekhi* 41, 983 (**1998**).
23. N. C. Bartelt, W. Theis, and R. M. Tromp, *Phys. Rev. B* 54, 11741 (**1996**).
24. I. M. Lifshitz and V. V. Slyozov, *J. Phys. Chem. Solids* 19, 35 (**1961**).
25. M. Kastner and B. Voigtlander, *Phys. Rev. Lett.* 82, 2745 (**1999**).
26. Y.-W. Mo, D. E. Savage, B. S. Swartzentruber, and M. G. Lagally, *Phys. Rev. Lett.* 65, 1020 (**1990**).
27. J. A. Floro, E. Chason, L. B. Freund, R. D. Twesten, R. Q. Hwang, and G. A. Lucadamo, *Phys. Rev. B* 59, 1990 (**1999**).
28. V. A. Markov, A. I. Nikiforov, and O. P. Pchelyakov, *J. Cryst. Growth* 175/176, 736 (**1997**).

29. Z. Jiang, H. Zhu, F. Lu, J. Qin, D. Huang, X. Wang, C. Hu, Y. Chen, Z. Zhu, and T. Yao, *Thin Solid Films* 321, 60 (**1998**).
30. V. A. Markov, O. P. Pchelyakov, L. V. Sokolov, S. I. Stenin, and S. Stoyanov, *Surf. Sci.* 250, 229 (**1991**).
31. O. P. Pchelyakov, I. G. Neisvestnyi, and Z. Sh. Yanovitskaya, *Phys. Low- Dim. Struct.* 10/11, 389 (**1995**).
32. H. Omi and T. Ogino, *Appl. Surf. Sci.* 130–132, 781 (**1998**).
33. G. Springholz, V. Holy, M. Pinczolits, and G. Bauer, *Science* 282, 734 (**1998**).
34. Y. W. Zhang, S. J. Xu, and C.-H. Chiu, *Appl. Phys. Lett.* 74, 1809 (**1999**).
35. O. P. Pchelyakov, Yu B. Bolkhovityanov, A. V. Dvurechenskii, A. I. Nikiforov, A. I. Yakimov, and B. Voigtlaender, *Thin Solid Films* 367, 75 (**2000**).
36. G. Abstreiter, P. Schittenhelm, C. Engel, E. Silveira, A. Zrenner, D. Meertens, and W. Jäger, *Semicond. Sci. Technol.* 11, 1521 (**1996**).
37. A. I. Yakimov, A. V. Dvurechenskii, Yu Yu Proskuryakov, A. I. Nikiforov, O. P. Pchelyakov, S. A. Teys, and A. K. Gutakovskii, *Appl. Phys. Lett.* 75, 1413 (**1999**).
38. C. S. Peng, Q. Huang, W. Q. Cheng, J. M. Zhou, Y. H. Zhang, T. T. Sheng, and C. H. Tung, *Appl. Phys. Lett.* 72, 2541 (**1998**).
39. A. I. Nikiforov, V. V. Ulyanov, O. P. Pchelyakov, S. A. Teys, and A. K. Gutakovskii, *Physics of the Solid State* 46, 77 (**2004**).
40. A. I. Nikiforov, V. V. Ulyanov, A. G. Milekhin, O. P. Pchelyakov, S. A. Teys, S. Schulze, and D. R. T. Zahn, *Phys. Stat. Sol. (c)* 1, 360 (**2004**).
41. A. I. Nikiforov, V. A. Cherepanov, O. P. Pchelyakov, A. V. Dvurechenskii, and A. I. Yakimov, *Thin Solid Films* 380, 158 (**2000**).
42. A. I. Nikiforov, V. A. Cherepanov, and O. P. Pchelyakov, *Semiconductors* 35, 988 (**2001**).
43. J. Drucker and S. Chaparro, *Appl. Phys. Lett.* 71, 614 (**1997**).
44. U. Denker, M. Stoffel, O. G. Schmidt, and H. Sigg, *Appl. Phys. Lett.* 82, 454 (**2003**).
45. S. A. Chaparro, Y. Zhang, J. Drucker, D. Chandrasekhar, and D. J. Smith, *J. Appl. Phys.* 87, 2245 (**2000**).
46. J. Tersoff, C. Teichert, and M. G. Lagally, *Phys. Rev. Lett.* 76, 1675 (**1996**).
47. E. Mateeva, P. Sutter, J. C. Bean, and M. G. Lagally, *Appl. Phys. Lett.* 71, 3233 (**1997**).
48. V. L. Thanh, V. Yam, P. Boucaud, Y. Zheng, and D. Bouchier, *Thin Solid Films* 69, 43 (**2000**).
49. C. S. Peng, Q. Huang, W. Q. Cheng, J. M. Zhou, Y. H. Zhang, T. T. Sheng, and C. H. Tung, *Phys. Rev. B* 57, 8805 (**1998**).
50. A. Portavoce, F. Volpi, A. Ronda, P. Gas, and I. Berbezier, *Thin Solid Films* 380, 164 (**2000**).
51. J. Zhu, K. Brunner, and G. Abstreiter, *Appl. Phys. Lett.* 73, 620 (**1998**).
52. A. I. Nikiforov, V. V. Ulyanov, O. P. Pchelyakov, S. A. Tiis, and A. K. Gutakovskii, *Physics of the Solid State* 47, 67 (**2005**).
53. A. V. Dvurechenskii, J. V. Smagina, V. A. Zinovyev, S. A. Teys, A. K. Gutakovskii, and R. Groetzschel, *Int. J. Nanosci.* 3, 19 (**2004**).
54. B. Cho, T. Schwarz-Selinger, K. Ohmori, D. Cahill, and J. E. Greene, *Phys. Rev. B* 66, 195407 (**2002**).
55. E. P. McDaniel, Jiang Qian, P. A. Crozier, J. Drucker, and D. J. Smith, *Appl. Phys. Lett.* 87, 223101 (**2005**).
56. Y. Q. Wu, F. H. Li, J. Cui, J. H. Lin, R. Wu, J. Qin, C. Y. Zhu, Y. L. Fan, X. J. Yang, and Z. M. Jiang, *Appl. Phys. Lett.* 87, 223116 (**2005**).
57. A. I. Yakimov, A. I. Nikiforov, A. V. Dvurechenskii, V. V. Ulyanov, V. A. Volodin, and R. Groetzschel, *Nanotechnology* 17, 4743 (**2006**).
58. G. Katsaros, G. Costantini, M. Stoffel, R. Esteban, A. M. Bittner, A. Rastelli, U. Denker, O. G. Schmidt, and K. Kern, *Phys. Rev. B* 72, 195320 (**2005**).

59. U. Denker, M. Stoffel, and O. G. Schmidt, *Phys. Rev. Lett.* 90, 196102 (**2003**).

60. F. Ratto, F. Rosei, A. Locatelli, S. Cherifi, S. Fontana, S. Heyn, P.-D. Szkutnik, A. Sgarlata, M. De Crescenzi, and N. Motta, *J. Appl. Phys.* 97, 043516 (**2005**).

61. S. A. Chaparro, J. Drucker, Y. Zhang, D. Chandrasekhar, M. R. McCartney, and D. J. Smith, *Phys. Rev. Lett.* 83, 1199 (**1999**).

62. X. Z. Liao, J. Zou, D. J. Cockayne, J. Qin, Z. M. Jiang, X. Wang, and R. Leon, *Phys. Rev. B* 60, 15605 (**1999**).

63. M. Floyd, Y. Zhang, K. P. Driver, J. Drucker, P. A. Crozier, and D. J. Smith, *Appl. Phys. Lett.* 82, 1473 (**2003**).

64. V. A. Volodin, M. D. Efremov, A. S. Deryabin, and L. V. Sokolov, *Semiconductors* 40, 1349 (**2006**).

65. S. H. Kwok, P. Y. Yu, C. H. Tung, Y. H. Zhang, C. S. Li, C. S. Peng, and J. M. Zhou, *Phys. Rev. B* 59, 4980 (**1999**).

66. M. M. Rieger and P. Vogl, *Phys. Rev. B* 48, 14276 (**1993**).

67. T. Meyer, M. Klemenc, and H. Von Kanel, *Phys. Rev. B* 60, R8493 (**1999**).

68. O. G. Schmidt, K. Eberl, and Y. Rau, *Phys. Rev. B* 62, 16715 (**2000**).

69. P. N. Keating, *Phys. Rev.* 145, 637 (**1966**).

70. R. Martin, *Phys. Rev. B* 1, 4005 (**1970**).

71. M. A. Cusack, P. R. Briddon, and M. Jaros, *Phys. Rev. B* 54, R2300 (**1996**).

72. C. Pryor, J. Kim, L. W. Wang, A. J. Williamson, and A. Zunger, *J. Appl. Phys.* 83, 2548 (**1998**).

73. L. W. Wang, J. Kim, and A. Zunger, *Phys. Rev. B* 59, 5678 (**1999**).

74. A. V. Nenashev and A. V. Dvurechenskii, *JETP* 91, 497 (**2000**).

75. Y. Kikuchi, H. Sugii, and K. Shintani, *J. Appl. Phys.* 89, 1191 (**2001**).

76. M. Grundmann, O. Stier, and D. Bimberg, *Phys. Rev. B* 52, 11969 (**1995**).

77. T. Benabbas, P. Francois, Y. Androussi, and A. Lefebvre, *J. Appl. Phys.* 80, 2763 (**1996**).

78. T. Benabbas, Y. Androussi, and A. Lefebvre, *J. Appl. Phys.* 86, 1945 (**1999**).

79. T. Saito, T. Nakaoka, T. Katitsuka, Y. Yoshikuni, and Y. Arakawa, *Physica E* 26, 217 (**2005**).

80. M. A. Cusack, P. R. Briddon, and M. Jaros, *Phys. Rev. B* 56, 4047 (**1997**).

81. H. Jiang and J. Singh, *Phys. Rev. B* 56, 4696 (**1997**).

82. O. Stier, M. Grundmann, and D. Bimberg, *Phys. Rev. B* 59, 5688 (**1999**).

83. T. Saito, J. N. Schulman, and Y. Arakawa, *Phys. Rev. B* 57, 13016 (**1998**).

84. Y. M. Niquet, G. Allan, C. Delerue, and M. Lannoo, *Appl. Phys. Lett.* 77, 1182 (**2000**).

85. A. V. Dvurechenskii, A. V. Nenashev, and A. I. Yakimov, *Nanotechnology* 13, 75 (**2002**).

86. D. J. Chadi and M. L. Cohen, *Phys. Status Solidi b* 68, 405 (**1975**).

87. J. C. Slater and G. F. Koster, *Phys. Rev.* 94, 1498 (**1954**).

88. D. J. Chadi, *Phys. Rev. B* 16, 790 (**1977**).

89. J.-M. Jancu, R. Scholz, F. Beltram, and F. Bassani, *Phys. Rev. B* 57, 6493 (**1998**).

90. F. B. Pedersen and Y.-C. Chang, *Phys. Rev. B* 53, 1507 (**1996**).

91. A. I. Yakimov, A. V. Dvurechenskii, N. P. Stepina, and A. I. Nikiforov, *Phys. Rev. B* 62, 9939 (**2000**).

92. L. P. Kouwenhoven, C. M. Marcus, P. L. McEuen, S. Tarucha, R. M. Westervelt, and N. S. Wingreen, Mesoscopic Electron Transport, edited by L. L. Sohn, L. P. Kouwenhoven, and G. Schön, NATO ASI series E, Kluwer (**1997**), Vol. 345, p. 105.

93. L. P. Kouwenhoven, D. G. Austing, and S. Tarucha, *Rep. Progr. Phys.* 64, 701 (**2001**).

94. S. Tarucha, D. G. Austing, T. Honda, R. J. van der Hage, and L. P. Kouwenhoven, *Phys. Rev. Lett.* 77, 3613 (**1996**).

95. L. P. Kouwenhoven, T. H. Oosterkamp, M. W. S. Danoesastro, M. Eto, D. G. Austing, T. Honda, and S. Tarucha, *Science* 278, 1788 (**1997**).

96. S. Sasaki, De Franceschi, J. M. Elzerman, W. G. van der Wiel, M. Eto, S. Tarucha, and L. P. Kouwenhoven, *Nature* 405, 764 (**2000**).

97. G. Burkard, D. Loss, and D. P. DiVincenzo, *Phys. Rev. B* 59, 2070 (**1999**).

98. P. Recher, E. V. Sukhorukov, and D. Loss, *Phys. Rev. Lett.* 85, 1962 (**2000**).

99. M. Bayer, V. B. Timofeev, T. Gutbrod, A. Forchel, R. Steffen, and J. Oshinovo, *Phys. Rev. B* 52, R11623 (**1995**).

100. V. K. Kalevich, B. P. Zakharchenya, and O. M. Fedorova, *Phys. Solid State* 37, 154 (**1995**).

101. E. L. Ivchenko and A. A. Kiselev, *Sov. Phys. Semicond.* 26, 827 (**1992**).

102. A. A. Kiselev, E. L. Ivchenko, and U. Rössler, *Phys. Rev. B* 58, 16353 (**1998**).

103. A. A. Kiselev and L. V. Moiseev, *Phys. Solid State* 38, 866 (**1996**).

104. X. Marie, T. Amand, P. Le Jeune, M. Paillard, P. Renucci, L. E. Golub, V. D. Dymnikov, and E. L. Ivchenko, *Phys. Rev. B* 60, 5811 (**1999**).

105. A. A. Kiselev, K. W. Kim, and E. Yablonovitch, *Phys. Rev. B* 64, 125303 (**2001**).

106. A. V. Nenashev, A. V. Dvurechenskii, and A. F. Zinovieva, *Phys. Rev. B* 67, 205301 (**2001**).

107. G. L. Bir and G. E. Pikus, Symmetry and Strain-Induced Effects in Semiconductors, Wiley, New York (**1974**).

108. A. Abragam and B. Bleaney, Electron Paramagnetic Resonance of Transition Ions. Clarendon Press, Oxford (**1970**).

109. L. D. Landau and E. M. Lifshits, Quantum Mechanics, Nauka, Moscow (**1989**).

110. C. G. Van de Walle, *Phys. Rev. B* 39, 1871 (**1989**).

111. J. C. Hensel and K. Suzuki, *Phys. Rev. Lett.* 22, 838 (**1969**).

112. R. L. Aggarwal, *Phys. Rev. B* 2, 446 (**1970**).

113. R. Winkler, M. Merkler, T. Darnhofer, and U. Rössler, *Phys. Rev. B* 53, 10858 (**1996**).

114. P. Lawaetz, *Phys. Rev. B* 4, 3460 (**1971**).

115. G. Theodorou, P. C. Kelires, and C. Tserbak, *Phys. Rev. B* 50, 18355 (**1994**).

116. J. A. Van Vechten, *Phys. Rev.* 182, 891 (**1969**).

117. V. F. Gantmakher and Y. B. Levinson, Carrier Scattering in Metals and Semiconductors, North Holland, Amsterdam (**1987**).

118. S. A. Altshuler and B. M. Kozyrev, Electron Paramagnetic Resonance, Nauka, Moscow (**1961**).

119. M. Bayer, A. Kuther, A. Forchel, A. Gorbunov, V. B. Timofeev, F. Schäfler, J. P. Reithmaier, T. L. Reinecke, and S. N. Walck, *Phys. Rev. Lett.* 82, 1748 (**1999**).

120. A. Zrenner, M. Markmann, E. Beham, F. Findeis, G. Böhm, and G. Abstreiter, *J. Electronic Materials* 28, 542 (**1999**).

121. M. Bayer, O. Stern, A. Kuther, and A. Forchel, *Phys. Rev. B* 61, 7273 (**2000**).

122. H.-A. Engel and D. Loss, *Phys. Rev. Lett.* 86, 4648 (**2001**).

123. A. I. Yakimov, N. P. Stepina, A. V. Dvurechenskii, A. I. Nikiforov, and A. V. Nenashev, *Phys. Rev. B* 63, 045312 (**2001**).

124. A. I. Yakimov, N. P. Stepina, A. V. Dvurechenskii, A. I. Nikiforov, and A. V. Nenashev, *Semicond. Sci. Technol.* 15, 1125 (**2000**).

125. A. I. Yakimov, A. V. Dvurechenskii, A. A. Bloshkin, and A. V. Nenashev, *JETP Lett.* 83, 156 (**2006**).

126. A. I. Yakimov, A. V. Dvurechenskii, A. I. Nikiforov, A. A. Bloshkin, A. V. Nenashev, and V. A. Volodin, *Phys. Rev. B* 73, 115333 (**2006**).

127. A. I. Yakimov, V. A. Markov, A. V. Dvurechenskii, and O. P. Pchelyakov, *Philos. Mag. B* 65, 701 (**1992**).

128. A. I. Yakimov, V. A. Markov, A. V. Dvurechenskii, and O. P. Pchelyakov, *J. Phys.: Condens. Matter* 6, 2573 (**1994**).

REVIEW

REVIEW

129. R. C. Ashoori, H. L. Stormer, J. S. Weiner, L. N. Pfeiffer, K. W. Baldwin, and K. W. West, *Phys. Rev. Lett.* 71, 613 (**1993**).
130. A. I. Yakimov, A. V. Dvurechenskii, A. I. Nikiforov, and O. P. Pchelyakov, *Thin Solid Films* 336, 332 (**1998**).
131. A. I. Yakimov, A. V. Dvurechenskii, A. I. Nikiforov, and O. P. Pchelyakov, *JETP Lett.* 68, 135 (**1998**).
132. A. I. Yakimov, A. V. Dvurechenskii, A. I. Nikiforov, and S. V. Chaikovskii, *JETP Lett.* 75, 113 (**2002**).
133. T. H. Wang, H. W. Li, and J. M. Zhou, *Appl. Phys. Lett.* 79, 1537 (**2001**).
134. S. Averine, Y. C. Chan, and Y. L. Lam, *Appl. Phys. Lett.* 77, 274 (**2000**).
135. E. H. Nicollian and A. Goetzberger, *Bell Sys. Tech. J.* 46, 1055 (**1967**); D. L. Losee, *Appl. Phys. Lett.* 21, 54 (**1972**); G. Vincent, D. Bois, and P. Pinard, *J. Appl. Phys.* 46, 5173 (**1975**).
136. W.-H. Chang, W. Y. Chen, T. M. Hsu, N.-T. Yeh, and J.-I. Chyi, *Phys. Rev. B* 66, 195337 (**2002**).
137. C. M. A. Kapteyn, F. Heinrichsdorff, O. Stier, R. Heitz, M. Grundmann, N. D. Zakharov, D. Bimberg, and P. Werner, *Phys. Rev. B* 60, 14265 (**1999**); C. M. A. Kapteyn, M. Lion, R. Heitz, D. Bimberg, P. N. Brunkov, B. V. Volovik, S. G. Konnikov, A. R. Kovsh, and V. M. Ustinov, *Appl. Phys. Lett.* 76, 1573 (**2000**); S. Schulz, S. Schnüll, Ch. Heyn, and W. Hansen, *Phys. Rev. B* 69, 195317 (**2004**); S. K. Zhang, H. J. Zhu, F. Lu, Z. M. Jiang, and X. Wang, *Phys. Rev. Lett.* 80, 3340 (**1998**); C. Miesner, T. Asperger, K. Brunner, and G. Abstreiter, *Appl. Phys. Lett.* 77, 2704 (**2000**); H. Zhou, S. Huang, Y. Rao, Z. Jiang, and F. Lu, *Solid State Commun.* 25, 161 (**2003**); K. Schmalz, I. N. Yassievich, P. Schittenhelm, and G. Abstreiter, *Phys. Rev. B* 60, 1792 (**1999**); S. Anand, N. Carlsson, M.-E. Pistol, L. Samuelson, and W. Seifert, *J. Appl. Phys.* 84, 3747 (**1998**).
138. C. M. A. Kapteyn, M. Lion, R. Heitz, D. Bimberg, C. Miesner, T. Asperger, K. Brunner, and G. Absreiter, *Appl. Phys. Lett.* 77, 4169 (**2000**).
139. W.-H. Chang, W. Y. Chen, M. C. Cheng, C. Y. Lai, T. M. Hsu, N.-T. Yeh, and J.-I. Chyi, *Phys. Rev. B* 64, 125315 (**2001**).
140. D. V. Lang, *J. Appl. Phys.* 45, 3023 (**1974**).
141. P. N. Brounkov, A. Polimeni, S. T. Stoddart, M. Henini, L. Eaves, P. C. Main, A. R. Kovsh, Yu G. Musikhin, and S. G. Konnikov, *Appl. Phys. Lett.* 73, 1092 (**1998**).
142. M. Geller, C. Kapteyn, L. Müller-Kirsch, R. Heitz, and D. Bimberg, *Appl. Phys. Lett.* 82, 2706 (**2003**).
143. O. G. Schmidt, O. Kienzle, Y. Hao, K. Eberl, and F. Ernst, *Appl. Phys. Lett.* 74, 1272 (**1999**).
144. V. Le Thanh, V. Yam, P. Boucaud, F. Fortuna, C. Ulysse, D. Bouchier, L. Vervoort, and J.-M. Lourtioz, *Phys. Rev. B* 60, 5851 (**1999**); V. Le Thanh, V. Yam, P. Boucaud, Y. Zheng, and D. Bouchier, *Thin Solid Films* 369, 43 (**2000**).
145. D. V. Singh, R. Kim, T. O. Mitchell, J. L. Hoyt, and J. F. Gibbons, *J. Appl. Phys.* 85, 985 (**1999**).
146. Single-Charge Tunneling-Coulomb Blockade Phenomena in Nanostructures, Series B: Physics, edited by H. Grabert and M. H. Devoret, NATO Advanced Study Institute, Plenum Press, New York (**1991**).
147. F. Hofmann, T. Heinzel, D. A. Wharam, J. P. Kotthaus, G. Böhm, W. Klein, G. Tränke, and G. Weimann, *Phys. Rev. B* 51, 13 872 (**1995**); D. Dixon, L. P. Kouwenhoven, P. L. McEuen, Y. Nagamune, J. Motohisa, and H. Sakaki, *Phys. Rev. B* 53, 12 625 (**1996**); R. H. Blick, R. J. Haug, J. Weis, D. Pfannkuche, K. von Klitzing, and K. Eberl, *Phys. Rev. B* 7899 (**1996**); R. J. Haug, J. Weis, R. H. Blick, K. von Klitzing, K. Berl, and K. Ploog, *Semicond. Sci. Technol.* 11, 381 (**1996**); R. H. Blick, T. Schmidt, R. Haug, and K. von Klitzing, *Semicond. Sci. Technol.* 11, 1506 (**1996**); T. Schmidt, R. J. Haug, K. von Klitzing, A. Förster, and H. Lüth, *Phys. Rev. Lett.* 78, 1544 (**1997**).
148. C. I. Duruöz, R. M. Clarke, C. M. Marcus, and J. S. Harris, Jr., *Phys. Rev. Lett.* 74, 3237 (**1995**).

149. M. G. Ancona and R. W. Rendel, *J. Appl. Phys.* 77, 393 (**1995**).
150. A. I. Yakimov, A. V. Dvurechenskii, V. V. Kirienko, Yu I. Yakovlev, A. I. Nikiforov, and C. J. Adkins, *Phys. Rev. B* 61, 10868 (**2000**).
151. A. I. Yakimov, C. J. Adkins, R. Boucher, A. V. Dvurechenskii, A. I. Nikiforov, O. P. Pchelyakov, and G. Biskupski, *Phys. Rev. B* 59, 12598 (**1999**).
152. V. L. Nguyen, *Sov. Phys. Semicond.* 18, 207 (**1984**).
153. B. I. Shklovskii and A. L. Efros, Electronic Properties of Doped Semiconductors, Springer-Verlag, Heidelberg (**1984**).
154. I. L. Aleiner and B. I. Shklovskii, *Phys. Rev. B* 49, 13 721 (**1994**).
155. O. Entin-Wohlman and Z. Ovadyahu, *Phys. Rev. Lett.* 56, 643 (**1986**).
156. C. J. Adkins and E. G. Astrakharchik, *J. Phys.: Condens. Matter* 10, 6651 (**1998**).
157. F. W. Van Keuls, X. L. Hu, H. W. Jiang, and A. J. Dahm, *Phys. Rev. B* 56, 1161 (**1997**).
158. A. G. Zabrodskii and K. N. Zinov'eva, *Soviet JETP* 59, 425 (**1984**).
159. W. Mason, S. V. Kravchenko, G. E. Bowker, and J. E. Furneaux, *Phys. Rev. B* 52, 7857 (**1995**).
160. S. I. Knondaker, I. S. Shlimak, J. T. Nicholls, M. Pepper, and D. A. Ritchie, *Phys. Rev. B* 59, 4580 (**1999**).
161. V. I. Kozub, S. D. Baranovskii, and I. S. Shlimak, *Solid State Commun.* 113, 587 (**2000**).
162. A. F. Zinovieva, A. V. Nenashev, and A. V. Dvurechenskii, *Phys. Rev. B* 71, 033310 (**2005**).
163. A. I. Yakimov, A. V. Dvurechenskii, G. M. Minkov, A. A. Sherstobitov, A. I. Nikiforov, A. A. Bloshkin, N. P. Stepina, J. P. Leitão, N. A. Sobolev, L. Pereira, and M. C. do Carmo, *Phys. Stat. Sol. (c)* 3, 296 (**2006**).
164. V. Ya Aleshkin, N. A. Bekin, N. G. Kalugin, Z. F. Krasil'nik, A. V. Novikov V. V. Postnikov, and H. Seyringer, *JETP Lett.* 67, 48 (**1998**).
165. A. V. Dvurechenskii and A. I. Yakimov, *Semiconductors* 35, 1143 (**2001**).
166. A. I. Yakimov, A. V. Dvurechenskii, N. P. Stepina, A. V. Nenashev, and A. I. Nikiforov, *Nanotechnology* 12, 441 (**2001**).
167. A. I. Yakimov, A. V. Dvurechenskii, N. P. Stepina, A. I. Nikiforov, and A. V. Nenashev, *JETP* 92, 500 (**2001**).
168. K. H. Schmidt, G. Medeiros-Ribeiro, and P. M. Petroff, *Phys. Rev. B* 58, 3597 (**1998**).
169. T. M. Hsu, W.-H. Chang, K. F. Tsai, J.-I. Chyi, N. T. Yeh, and T. E. Nee, *Phys. Rev. B* 60, R2189 (**1999**).
170. R. J. Warburton, C. S. Dürr, K. Karrai, J. P. Kotthaus, G. Medeiros-Ribeiro, and P. M. Petroff, *Phys. Rev. Lett.* 79, 5282 (**1997**).
171. F. Hatami, M. Grundmann, N. N. Ledentsov, F. Heinrichsdorff, R. Heitz, J. Böhrer, D. Bimberg, S. S. Ruvimov, P. Werner, V. M. Ustinov, P. S. Kop'ev, and Zh. I. Alferov, *Phys. Rev. B* 57, 4635 (**1998**).
172. J. M. Rorison, *Phys. Rev. B* 48, 4643 (**1993**).
173. A. Wojs and P. Hawrulak, *Phys. Rev. B* 55, 13066 (**1997**).
174. M. Grundmann, O. Stier, and D. Bimberg, *Phys. Rev. B* 52, 11969 (**1995**).
175. S.-S. Li and J.-B. Xia, *J. Appl. Phys.* 88, 7171 (**2000**).
176. J. A. Barker and E. P. O'Reilly, *Phys. Rev. B* 61, 13840 (**2000**).
177. W. Sheng and J.-P. Leburton, *Phys. Rev. Lett.* 88, 167401 (**2002**).
178. K. L. Janssens, B. Partoens, and F. M. Peeters, *Phys. Rev. B* 65, 233301 (**2002**).
179. P. W. Fry, I. E. Itskevich, D. J. Mowbray, M. S. Skolnick, J. J. Finley, J. A. Barker, E. P. O'Reilly, L. R. Wilson, I. A. Larkin, P. A. Maksum, M. Hopkinson, M. Al-Khafaji, J. P. R. David, A. G. Cullis, G. Hill, and J. C. Clark, *Phys. Rev. Lett.* 84, 733 (**2000**); P. W. Fry, I. E. Itskevich, S. R. Parnell, J. J. Finley, L. R. Wilson, K. L. Schumacher, D. J. Mowbray, M. S. Skolnick, M. Al-Khafaji, A. G. Cullis, M. Hopkinson, J. C. Clark, and G. Hill, *Phys. Rev. B* 62, 16784 (**2000**).
180. A. Patanè, A. Levin, A. Polimeni, F. Schindler, P. C. Main, L. Eaves, and M. Henini, *Appl. Phys. Lett.* 77, 2979 (**2000**).

181. F. Findeis, M. Baier, E. Beham, A. Zrenner, and G. Abstreiter, *Appl. Phys. Lett.* 78, 2958 (**2001**).

182. Zhonghui Chen, Eui-Tae Kim, and Anupam Madhukar, *Appl. Phys. Lett.* 80, 2770 (**2002**).

183. A. I. Yakimov, A. V. Dvurechenskii, A. I. Nikiforov, V. V. Ulyanov, A. G. Milekhin, A. O. Govorov, S. Shulze, and D. R. T. Zahn, *Phys. Rev. B* 67, 125318 (**2003**).

184. A. V. Dvurechenskii and A. I. Yakimov, Towards the First Silicon Laser, edited by L. Paversi, Kluwer Academic Publishers, Netherland (**2003**), p. 307.

185. A. I. Yakimov, A. V. Dvurechenskii, A. I. Nikiforov, O. P. Pchelyakov, and A. V. Nenashev, *Phys. Rev. B* 62, R16283 (**2000**).

186. A. I. Yakimov, A. V. Dvurechenskii, and A. I. Nikiforov, *JETP Lett.* 73, 529 (**2001**).

187. R. Sasagawa, H. Sugawara, Y. Ohno, H. Nakajima, S. Tsujino, H. Akiyama, and H. Sakaki, *Appl. Phys. Lett.* 72, 719 (**1998**).

188. M. Załużny, *Phys. Rev. B* 43, 4511 (**1991**); M. Załużny, *Phys. Rev. B* 49, 2923 (**1994**).

189. T. Ando, A. B. Fowler, and F. Stern, *Rev. Mod. Phys.* 54, 437 (**1982**).

190. C. Metzner and G. H. Döhler, *Phys. Rev. B* 60, 11005 (**1999**).

191. A. O. Govorov and A. V. Chaplik, *Sov. Phys. JETP* 72, 1037 (**1991**).

192. M. Załużny, *J. Appl. Phys.* 74, 4716 (**1993**).

193. P. Schittenhelm, C. Engel, F. Findeis, G. Abstreiter, A. A. Darhuber, G. Bauer, A. O. Kosogov, and P. Werner, *J. Vac. Sci. Technol. B* 16, 1575 (**1998**).

194. C. Miesner, O. Röthig, K. Bruner, and G. Abstreiter, *Physica E* 7, 145 (**2000**).

195. N. Rappaport, E. Finkman, T. Brunhes, P. Boucaud, S. Sauvage, N. Yam, V. Le Thanh, and D. Bouchier, *Appl. Phys. Lett.* 77, 3224 (**2000**).

196. A. I. Yakimov, A. V. Dvurechenskii, A. I. Nikiforov, and Yu Yu Proskuryakov, *J. Appl. Phys.* 89, 5676 (**2001**).

197. R. Apetz, L. Vescan, A. Hartmann, C. Dieker, and H. Lüth, *Appl. Phys. Lett.* 66, 445 (**1995**).

198. L. Vescan and T. Stoica, *J. Luminescence* 80, 485 (**1999**).

199. O. G. Schmidt, U. Denker, K. Eberl, O. Kienzle, F. Ernst, and R. J. Haug, *Appl. Phys. Lett.* 77, 4341 (**2000**).

200. A. I. Yakimov, A. V. Dvurechenskii, V. V. Kirienko, and A. I. Nikiforov, *Appl. Phys. Lett.* 80, 4783 (**2002**).

201. N. Horiguchi, T. Futatsugi, Y. Nakata, and N. Yokoyama, *Appl. Phys. Lett.* 70, 2294 (**1997**).

202. J. Phillips, K. Kamath, T. Brock, and P. Bhattacharya, *Appl. Phys. Lett.* 72, 3509 (**1998**).

203. K. H. Schmidt, M. Versen, U. Kunze, D. Reuter, and A. D. Wieck, *Phys. Rev. B* 62, 15879 (**2000**).

204. H. Ishikuro, T. Fujii, T. Saraya, G. Hashiguchi, T. Hiramoto, and T. Ikoma, *Appl. Phys. Lett.* 68, 3585 (**1996**).

205. L. Guo, E. Leobandung, and S. Y. Chou, *Appl. Phys. Lett.* 70, 850 (**1997**).

206. T. Sakamoto, H. Kawaura, and T. Baba, *Appl. Phys. Lett.* 72, 795 (**1998**).

207. N. Takahashi, H. Ishikuro, and T. Hiramoto, *Appl. Phys. Lett.* 76, 209 (**2009**).

208. L. Zhuang, L. Guo, and S. Y. Chou, *Appl. Phys. Lett.* 72, 1205 (**1998**).

209. T. H. Wang, H. W. Li, and J. M. Zhou, *Appl. Phys. Lett.* 78, 2160 (**2001**).

210. J. W. Park, K. S. Park, B. T. Lee, C. H. Lee, Jung B. Choi, K.-H. Yoo, J. Kim, S. C. Oh, S. I. Park, K. T. Kim, and J. J. Kim, *Appl. Phys. Lett.* 75, 566 (**1999**).

211. A. I. Yakimov, A. V. Dvurechenskii, A. I. Nikiforov, and O. P. Pchelyakov, *Phys. Low-Dim. Struct.* 3/4, 99 (**1999**).

212. C. W. J. Beenakker, *Phys. Rev. B* 44, 1646 (**1991**).

213. K. A. Matveev and L. I. Glazman, *Phys. Rev. B* 54, 10339 (**1996**).

214. N. F. Mott and E. A. Davis, Electronic Processes in Non-Crystalline Materials, 2nd edn., Clarendon Press, Oxford (**1979**).

215. A. Vasanelli, M. De Giorgi, R. Ferreira, R. Cingolani, and G. Bastard, *Physica E* 11, 41 (**2001**).

216. V. Ryzhii, *Semicond. Sci. Technol.* 11, 759 (**1996**).

217. V. Ryzhii, V. Pipa, I. Khmyrova, V. Mitin, and M. Willander, *Jpn. J. Appl. Phys.* 39, L1283 (**2000**).

218. V. Ryzhii, *Appl. Phys. Lett.* 78, 3346 (**2001**).

219. V. Ryzhii, I. Khmyrova, V. Mitin, M. Stroscio, and M. Willander, *Appl. Phys. Lett.* 78, 3523 (**2001**).

220. V. Ryzhii, I. Khmyrova, V. Pipa, V. Mitin, and M. Willander, *Semicond. Sci. Technol.* 16, 331 (**2001**).

221. R. A. Suris, Future Trends in Microelectronics, edited by S. Luryi, Kluwer Academic Publishers, Netherlands (**1996**), p. 197.

222. M. Elkurdi, P. Boucaud, S. Sauvage, O. Kermarrec, Y. Campidelli, D. Bensahel, G. Saint-Girons, and I. Sagnes, *Appl. Phys. Lett.* 80, 509 (**2002**).

223. A. I. Yakimov, A. V. Dvurechenskii, A. I. Nikiforov, S. V. Chaikovskii, and S. A. Tiis, *Semiconductors* 37, 1383 (**2003**).

224. A. I. Yakimov, A. V. Dvurechenskii, V. V. Kirienko, N. P. Stepina, A. I. Nikiforov, V. V. Ulyanov, S. V. Chaikovskii, V. A. Volodin, M. D. Efremov, M. S. Seksenbaev, and K. S. Zhuravlev, *Semiconductors* 38, 1225 (**2004**).

225. L. P. Rokhinson, D. C. Tsui, J. L. Benton, and Y.-H. Xie, *Appl. Phys. Lett.* 75, 2413 (**1999**).

226. C. Miesner, K. Brunner, and G. Abstreiter, *Phys. Stat. Sol.* (*a*) 224, 605 (**2001**).

227. C. Miesner, K. Brunner, and G. Abstreiter, *Infrared Physics and Technology* 42, 461 (**2001**).

228. P. Boucaud, T. Brunhes, S. Sauvage, N. Yam, V. Le Thanh, D. Bouchier, N. Rappaport, and E. Finkman, *Phys. Stat. Sol.* (*a*) 224, 233 (**2001**).

REVIEW